

ALMA Mater Studiorum
Universita` degli di Studi Bologna

SCUOLA DI SCIENZE

Corso di Laurea Magistrale in Astrofisica e Cosmologia

Dipartimento di Fisica e Astronomia

The Environment Of Radio Sources In The
VLA-COSMOS Survey

Elaborato Finale

Candidato:

Nicola Malavasi

Relatore:

Chiar.mo Prof.:

Andrea Cimatti

Co-relatore:

Sandro Bardelli

Sessione II - Prima Seduta
Anno Accademico 2012/2013

Abstract

Sebbene studiati a fondo, i processi che hanno portato alla formazione e alla evoluzione delle galassie così come sono osservate nell'Universo attuale non sono ancora del tutto compresi. La visione attuale della storia di formazione delle strutture prevede che il collasso gravitazionale, a partire dalle fluttuazioni di densità primordiali, porti all'innesco della formazione stellare; quindi che un qualche processo intervenga e la interrompa. Diversi studi vedono il principale responsabile di questa brusca interruzione della formazione stellare nei fenomeni di attività nucleare al centro delle galassie (Active Galactic Nuclei, AGN), capaci di fornire l'energia necessaria a impedire il collasso gravitazionale del gas e la formazione di nuove stelle. Uno dei segni della presenza di un tale fenomeno all'interno di una galassia è l'emissione radio dovuta ai fenomeni di accrescimento di gas su buco nero.

In questo lavoro di tesi si è studiato l'ambiente delle radio sorgenti nel campo della survey VLA-COSMOS. Partendo da un campione di 1806 radio sorgenti e 1482993 galassie che non presentassero emissione radio, con redshift fotometrici e fotometria provenienti dalla survey COSMOS e dalla sua parte radio (VLA-COSMOS), si è stimata la ricchezza dell'ambiente attorno a ciascuna radio sorgente, contando il numero di galassie senza emissione radio presenti all'interno di un cilindro di raggio di base 1 Mpc e di altezza proporzionale all'errore sul redshift fotometrico di ciascuna radio sorgente, centrato su di essa. Al fine di stimare la significatività dei risultati si è creato un campione di controllo costituito da 1806 galassie che non presentassero emissione radio e si è stimato l'ambiente attorno a ciascuna di esse con lo stesso metodo usato per le radio sorgenti.

I risultati mostrano che gli ammassi di galassie aventi al proprio centro una radio sorgente sono significativamente più ricchi di quelli con al proprio centro una galassia senza emissione radio. Tale differenza in ricchezza permane indipendentemente da selezioni basate sul redshift, la massa stellare e il tasso di formazione stellare specifica delle galassie del campione e mostra che gli ammassi di galassie con al proprio centro una radio sorgente dovuta a fenomeni di AGN sono significativamente più ricchi di ammassi con al proprio centro una galassia senza emissione radio. Questo effetto è più marcato per AGN di tipo FR I rispetto ad oggetti di tipo FR II, indicando una correlazione fra potenza dell'AGN e formazione delle strutture.

Tali risultati gettano nuova luce sui meccanismi di formazione ed evoluzione delle galassie che prevedono una stretta correlazione tra fenomeni di AGN, formazione stellare ed interruzione della stessa.

Contents

1	Introduction	1
1.1	The General View	1
1.2	The Formation Of First Structures	3
1.3	The Role Of Merging And The AGN Phase	4
1.4	Star Formation Quenching And The Passive Evolution	7
1.5	The Different Types Of Radio AGNs	10
1.6	The Thesis	11
2	Data Description	13
2.1	The COSMOS Survey	13
2.1.1	The Optical Sample Of The COSMOS Survey	15
2.1.2	COSMOS Photometric Redshifts	16
2.1.3	The VLA-COSMOS Survey	19
2.2	The Data Sample For This Work	22
2.2.1	How Absolute Magnitude, Stellar Mass And Specific Star Formation Rate Are Derived	23
2.3	Conclusions	24
3	Preliminary Data Analysis	27
3.1	Matching	27
3.2	Radio Flux, Redshift And Apparent Magnitude Distributions	28
3.2.1	Radio Flux Distribution	28
3.2.2	Apparent I-Band Magnitude Distributions	29
3.2.3	Redshift Distributions	29
3.3	Absolute Magnitude, Radio Luminosity, Stellar Mass And Spe- cific Star Formation Rate	31
3.3.1	Absolute Magnitude Distribution	32
3.3.2	Radio Luminosity Distribution	33
3.3.3	Specific Star Formation Rate And Stellar Mass	34
3.4	Conclusions	38
4	The Study Of The Environment	39
4.1	The Searching Algorithm	39
4.2	The Control Sample	40
4.3	Fixed Distance	40

4.3.1	Fixed Distance, Apparent Magnitude Cut	44
4.3.2	Stellar Mass And Specific Star Formation Rate Selections	46
4.3.3	Stellar Mass And Specific Star Formation Rate Selections Applied Also To The Optical Sample	48
4.4	Redshift Dependent Radius	53
4.4.1	Apparent Magnitude Cut	54
4.4.2	Specific Star Formation Rate And Stellar Mass Cut . . .	57
4.4.3	Stellar Mass And Specific Star Formation Rate Selections Applied Also To The Optical Sample	60
4.5	The Check For Significativity	63
4.6	Conclusions	76
5	The Study Of The Environment - A Restriction To $1 \leq z \leq 2$	77
5.1	Analysis Of The Redshift Range $1 \leq z \leq 2$	77
5.2	The Absolute Radio Luminosity Cut	84
5.3	Conclusions	94
6	Conclusions	95
6.1	The Properties Of The Environment Around Radiogalaxies . . .	95
6.1.1	Fixed Distance	95
6.1.2	Redshift Dependence	97
6.2	The Restriction To $1 \leq z \leq 2$	98
6.3	The Distinction Between Low Power And High Power Radio Sources	99
6.4	Comparison With Previous Works	100
6.5	Summary	101
A	χ^2 Distribution Table	103

Chapter 1

Introduction

1.1 The General View

ONE of the most interesting fields of research in modern astrophysics is undoubtedly the study of the process which lead to the formation of galaxies as are observed in the present-day Universe. Although thoroughly studied and analyzed, the problem of galaxy formation and evolution it is still not yet understood in its complexity.

The process which forms galaxies, as it is in its current understanding, is not a simple one. It involves many steps, each of which lacks full comprehension, although a general view can be outlined. General agreement, supported by empirical observations, has been reached and a story of galaxy formation, from the first overdensities created in the early epochs of the Universe, to the modern structures observed nowadays has been delineated.

The general view is that galaxies are formed through mergers of structures that originate from the collapse of the first overdensities of the cosmological density field. This idea of the process has been initially proposed by White & Rees (1978). The first structures to collapse are dark matter haloes, since they first decouple from the radiation and can collapse freely. This creates the first potential wells into which the gas falls once it decouples from the radiation, at later times. The collapsing gas forms the first generation of stars (population III stars) and forms the first structures, gas rich disks. The red, gas poor spheroids and elliptical galaxies are built in roughly two ways. The bigger, more luminous elliptical galaxies, such as central dominant galaxies of galaxy clusters are formed through the accretion of gas coming from the cooling flows that form during the formation of the cluster itself. This inflow of gas also triggers the Active Galactic Nucleus (AGN) phase of the galaxy, and accounts for its energy output. This vision is supported, for example, by the observation that every cluster with a strong cooling flow also contains a massive and active central radio galaxy (Burns et al., 1981). Merging is not a very efficient formation mechanism for these galaxies since the velocity dispersion at the center of clusters are too high for galaxies having encounters leading to successful mergers. Instead, galaxy merging becomes successful on smaller scales, since the central velocity dispersion of smaller galaxy clusters and groups allow for the galaxies

to merge and trigger a luminous quasar phase. The idea took place, therefore, that radiogalaxies might regulate cooling flows (Tabor & Binney, 1993). Small spheroids, instead are formed through secular accretion of hot gas and mergers, again, do not play a dominant role.

Examples of the refinement of the idea introduced by White & Rees (1978) can be found in Hopkins et al. (2008a), with a generalization in Hickox et al. (2009). A summary of the process is found also in the introduction of Croton et al. (2006) (and references therein) and in Longair (2008).

A scheme that can be kept in mind and that gives a good summary of the formation process for the galaxies on the small cluster scale is showed in figure 1.1, taken from Hopkins et al. (2008a), a work that present an analysis of the role that merging plays in the formation and evolution of galaxies.

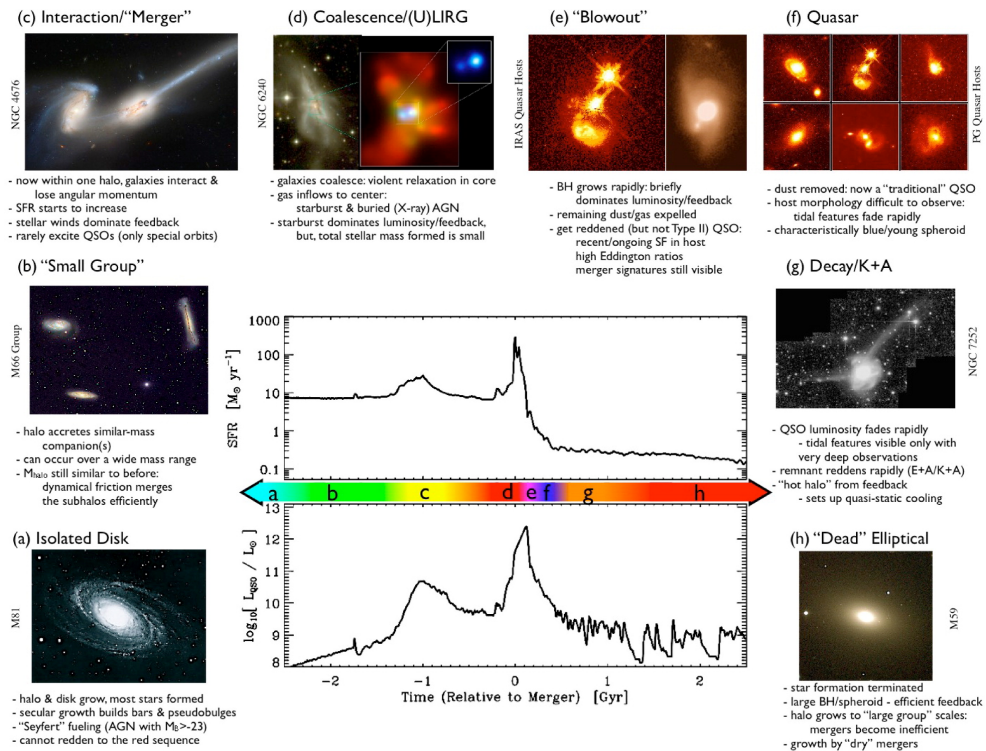


Figure 1.1: The galaxy formation mechanism which operates on small cluster scales. (Figure from Hopkins et al. (2008a)).

This chapter is structured as follows: in section 1.2 a brief description of the collapse of dark matter haloes, gas inflow and Population III stars is given. In section 1.3 the role of merging in triggering the AGN phase is described. Star formation quenching, passive evolution and the present day Universe are described in section 1.4, while in section 1.5 a brief description of the radiogalaxy types is outlined. Finally the outline of this thesis work and its role in the understanding the process of galaxy formation and evolution is given section 1.6.

1.2 The Formation Of First Structures

The structures that are observed in present day Universe originate from small fluctuations in the density field that is originated in the Big Bang. These perturbations have the form of

$$\delta = \frac{\Delta \varrho}{\langle \varrho \rangle} = \frac{\varrho - \langle \varrho \rangle}{\langle \varrho \rangle} \propto \frac{1}{1+z} \quad (1.1)$$

following the description found in Longair (2008). The medium whose density is considered is a mixture of dark matter, radiation and baryonic matter all coupled together. The evolution of the density perturbations is the same for the three components of the medium as long as they are coupled. Since the evolution of the density fluctuation is proportional to the inverse of redshift, at the redshift of $z \sim 1000$, corresponding to the surface of last scattering (where the Cosmic Microwave Background is created), the value of the density fluctuations is expected to be of the order of 10^{-3} . This is in good agreement with what found from the study of CMB anisotropies (see for example Spergel et al. (2003)), since the primordial density fluctuations leave an imprint in the form of temperature anisotropies on the temperature field of the Cosmic Microwave Background. These temperature fluctuations are observed to be of the order of 10^{-5} at $z = 1100$ therefore compatible with the assumptions made.

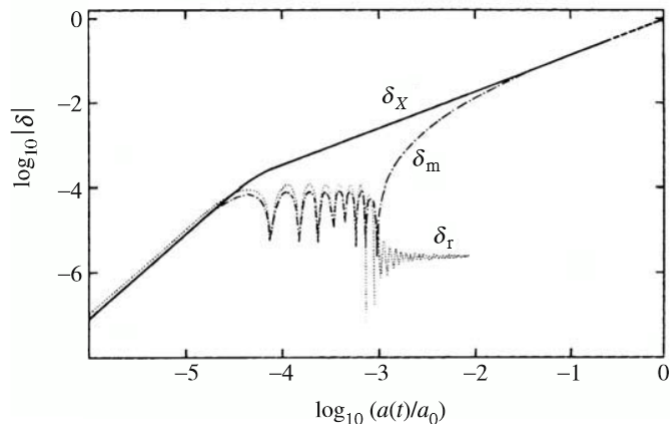


Figure 1.2: A schematic representation of the evolution of the primordial fluctuations. The evolution for three species is represented: a cold dark matter component (δ_X), a baryonic component (δ_m) and a radiation component (δ_r). Figure taken from Coles & Lucchin (2002)

Figure 1.2, taken from Coles & Lucchin (2002), represents a good summary of what happens at various stages of the collapse of the primordial density fluctuations. This figure shows the evolution of the density fluctuations of a medium composed of three species: a cold dark matter component (δ_X), a baryonic component (δ_m) and a radiation component (δ_r).

Following the descriptions found in Coles & Lucchin (2002) and in Longair (2008), the process which leads to the collapse of the primordial density fluctuations can be summed up as it follows. At first, the medium composed of cold

dark matter¹, baryonic matter and radiation is not decoupled. The density fluctuations evolve as $\frac{1}{1+z}$. The first component to decouple is dark matter, since it has no interaction with radiation. After the decoupling of cold dark matter, the first dark matter haloes begin to collapse. The potential wells become deeper, although the haloes cannot reach a full collapse. This is because dark matter is not at all efficient in dissipating the energy gained from gravitational collapse, since it lacks interaction with radiation and therefore the possibility to radiate the gravitational energy acquired during collapse. Instead, baryonic matter is much more efficient in dissipating, through the emission of radiation, the energy that is gained during gravitational collapse. Therefore, after a lapse of time during which the baryon-radiation plasma density fluctuations oscillate, while keeping almost constant amplitude, the baryonic matter decouples from radiation. The gas, composed mainly of hydrogen and helium, falls into the gravitational potential wells created by dark matter haloes and, thanks to its ability to dissipate through radiation the gravitational energy acquired, it can fully collapse. Radiation fluctuations, instead never grow and so do not enter the processes that regulate the formation and evolution of structures.

Once the gas falls into the gravitational potential wells, already in place due to the formation of cold dark matter halos, it turns into stars. These stars (called Population III stars) are the first stars that ever ignited and are composed only of hydrogen and helium in the primordial abundance, set by Big Bang nucleosynthesis. Their observation has been the subject of several studies, but results are controversial.

Together with the formation of the first stars, also the first structures are built. The first galaxies are assembled, small spheroids and disks, at the center of which the first black holes are beginning to form, as expected from the discovery of scaling laws which relate the properties of the central black hole to those of the host galaxy (*e.g.* see Magorrian et al. (1998), Kormendy & Richstone (1995), Ferrarese & Merritt (2000), Gebhardt et al. (2000)).

1.3 The Role Of Merging And The AGN Phase

In the previous section, the primordial formation of structures has been analyzed. The path which connects the spectrum of the primeval density fluctuations with the first galaxies and population III stars has been quite understood and general agreement has been achieved over the majority of the process. By redshift $z = 6$ the Universe is populated by a great number of galaxies, the majority of which is replenished of cold gas, situated in a disk. More massive galaxies are mainly at the center of protoclusters, embedded in the most mas-

¹Alternatively also hot dark matter can be considered. The difference between the two stands in whether the particles of which dark matter is composed were relativistic at the moment of the decoupling from radiation. If the particles were relativistic at the moment of decoupling then dark matter is called “Hot”, while if the particles became non relativistic before decoupling, the dark matter is said to be “Cold”. Hot and cold dark matter differ also in the way they give start to the formation of structures: hot dark matter produces the so-called “top-down scenario” in which smaller structures such as globular clusters and galaxies form by fragmentation of a bigger, large scale structure; instead cold dark matter gives rise to the opposite “bottom-up scenario” in which large scale structure and big galaxies form by aggregation of smaller parts, such as globular clusters and smaller disk galaxies. Since this second scenario seems to better match astrophysical observations and observed phenomena, only cold dark matter will be considered in the rest of this work.

sive dark matter haloes and accrete gas which has undergone massive cooling from the surrounding. Mid-sized galaxies are positioned in the group scale, in lower mass dark matter haloes, while lowest mass galaxies populate all kind of environments.

Although, as said before, what stated in the previous section is almost fully understood, how the primordial structures turn into the galaxies observed in the present-day Universe is still debated. The current view is that galaxies evolve in different ways, depending on the mass of the dark matter halo they are in. Every mechanism proposed has to cope with several observed facts. As an example, nowadays, red elliptical galaxies are common. They show no formation of new stars, lack the presence of cold gas and are not rotationally supported (as showed in Kormendy (1982)). Therefore, every galaxy formation mechanism must reproduce the observed population of elliptical galaxies, and account for their formation. Nevertheless, disk galaxies, rich in cold gas, rotationally supported and with evident signature of ongoing star formation are present too and must be accounted for as well in any mechanism of galaxy formation and evolution.

The first mechanism, which leads to the formation of present day galaxies from the first structures that have been created, is merging. It is believed that merging is capable of producing elliptical galaxies, starting from disk-like gas rich galaxies, provided that the mass, dark halo mass, mass ratio of the merging galaxies and gas content are suitable. In this scenario, the evolution of a galaxy is regulated by the process showed in figure 1.1. In particular, two galaxies have a so-called “major wet merger”, *i.e.* a merger in which both of the colliding galaxies have comparable mass and a great reservoir of cold gas. The torque generated on the disks by the tidal interactions triggers star formation in the gas and deviates a large fraction of the cold gas towards the central black hole. This triggers a phase of Active Galactic Nucleus (AGN) of the galaxy resulted from the merger. The AGN will then quench the star formation.

The problems with the merging scenario are that, in order to result efficient in creating elliptical galaxies, merging should have peculiar qualities. As analyzed, for example, in Hopkins et al. (2008a), mergers should happen between galaxies with a mass ratio not larger than 3:1 and both galaxies must contain large quantities of cold gas. This kind of mergers do not happens with the same probability in all of the environments in which galaxies can be found. In fact, if the mass of the dark matter halo is too large, as it happens in the case of massive galaxy clusters, at its center galaxies will have velocities too large in order to have succesful merging events. Therefore, it seems unlikely that merging could be the principal way of forming clusters central dominant elliptical galaxies. Moreover, isolated galaxies (or galaxies in less dense environments), still retain disk-like morphologies, or are small spheroids which seem to never have gone through a major merger events. Another formation mechanism seems then to be required, in order to explain these observations. Instead, merging seems to be the principal galaxy formation mechanism on the scale of small galaxy clusters and galaxy groups. On this scale merging is very efficient and theory of galaxy formation through merger events on the medium size scale are in good agreement with the observations. Figure 1.3, taken from Hickox et al. (2009), reproduces the formation mechanism with the segregation in dark halo mass, therefore accounting for the different evolutionary paths of galaxies.

Another formation mechanism has been proposed to operate on small scales,

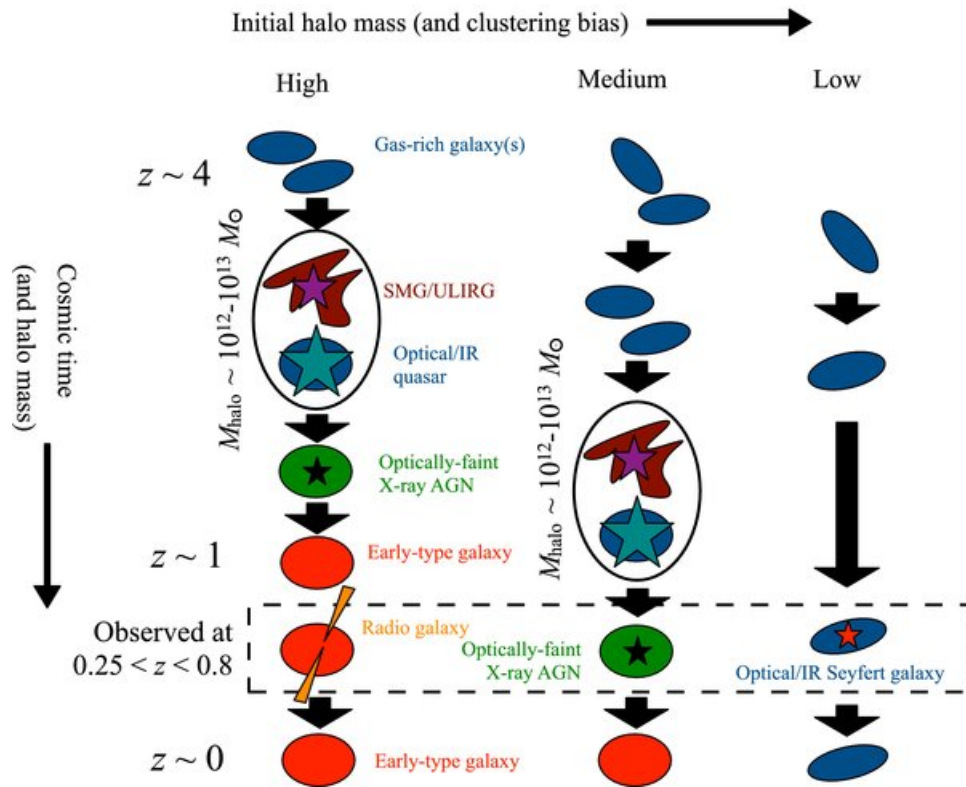


Figure 1.3: The galaxy formation mechanism, differentiated by host dark matter halo mass. Figure from Hickox et al. (2009).

1.4. STAR FORMATION QUENCHING AND THE PASSIVE EVOLUTION 7

where merging is not efficient due to the lack of galaxies with adequate properties. It is known, from the theory of AGNs (see also section 1.5) that two modes of accretion on to black hole are responsible for AGN with different properties. The difference in the modes of accretion results in difference in the AGN emission, as analyzed, for example, in Hardcastle et al. (2007). The difference between the two modes consists in the source of the gas that accretes on the supermassive black hole and that fuels the AGN emission. In particular it has been discovered that cold gas accretion is responsible for high-power radio-loud AGNs, like Fanaroff-Riley class II objects (Fanaroff & Riley, 1974), while hot gas is responsible for the low-power radio-loud AGNs, like Fanaroff-Riley class I objects. Therefore, on the scales where merging is not efficient in bringing cold gas to the central black hole and therefore cannot be accounted as a mechanism for the mass growth of the galaxy, the hot gas accretion mode can replace it as an accretion mechanism. In this view, galaxies embedded in small scale dark haloes can grow through secular accretion of hot gas and evolve to become small mass red spheroids or spiral galaxies.

It is still controversial if hot gas accretion is responsible also for the growth and the formation of high mass elliptical galaxies, like those found at the center of massive galaxy clusters, where the velocities of galaxies are too high to allow for succesful merger events. If the black holes of these high mass galaxies accrete hot gas, like the one that is responsible for the X-Ray emission of the galaxy clusters, this could lead to an evolution mechanism capable of reproducing the observations. Another explanation could be that these galaxies accrete the gas cooling from the central part of the galaxy clusters and therefore form at the end of the cooling flows.

1.4 Star Formation Quenching And The Passive Evolution

Another important part of galaxy evolution which is yet to be fully understood is the mechanism which leads to the formation of the nowadays observed, so-called *red & dead* elliptical galaxies.

When galaxies do form, an intense burst of star formation, together with a phase of AGN activity is triggered. Nevertheless, this same phase of intense activity must be somehow terminated, in order to reproduce the observed characteristics of elliptical galaxies.

The need for a quenching mechanism is evidantiated also when considering the Cosmic Star Formation History (CSFH). The star formation history for the entire Universe has been estimated by Soifer et al. (2008), using the infrared luminosity of galaxies. A plot of the CSFH as a function of redshift is showed in figure 1.4.

From this figure it can be seen that the star formation of the universe reaches its maximum for redshifts in the interval $z \in [1; 2]$ and that in this interval is quite constant. For redshifts higher than 2, although the quality of data is lower, a decline in star formation seems plausible, since the Universe was too young for the first structures to form. More certain is, nevertheless, the abrupt stop in star formation for redshifts from $z = 1$ to present days. In order to explain this sudden termination in the formation of stars, some sort of quenching mechanism

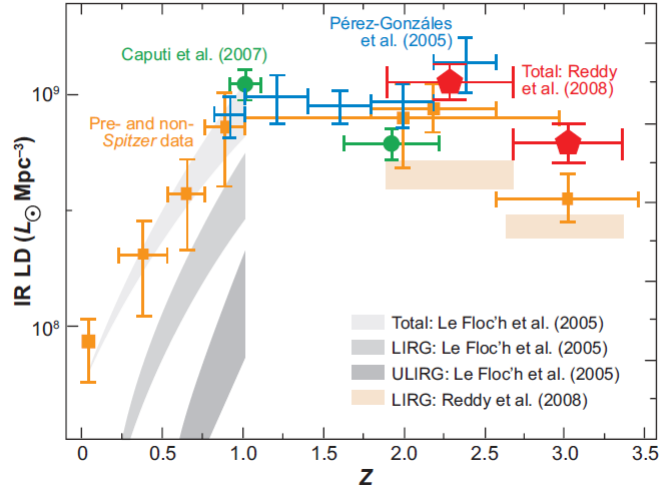


Figure 1.4: The Cosmic Star Formation History. On the vertical axis is the Infrared Luminosity Density is plotted, used as a proxy for star formation. (Figure From Soifer et al. (2008)).

is required to intervene.

An analysis of the mechanisms which lead to the sudden termination of the star formation has been carried out, for example, by Hopkins et al. (2008b).

The most accounted path, which leads from a gas-rich, post-merger situation to a gas-poor elliptical galaxy, with no star formation and an anisotropic orbital distribution is the so called *quenching* process. The idea is that the merger of two gas rich galaxies, such as those described in section 1.3, triggers a violent phase of star formation, making the galaxy colors bluer. Also, a massive inflow of gas, which accretes on the central black hole, triggers a phase of Active Galactic Nucleus, making the galaxy appear as a Quasar source. These two events are also responsible for the quenching of the star formation. A few possible viable mechanisms are reported below:

Kinematic Feedback: Mergers move large quantities of gas, mixing hot and cold gas from the outer and inner regions of the halo. Moreover, cooling flows can be interrupted and shocks may heat gas, therefore interrupting star formation.

Winds: The intense starburst developed during a merger can generate a galactic wind which both heats the gas and blows it away from the galaxy and into the hot Intergalactic Medium (IGM), therefore quenching star formation. Also, the most massive stars turn into supernovae very quickly and almost all together. This large quantity of supernova explosions can also generate a strong wind and contribute to the effect.

AGN: Quasars and Active Galactic Nuclei are among the most powerful events in the Universe. The strong radiation emitted from the accretion phenomena around the black hole is capable of heating the gas, while mechanical

1.4. STAR FORMATION QUENCHING AND THE PASSIVE EVOLUTION

feedback such as jets, outflows and winds can blow the gas away from the galaxy. It is the most powerful source of quenching.

Whether one of the above mentioned mechanisms dominates or whether all of them are responsible of quenching is still to be understood. In particular, studies have showed (Croton et al., 2006) that AGN activity is more efficient in quenching star formation, since the entropy of the output from such a phenomenon does not depend on the starburst activity prior to it. Using semianalytical models implemented onto the output of the Millennium Run (Springel et al., 2005) in order to simulate the process of galaxy formation, Croton et al. (2006) showed that the onset of an AGN phase to suppress the cooling flow in massive galaxies allows to better reproduce the high luminosity cut-off in the galaxy luminosity functions in the K and b_J bands, as showed in figure 1.5.

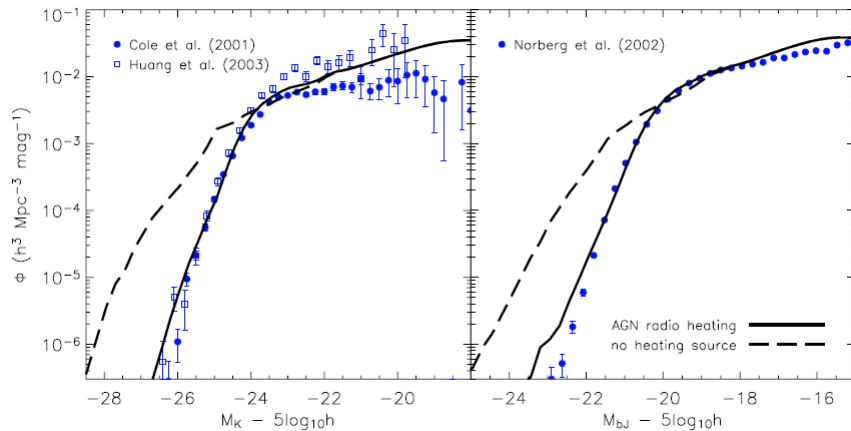


Figure 1.5: Galaxy luminosity functions, in the K and b_J bands. The solid line represents the model with AGN feedback, the dashed line represents the model without AGN feedback. The agreement with the data is much better for the AGN feedback case. Data points are taken from the literature. (Figure from Croton et al. (2006)).

This figure shows the perfect agreement with observational data of the model with AGN feedback compared to the model without AGN feedback as described in Croton et al. (2006). This is a confirm of the importance of the role of AGN in suppressing cooling flows and quenching star formation.

Nevertheless two different modes for AGN quenching seem possible: a “quasar mode”, which requires accretion of cold gas and is far more powerful, and a “radio mode”, in which the central black hole accretes hot gas for a longer time. According to Croton et al. (2006) this second accretion mode could be more efficient in quenching star formation, since the low luminosity, sub-Eddington accretion disk deriving from the accretion of hot gas could still supply the energy needed to heat the gas, while maintaining also the gas hot for a longer time. It appears that the two different accretion modes operates in galaxies of different mass. In fact, it seems plausible that in higher mass systems the hot phase gas (with temperatures of the order of 10^7 K) is more abundant than the cold one. Therefore, a more efficient cooling flow can onset in the central regions, leading

to the collapse of the gas and to the accretion of hot gas (now with temperatures of the order of 10^4 K) to the central black hole. This kind of accretion results in a radiatively inefficient accretion flow, creating, therefore, a low power AGN (a source of Fanaroff-Riley Class I, see section 1.5 and Hardcastle et al. (2007)). The presence of such a mechanism in high mass systems is justified also by the reduced efficiency of merger events, due to the higher velocities of galaxies at the center of the protocluster dark matter halo. This limits the availability of cold gas.

On smaller scales, where merger is efficient, wet merger events create abundance of cold gas (temperatures of the order of a few Kelvins) and therefore the quasar mode is preferred. In the quasar mode the black hole is fueled through the accretion of cold gas in a radiatively very efficient accretion disk. The output is therefore a high power Fanaroff-Riley Class II object.

This is in agreement with the work by Hickox et al. (2009), which separates different formation mechanisms for systems of different mass.

After the star formation is quenched by one or all the mechanisms above, galaxies build up the rest of their mass through gas-poor, low mass-ratio, minor dry mergers or through continued, low rate star formation in a disk with spiral features (like the Milky Way). This reproduces also the observed galaxy bimodality in colors, luminosity and other properties. This so-called passive evolution goes on since quenching through present times.

It is in this vision of the formation of galaxies that the present work of thesis is situated.

1.5 The Different Types Of Radio AGNs

It is useful, in the following, to give a brief description of the various types and the different properties of Active Galactic Nuclei.

Active Galactic Nucleus indicates a galaxy whose nuclear emission of light dominates the emission from the rest of the galaxy. The emission in these kind of galaxies is too high to be attributed simply to the star content of the galaxy and therefore another source for the radiation must be found. The current understanding of the phenomenon attributes the source of energy to the presence of a supermassive black hole accreting gas (either hot or cold, as stated in the previous section) in an accretion disk. This is responsible for the observed spectra of AGNs, which ranges from γ -rays to radio wavelengths, and that presents several non thermal features.

There are several classes of AGNs each of which presents different features and properties. For the scope of this work, the most important distinction is the one between Fanaroff-Riley class I and II objects (Fanaroff & Riley, 1974). The distinction between the classes is both morphological (with FR I objects showing symmetric, evident jets, with wide opening angles and FR II showing bright lobes, hotspots, and almost invisible collimated jets) and a distinction based on the power of the radio source. It is this distinction, based on radio power that is interesting for the data analysis presented in this work. In particular, the distinction between FR I and FR II is set to be $P_{1.4GHz} = 10^{24.5} \frac{W}{Hz}$, with low power, FR I objects below the limit and high power, FR II objects above. This difference in radio power seems to be due to both a different source for the gas that is accreted (Hardcastle et al., 2007) and to a different viewing angle of the

source, depending on whether the line of sight passes through the dusty torus or not, as explained in Urry & Padovani (1995).

More exhaustive descriptions of the AGN phenomenon and its properties can be found in Peterson (1997) and in Krolik (1999). Moreover, since this work will concentrate on relatively high redshift radio galaxies, it is useful also the review by Miley & De Breuck (2008) which revises the properties and the recent discoveries on the topic.

1.6 The Thesis

According to the picture of galaxy formation described in the sections above, a few predictions on the trends in the properties of galaxies, quasars and galaxy clusters/groups can be made. The comparison of these predictions with the observed data will give new insights on the problem of galaxy evolution and can help to solve the points which are still not well understood.

If it is accepted the current view that AGNs play a crucial role in quenching the star formation and if it is assumed that the quasar phase is triggered by galaxy mergers and important cooling flows, then galaxies showing the signature of an active nucleus (such as radiogalaxies) should be found more frequently at the center of galaxy clusters and groups. Therefore, the environment around radiogalaxies should show different properties compared to the environment around normal ones.

This thesis has achieved the exposed task, using a sample of radiogalaxies from the Very Large Array part of the Cosmic Evolution Survey (VLA-COSMOS) and studying the environment around them, using galaxies from the COSMOS survey with measured photometric redshifts. The environment has been studied on a 1 Mpc scale, typical of galaxy clusters, and in a thorough manner, by selectioning radiogalaxies and normal ones according to their optical apparent magnitude, stellar mass and specific star formation rate. The environment around radiogalaxies has been compared to an *ad hoc* control sample, made of galaxies extracted randomly from the optical part of the COSMOS survey, in order to match the properties of the radiogalaxies from the VLA-COSMOS sample.

This work is structured as it follows: in chapter 2 a complete description of the COSMOS survey, the VLA-COSMOS and the data sample used for this work is given; in chapter 3 a preliminary analysis of the data sample is performed. Redshift, apparent and total I-band magnitude distributions, together with radio luminosity distribution, are derived and analyzed. Moreover an analysis of the sample specific star formation rate, stellar mass and evolution properties is performed. In chapter 4 the environment is studied and the group richness distributions for various cuts on the sample are shown and described. In chapter 5 a restriction of the study to redshifts $1 \leq z \leq 2$ is analyzed together with a cut in radio luminosity aimed to distinguish between low power radio sources and high power ones, in order to check the importance of the different modes of accretion as described in the above sections. Conclusions are drawn in chapter 6.

Chapter 2

Data Description

IN this chapter the data sample that has been used for the subsequent work will be introduced. The sample consists of optical data (photometry and redshifts) and radio data, both drawn from the Cosmic Evolution Survey (COSMOS).

The chapter is structured as it follows: in section 2.1 a general description of the COSMOS survey is made (concentrating in particular on the optical part, subsection 2.1.1, on the way redshifts are calculated (subsection 2.1.2) and on the radio part, subsection 2.1.3. In section 2.2 the sample which is used for the present work is described, with a small digression on how absolute magnitude, stellar mass and specific star formation rate are derived (subsection 2.2.1).

2.1 The COSMOS Survey

The Cosmic Evolution Survey (COSMOS) is an imaging and spectroscopic survey, realized with a large number of state-of-the-art telescopes in all of the accessible parts of the electromagnetic spectrum.

The field chosen to carry out the survey has been specially selected to be equatorial, so to be readily available to all ground based facilities (optical, infrared and radio telescopes). It is also void of bright ultraviolet and X-Ray sources, while granting a low and uniform galactic extinction (estimated to be $\langle E_{(B-V)} \rangle = 0.02$ mag). The sky region analyzed has an area of about $1.4^\circ \times 1.4^\circ$ and is centered at R.A. (J2000.0) = $10^h 00^m 28.6^s$ and Dec (J2000.0) = $+02^\circ 12' 21.0''$. The number of sources expected in such field is about 2×10^6 , out to a redshift of $z = 6$. An overview of the COSMOS scientific goals, field selection and observational goals may be found in Scoville et al. (2007b).

The peculiarity of the COSMOS survey is its large quantity of data in a great number of different wavelengths. The COSMOS field has been studied in all of the accessible parts of the electromagnetic spectrum. In this chapter mainly the radio sub-sample (named VLA-COSMOS survey) and the optical one will be discussed. Nevertheless it is important to describe briefly also the other sub-samples which constitute the COSMOS survey as a whole. The COSMOS field has been studied in wavelengths ranging from X-Ray using XMM-Newton (Hasinger et al., 2007) and Chandra (Elvis et al., 2009), to UV with the GALEX instrument (Zamojski et al., 2007), optical (which will be described in detail in

the following section), IR with the SPITZER instrument (named S-COSMOS survey, Sanders et al. (2007)), millimetre wavelengths with the MAMBO instrument (named COSBO survey, Bertoldi et al. (2007)) and radio wavelengths, described in the following.

In tables 2.1 and 2.2 a complete list of the bands observed in the COSMOS Survey is given. For every band the wavelength and the telescope used for observations are given, together with a limiting magnitude or a limiting flux of the measurements taken.

Filter	Telescope	Effective λ	FWHM	Limiting Magnitude
u^*	CFHT	3911.0	538.0	26.5
B_J	Subaru	4439.6	806.7	27.3
V_J	Subaru	5448.9	934.8	26.6
g^+	Subaru	4728.3	1162.9	27.0
r^+	Subaru	6231.8	1348.8	26.8
i^+	Subaru	7629.1	1489.4	26.2
i^*	CFHT	7628.9	1460.0	24.0
z^+	Subaru	9021.6	955.3	25.2
J	UKIRT	12444.1	1558.0	23.7
K_S	NOAO	21434.8	3115.0	
K	CFHT	21480.2	3250.0	23.7
IA427	Subaru	4256.3	206.5	
IA464	Subaru	4633.3	218.0	
IA484	Subaru	4845.9	228.5	
IA505	Subaru	5060.7	230.5	
IA527	Subaru	5258.9	242.0	
IA574	Subaru	5762.1	271.5	
IA624	Subaru	6230.0	300.5	
IA679	Subaru	6778.8	336.0	
IA709	Subaru	7070.7	315.5	
IA738	Subaru	7358.7	323.5	
IA767	Subaru	7681.2	364.0	
IA827	Subaru	8240.9	343.5	
NB711	Subaru	7119.6	72.5	
NB816	Subaru	8149.0	119.5	
IRAC1	Spitzer	35262.5	7412.0	23.9
IRAC2	Spitzer	44606.7	10113.0	23.9
IRAC3	Spitzer	56764.4	13499.0	23.9
IRAC4	Spitzer	77030.1	28397.0	23.9
FUV	GALEX	1551.3	230.8	25.5
NUV	GALEX	2306.5	789.1	25.5

Table 2.1: Bands Of Observations

In particular these bands are those used to calculate the photometric redshifts as described in the following section. Other bands (table 2.2) have to be added to the list.

Filter	Telescope	Limiting Magnitude
MIPS 24 μ m	Spitzer	
MIPS 70 μ m	Spitzer	
MIPS 160 μ m	Spitzer	
ACS F475W	HST	
ACS F814W	HST	
NICMOS F160W	HST	
WFPC2 F300W	HST	
WFPC2 F450W	HST	
u'	SDSS	22.0
g'	SDSS	22.2
r'	SDSS	22.2
i'	SDSS	21.3
z'	SDSS	20.5
1.4 GHz	VLA	30 μ Jy ¹
0.5 \div 2 keV	XMM	$5 \times 10^{-16} \frac{erg}{cm^{-2} \times s^{-1}}$
2 \div 10 keV	XMM	$3 \times 10^{-15} \frac{erg}{cm^{-2} \times s^{-1}}$
5 \div 10 keV	XMM	$7 \times 10^{-15} \frac{erg}{cm^{-2} \times s^{-1}}$
0.5 \div 2 keV	Chandra	$1.9 \times 10^{-16} \frac{erg}{cm^{-2} \times s^{-1}}$
2 \div 10 keV	Chandra	$7.3 \times 10^{-16} \frac{erg}{cm^{-2} \times s^{-1}}$
5 \div 10 keV	Chandra	$5.7 \times 10^{-16} \frac{erg}{cm^{-2} \times s^{-1}}$

Table 2.2: Additional Bands

2.1.1 The Optical Sample Of The COSMOS Survey

Before starting to describe the optical observations of the COSMOS project, it is necessary to make a *distinguo* regarding the purpose of the observations. In fact, the COSMOS optical survey has been realized in two separate steps, namely the imaging and the measure of photometry and spectroscopy of the sources in the COSMOS field.

Realizing the imaging at optical frequencies has involved mainly three facilities, both ground based and spaceborne: the Hubble Space Telescope (HST), the 8.2 m Subaru Telescope and the 3.6 m Canada-France-Hawaii Telescope (CFHT), both on Mauna Kea Observatory, Hawaii. A complete description of the HST data can be found in Scoville et al. (2007a). This work will describe in detail only the photometry and spectroscopy part of the optical survey, since these data are those which have been used to calculate the redshifts used for the calculations of the following chapters.

The spectrophotometric data have been taken with several facilities, such as the Kitt-Peak National Observatory (KPNO) and Cerro Tololo International Observatory (CTIO) 4m telescopes, the Suprime-Cam of the 8.2m Subaru Telescope and the 3.6m CFHT telescope. A description of the procedure used for data reduction may be found in Taniguchi et al. (2007) and in Capak et al. (2007). In these works the quality of data is investigated, the accuracy of the photometry is believed to be of the order of 6%. Moreover, limiting magnitudes are derived and estimated to be a little greater than 27 mag.

2.1.2 COSMOS Photometric Redshifts

The importance of realizing a good compilation of photometric data is that photometric redshifts can be calculated from the photometry of galaxies. The best way to measure the redshift of a galaxy is through spectroscopy, measuring the shift of the emission or absorption lines of its spectrum from the position that they have at rest. For very distant galaxies or for faint ones, accurate spectroscopy is not available and measuring its spectroscopic redshift is impossible. It is nevertheless possible the measurement of photometric redshifts, which are less accurate, but can be measured for galaxies with fainter magnitudes. Moreover the measurement of spectroscopic redshifts for a large number of objects is difficult, since the whole procedure is very time-consuming and therefore not convenient. The photometric redshift method, instead is efficient and viable also on large number of objects.

For the COSMOS survey, photometric redshifts have been calculated using 30 broad-, intermediate- and narrow-bands from UV to mid-IR frequencies (see tables 2.1 and 2.2). The method used in order to derive these redshifts is the χ^2 template-fitting and is described in Ilbert et al. (2009). Observed Spectral Energy Distributions (SED) of the galaxies of the sample are fitted with template SEDs of galaxies of known type, leaving redshift as a free parameter and trying to minimize the χ^2 for the fit. This procedure is achieved with the *Le Phare* code (S. Arnouts & O. Ilbert). The redshifts obtained with the procedure described have been compared with those obtained using the zCOSMOS spectroscopic survey (Lilly et al., 2007). The same procedure has also been used on data coming from the Canada-France-Hawaii Telescope (CFHT) Legacy Survey (Ilbert et al., 2006). As said before, the procedure used to derive photometric redshifts for the galaxies of the COSMOS survey utilizes the *Le Phare* code to fit galaxy templates to SEDs constructed with fluxes measured in several bands. What done by Ilbert et al. (2009) improves what already achieved by Mobasher et al. (2007). In Ilbert et al. (2009) the template database has been renewed, including templates from Polletta et al. (2007) and from Bruzual & Charlot (2003). Moreover, a number of emission lines are used in the SED templates which were not included in previous works and sistematic zero point offsets are derived and applied to the calculations. These zero point offsets are used to correct for errors in the template fitting procedure, such as those produced by uncertainties due to band zero-point calibration and uncertainties in the modeling of the templates). All of these errors produce a sistematic offset between the values from the template and the data in one or more bands, which are corrected with a zero point offset.

The procedure described above and in the references uses the *Le Phare* code to minimize the following expression:

$$\chi^2(z, T, A) = \sum_{f=1}^{N_f} \left(\frac{F_{obs}^f - A \times F_{pred}^f(z, T) \cdot 10^{-0.4s_f}}{\sigma_{obs}^f} \right)^2 \quad (2.1)$$

where $F_{pred}^f(z, T)$ is the flux predicted for a template T at a redshift z , F_{obs}^f is the observed flux and σ_{obs}^f is the associated error. The sum is extended to all the bands available for calculation and s_f is the sistematic zero point offset, a list of which can be found in Table 1 of Ilbert et al. (2009) along with a description of the improvement given by the inclusion of these values in the formula. The

output of this minimization is the redshift Probability Distribution Function (PDFz), in the form of

$$p(z, T) = e^{-\frac{\chi(z, T)^2}{2}} \quad (2.2)$$

which provides the maximum and minimum redshift for every object. From this distribution the redshift of each galaxy can be calculated by solving

$$z = \frac{\int_{T_{min}}^{T_{max}} \int_{z_{min}}^{z_{max}} p(z, T) z dz dT}{\int_{T_{min}}^{T_{max}} \int_{z_{min}}^{z_{max}} p(z, T) dz dT} \quad (2.3)$$

The result of this procedure is about 1.5×10^6 galaxies with a confirmed photometric redshift.

The accuracy of the photometric redshifts is estimated in two separate ways: by comparing the photometric redshift and the spectroscopic redshift of those objects for which both are measured and by analysing the width of the PDFz. The first method gives an accuracy of the photometric redshift of:

$$\sigma_{\frac{\Delta z}{1+z_s}} = 0.007 \div 0.06 \quad (2.4)$$

where z_s is the spectroscopic redshift, z_p is the photometric redshift and $\Delta z = z_s - z_p$.

The change of about one order of magnitude of the error range is due to a small trend of the uncertainty of photometric redshift with apparent magnitude. In particular, two spectroscopic samples have been used to calculate the errors. The values above refer to the zCOSMOS survey (Lilly et al., 2007), the interval is due to the fact that the zCOSMOS is composed of two different subsamples, the zCOSMOS-bright (with $i^+ < 22.5$) and the zCOSMOS-faint (median $i^+ \sim 24$). It can be seen that the error on photometric redshift is smaller for brighter galaxies, while it is slightly larger for fainter ones. In figure 2.1 the comparison between photometric and spectroscopic redshift for the galaxies from the zCOSMOS-bright sample is shown. The dotted and dashed lines are for $z_p = z_s \pm 0.15(1 + z_s)$ and $z_p = z_s \pm 0.05(1 + z_s)$, respectively. The 1σ dispersion, the fraction η of catastrophic failures ($\eta = 0.7\%$) and the median apparent magnitude are listed in the top-left corner. It can be seen that there is a good agreement between the photometric and spectroscopic redshift. For a complete description of the figure see Ilbert et al. (2009).

Another sample used is the so called ‘‘MIPS-spectro-z’’, composed of galaxies with infrared data, coming from the S-COSMOS Survey, realized with the Spitzer Space Telescope (see Sanders et al. (2007)). The comparison yields error estimates of the order of

$$\sigma_{\frac{\Delta z}{1+z_s}} = 0.009 \div 0.053 \quad (2.5)$$

for galaxies ranging from $i^+ < 22.5$, to $22.5 < i^+ < 24$ and to $24 < i^+ < 25$. Again, errors are lower for brighter galaxies.

In figure 2.2 the comparison between photometric and spectroscopic redshift for the zCOSMOS-faint and the MIPS-spectro-z sample are given. In the left panel the zCOSMOS-faint sample is analysed. The dotted and dashed lines are, as before, for $z_p = z_s \pm 0.15(1 + z_s)$ and $z_p = z_s \pm 0.05(1 + z_s)$, respectively. Again in the top-left corner of the plot the 1σ dispersion, the fraction $\eta = 15.3\%$

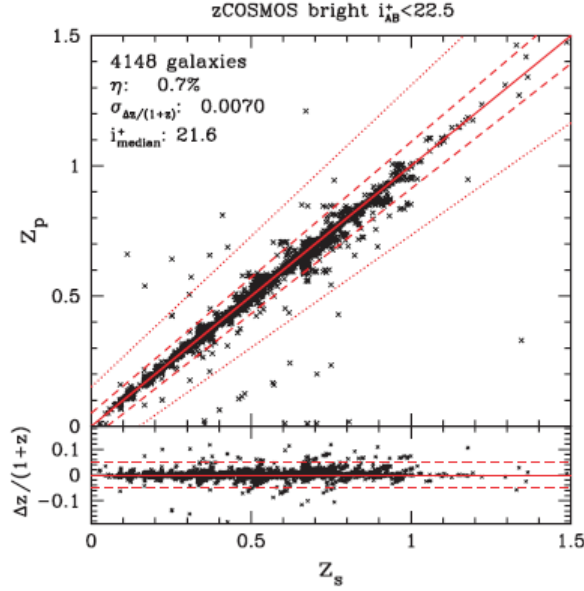


Figure 2.1: Comparison between spectroscopic and photometric redshift, zCOSMOS-Bright. This figure is taken from Ilbert et al. (2009).

of catastrophic failures and the median apparent magnitude are listed. The open triangles are objects with a secondary peak in the redshift probability distribution function. This time there is a lower agreement between the two measurements, as stated in the text. Also the fraction of catastrophic failures is higher. In the right panel of figure 2.2 the analysis is focused on the galaxies from the MIPS-spectro-z sample. The dotted and dashed lines have the same meaning as before, and the same informations are given in the plot ($\eta = 0.0\%$). The different symbols are for different magnitude ranges: bright sample $i^+ < 22.5$ (black), faint sample $22.5 < i^+ < 24$ (red) and very faint sample $24 < i^+ < 25$ (green). For the infrared sample the agreement between spectroscopic and photometric redshift is high.

The second method, which uses the width of the PDF_z to determine errors for the photometric redshifts, gives:

$$\sigma_{\Delta z} = 0.02 \div 0.19 \quad (2.6)$$

with similar trends with apparent magnitudes as stated above for the precedent method.

For the present work an error of $\sigma_{\frac{\Delta z}{1+z_p}} = 0.06$ will be assumed.

Another source of uncertainties in the photometric redshift determination which must be kept in mind are the so called *catastrophic errors*. Catastrophic errors are defined those objects for which $\frac{|z_p - z_s|}{1+z_s} > 0.15$. It is estimated that the fraction η of catastrophic errors rises from 1% to 20% going from $i^+ < 22.5$ to $i^+ \sim 24$.

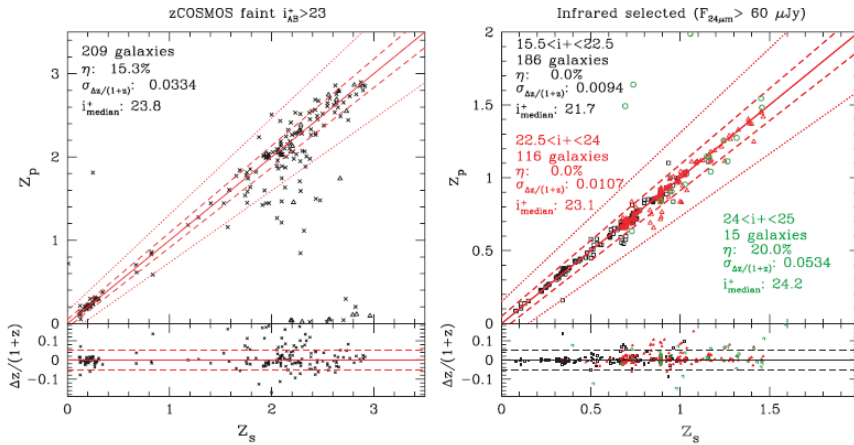


Figure 2.2: Left Panel: Comparison between spectroscopic and photometric redshift, zCOSMOS-Faint. Right Panel: Comparison between spectroscopic and photometric redshift, MIPS-Spectro-z. This figure is taken from Ilbert et al. (2009).

2.1.3 The VLA-COSMOS Survey

The radio part of the COSMOS survey was realized with the Very Large Array (VLA) instrument of the National Radio-Astronomy Observatory (NRAO). The VLA-COSMOS survey can be considered a good balance between large surveys, with great source numbers, great field of view but high limiting fluxes, and small and deep surveys, with small fields, small source numbers but small limiting flux. In fact, with its about $11 \mu Jy$ r.m.s. sensitivity and great number of sources studied, it allows to analyze statistical samples of both Radio-Loud and Radio-Quiet Quasars even at high redshifts.

The whole survey was divided into three distinct projects: the Pilot Project (Schinnerer et al., 2004) is a first look at the COSMOS field, to decide the observing strategy for more extended and complete surveys; the Large Project (Schinnerer et al. (2007), Bondi et al. (2008)) has observed the whole COSMOS field, while the Deep Project (Schinnerer et al., 2010) has observed the central part with improved sensitivity.

The VLA-COSMOS Large Project survey (Schinnerer et al., 2007) has been carried out with the Very Large Array in its configuration A. This grants a resolution of about $1.5''$ at Full Width Half Maximum (FWHM) in the observation wavelength of 1.4 GHz, but mosaicing was needed to cover the full COSMOS field. A total of 23 pointings was necessary to cover the whole COSMOS field, for 240 hours of observation, performed between 2004 and 2005. Images were reduced using Astronomical Imaging Processing System (AIPS), following the usual VLA data reduction procedure. The VLA-COSMOS Large Project survey has been compared to other surveys with similar properties, such as the NRAO VLA Sky Survey (NVSS) and the 20 cm FIRST survey, finding good agreement between the results (see figure 2.3). A further analysis of the biases affecting the VLA-COSMOS Large Project survey may be found in Bondi et al. (2008), along with correction factors and a study of the radio source counts.

The VLA-COSMOS Deep Project survey (Schinnerer et al., 2010) is an additional set of observations at 1.4 GHz, taken with the VLA in its A configuration, which have been carried out for the central $50' \times 50'$ with a resolution of $2.5''$ at FWHM. The data reduction procedure is the same as for the Large Project, in order to be able to unify the two samples and to create a Joint Catalog.

The first attempt to join the Large and Deep catalogs has produced the Revised Large Catalog, which contains 2417 sources at 5σ detection. In this new version of the Large Catalog are also implemented the corrections explained in Bondi et al. (2008), while spurious detections have been identified and removed from the sample.

The sources have been detected by distinguishing them from the background noise. This is achieved by selecting only those sources with a peak flux over a threshold defined as a five times the r.m.s. noise. Sources are extracted and by the comparison of total and peak flux are discriminated into resolved and unresolved.

Figure 2.3 shows the radio source counts as a function of radio flux, as found and described in Bondi et al. (2008). The VLA-COSMOS data are compared to data coming from other surveys, showing the large agreement between various data sets. This figure is to be compared with picture 3.1 which shows the same plot for the sample used for this work.

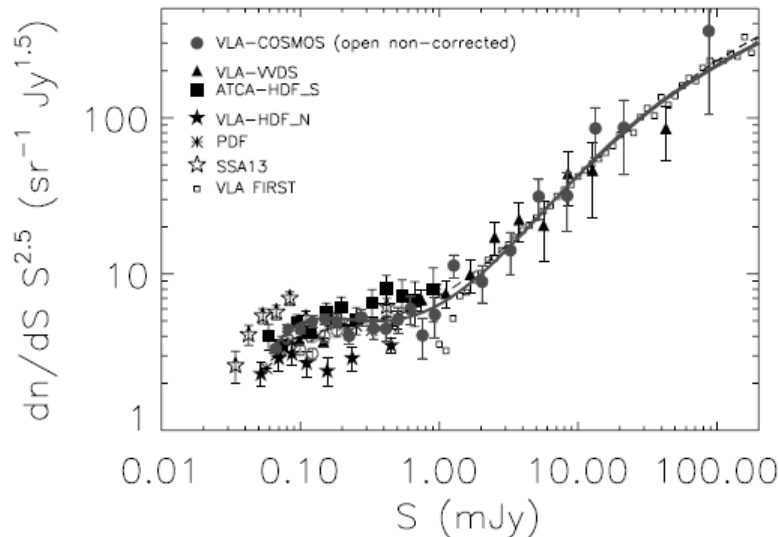


Figure 2.3: Radio Source Counts (From Bondi et al. (2008)). The various symbols refer to various radio surveys as explained in the image (see also the image caption in the reference).

It is worth spending a few words on the method used to obtain optical identifications of the radio sources. The data used for this work are taken from Ciliegi (private communication) but the method used to optically identify the radio sources is the one described in Ciliegi et al. (2003) and Ciliegi et al. (2005).

For every source from the Revised Large Catalog, extracted in the way de-

defined above, optical counterparts are determined by comparing the position of the source from the radio observations to the position from the optical ones. Systematic differences between the two sets of coordinates (called positional offset, indicated with r and taken to be $r = 3''$) are eliminated. At this point the likelihood ratio technique is applied. This technique, developed by Sutherland & Saunders (1992) and described in Ciliegi et al. (2003) and Ciliegi et al. (2005) is based on the calculation of the quantity called Likelihood Ratio (LR)

$$LR = \frac{q(m)f(r)}{n(m)} \quad (2.7)$$

where $q(m)$ is the expected distribution as a function of magnitude of the optical counterparts within a small radius from the radio source, $f(r)$ is the probability distribution function of the positional errors, assumed to be equal in the two coordinates and $n(m)$ is the surface density of background objects with magnitude m . As a functional form for $f(r)$ it has been chosen a gaussian distribution, with a standard deviation σ which takes into account the combined effect of the radio and the optical positional uncertainties

$$f(r) = \frac{1}{2\pi\sigma^2} e^{-\frac{r^2}{2\sigma^2}} \quad (2.8)$$

where σ is the average between $\sigma_x = (\sigma_{op}^2 + \sigma_\alpha^2)^{\frac{1}{2}}$ and $\sigma_y = (\sigma_{op}^2 + \sigma_\delta^2)^{\frac{1}{2}}$, with σ_{op} as the error on the optical position and σ_α and σ_δ are the errors on Right Ascension and Declination for the radio position. Therefore the likelihood ratio is defined as the ratio between the probability that the optical source is the correct identification of the radio one and the corresponding probability for a background, unrelated object. If, for a given optical candidate with magnitude m and positional offset r from the radio source position, the probability p that the true source lies in an infinitesimal interval of $r \pm \frac{dr}{2}$ and in a magnitude interval $m \pm \frac{dm}{2}$ is calculated, on the assumption that the positional offsets are independent of the optical properties, then p is given by the formula

$$p = q(m)dm \times 2\pi r f(r)dr \quad (2.9)$$

Once the LR has been calculated, the reliability of every optical counterpart is estimated in the following way

$$Rel_j = \frac{(LR)_j}{\sum_i (LR)_i + (1 - Q)} \quad (2.10)$$

where the sum is over the set of all optical candidates for the particular radio source and Q is the probability that the optical counterpart of the source is brighter than the magnitude limit of the optical catalogue. Therefore

$$Q = \int_0^{m_{lim}} q(m)dm \quad (2.11)$$

The likelihood ratio is calculated for all the optical counterpart candidates. A threshold value is defined (LR_{tr}) and only those sources having $LR > LR_{tr}$ are considered as optical counterparts for the radio sources.

2.2 The Data Sample For This Work

The sample that has been used for the present work is a compilation of data drawn both from the optical part of the COSMOS survey and from the radio part. The sample is composed of the Revised Large Catalog (2417 sources) of the VLA-COSMOS survey for the radio part and of the optical part of the COSMOS survey for the visible wavelengths part, with photometric redshifts measured from IR-Optical photometry (1482993 sources). For the radio sample, of the 2417 sources, 2020 have been identified, therefore reaching a completeness of 84%. From the likelihood method, 26 of the identified sources are spurious detections, therefore the reliability of the radio sample is 98.7%.

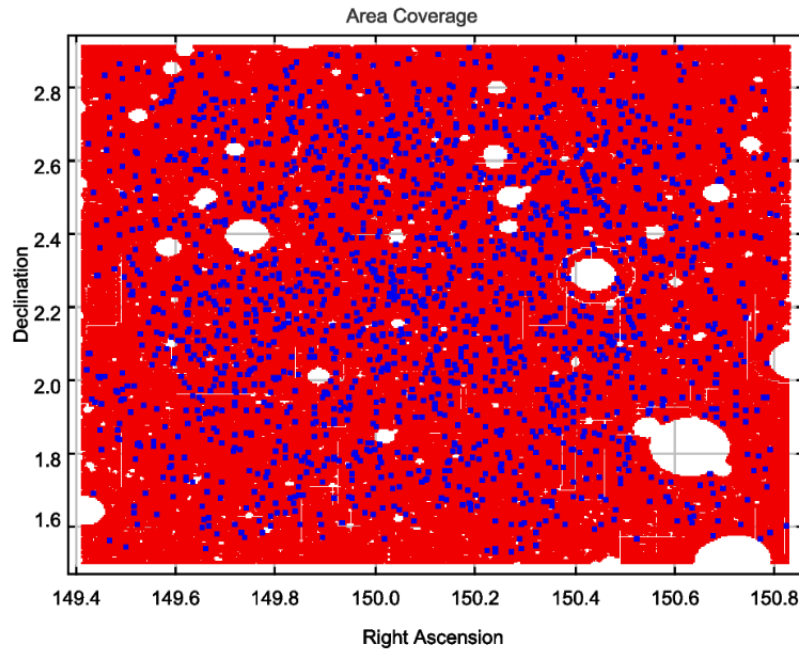


Figure 2.4: Area Coverage. The red dots refer to the optical sample, the blue dots refer to the radio sample.

Figure 2.4 shows that the distribution of the sources in the sky area covered by the COSMOS survey is roughly the same for the optical part (red dots) and for the radio part (blue dots) of the sample used. The area covered by both samples is of $1.4^\circ \times 1.4^\circ$. In the figure, the white areas are saturated stars that have been masked out in order to better reduce and analyse the data.

For every source of the radio part of the sample (hereafter “radio sample”) are given: ID in the the VLA-COSMOS Revised Large Catalog, peak of the radio flux, total radio flux, ID of the galaxy from Capak et al. (2007) (*i.e.* the photometric redshift compilation, hereafter “optical sample”) and apparent magnitudes in several bands. For the optical sample are given the ID of the galaxy from Capak et al. (2007), Right Ascension, Declination, photometric

redshift, apparent magnitudes in several bands, absolute magnitudes in several bands, stellar mass and star formation rate. The IDs of the galaxies in the various samples are those taken from Capak et al. (2007) because the catalog described in that work constitutes the photometric base for the photometric redshift catalogue described in Ilbert et al. (2009).

As will be described in the following sections (in particular section 3.1) the optical sample and the radio sample have been matched, to create the radio-optical sample. This sample is constituted of radiogalaxies with a measured photometric redshift and counts 1806 elements.

A summary of the important quantities defining the sample used for the work and listed in the previous sections can be found in table 2.3.

Quantity	Value
Galactic Extinction Of The Field	$\langle E_{(B-V)} \rangle = 0.02$ mag
Area Of The Field	$1.4^\circ \times 1.4^\circ$
Coordinates Of The Center Of The Field	R.A. = $10^h 00^m 28.6^s$ Dec = $+02^\circ 12' 21.0''$
Maximum Redshift	$z = 6$
Limiting Magnitude	27 mag
Redshift Accuracy	$\sigma_{\frac{\Delta z}{1+z_p}} = 0.007 \div 0.06$
Radio Sensitivity	11 μJy
Resolution Of The Radio Sample (FWHM)	1.5''
Wavelength Of The Radio Survey	1.4 GHz
Completeness Of The Radio Sample	84%
Reliability	98.7%
Number Of Sources Of The Optical Sample	1482993
Number Of Sources Of The Radio Sample	2417
Number Of Sources Of The Radio-Optical Sample	1806

Table 2.3: The Sample

2.2.1 How Absolute Magnitude, Stellar Mass And Specific Star Formation Rate Are Derived

As said in the above section, some quantities are derived during the template fitting procedure. This has been achieved by O. Ilbert in the following way.

For the present sample, absolute magnitudes are calculated using the method described in Dahlen et al. (2005), using galaxy templates from Polletta et al. (2007) and Bruzual & Charlot (2003). This method consists in inserting a term that takes account of the *K-correction* due to cosmological effects on the galaxy flux in the usual formula for deriving absolute magnitudes. With this term the formula becomes

$$M_Y = m_X - 5 \log\left(\frac{D_L(z)}{10pc}\right) - K_{XY}(z; T) \quad (2.12)$$

where M_Y is the absolute magnitude in rest-frame filter Y, m_X is the apparent magnitude in the observed filter X, $D_L(z)$ is the luminosity distance at redshift z and $K_{XY}(z; T)$ is the K-correction at redshift z , for galaxy template T,

correcting from observed filter X to rest frame filter Y. The K-correction compensates two ways in which a galaxy flux changes due to cosmological effects. The first one is an actual reduction of the flux that increases with distance. More distant galaxies appear fainter than less distant ones. The second effect is that the wavelengths of the light emitted are shifted towards longer values than the rest frame ones. As an example, the light that would be observed in a rest-frame blue filter is observed here in a red filter. In order to not make mistakes in calculating the absolute magnitudes of a galaxy in several bands it is therefore necessary to correct for this effect, introducing the term in the equations above using the best-fit template used for the determination of the photometric redshift.

A detailed description of the procedure, together with functional forms for the luminosity distance and the K-correction, can be found in the appendix of Dahlen et al. (2005).

The specific star formation rate is defined as

$$\log\left(\frac{SSFR}{yr^{-1}}\right) = \log\left(\frac{SFR}{M_{\odot} yr^{-1}}\right) - \log\left(\frac{M^*}{M_{\odot}}\right) \quad (2.13)$$

where SFR is the star formation rate in Solar masses per year.

The star formation rate and the stellar mass entering in the equation above are calculated through template fitting. For the SFR, once the galaxy kind has been identified, the color indexes are derived in several bands for both the template and the galaxy. SFR is obtained by the comparison of the two sets of color indexes.

Stellar mass is derived in a similar way. Luminosity is converted into mass using the mass to light ratio. Stellar mass is derived for the galaxy using a formula linking mass, mass to light ratio and absolute magnitude. The same quantities are derived for the templates too, using a Chabrier IMF and templates from Polletta et al. (2007) and Bruzual & Charlot (2003). A fit of the templates to the observations gives the quantities needed. A complete description of the method can be found in Mobasher et al. (2007) and in Ilbert et al. (2010).

2.3 Conclusions

In this chapter a general description of the data sample used for this work has been given.

The data sample for the present work comes from the Cosmic Evolution Survey (COSMOS). The survey is a multiwavelength compilation of data, taken with several instruments. All of the data come from a $1.4^{\circ} \times 1.4^{\circ}$ area of sky which has been observed in bands ranging from X-rays to radio wavelengths. For the present work only data in two of these bands will be taken into account, namely the optical part and the radio part of the survey.

The optical part consists in data in several bands, listed in table 2.1. From these observations both imaging and photometry of the sources have been realized. The photometrical data have been used to obtain photometrical redshifts for the sources, through a template fitting procedure which makes use of χ^2 minimization accomplished with the *Le Phare* code. The error on the photometric redshifts has been assumed to be of the order of $\sigma_{\frac{\Delta z}{1+z_p}} = 0.06$, a quantity which has been estimated through both comparison with spectroscopic redshifts and

the redshift probability distribution function. From the same procedure, absolute magnitude, stellar mass and specific star formation rate have been derived, with the method described above.

The radio part is made of VLA data at 1.4 GHz of the same area of sky. The sources in the sample have been optically identified and matched to the optical sample. The radio sensitivity is expected to be $11 \mu Jy$.

The sample for the present work is therefore composed of 1482993 galaxies with optical data (the optical sample) and 2417 galaxies with radio data and optical identification (the radio sample). A matching of the two produces the radio-optical sample, composed of 1806 galaxies with radio and optical data and a measured photometric redshift, which will be analyzed in the following chapters.

Chapter 3

Preliminary Data Analysis

IN this chapter a preliminary analysis of the data sample will be discussed. The data sample has been analyzed with the Interactive Data Language software (IDL)¹ and the Tool for OPERations on CAtalogues and Tables (TOPCAT)². They are both useful tools to analyze compilations of data.

IDL is an environment developed to operate mathematical and statistical calculations on numerical data. It possess a wide variety of routines which allow to perform advanced mathematical operations which range from array manipulation to curve fitting, to plotting and statistical calculations. It is quite accurate and user-friendly, allowing to operate advanced calculations in a fast and reliable way.

TOPCAT is a software useful to manipulate a great amount of data that are already formatted in a tabular way. It is ideal to perform fast statistics and plots onto catalogs and tables of great dimensions. It is a useful program to have a quick look through a great amount of data although being less reliable than IDL.

The chapter is structured in the following way: matching procedures are explained in section 3.1, redshift, apparent magnitude and radio flux distributions are presented in section 3.2 and the correlations between specific star formation rate and stellar mass and between absolute magnitude and redshift are analyzed in section 3.3.

3.1 Matching

The data sample used for the present work is composed of a radio sample and of an optical sample (section 2.2). The first operation performed on the data has been the matching of the two data samples. In particular, the sources in the radio sample which were also present in the optical sample were identified. The matching has been realized with TOPCAT through the `MATCH` command, setting the options “Algorithm” to `EXACT VALUE`, “Match Selection” to `BEST MATCH`, `SYMMETRIC` and “Join Type” to `1 AND 2`. The match has been executed

¹<http://www.exelisvis.com/ProductsServices/IDL.aspx>

²<http://www.star.bris.ac.uk/~mbt/topcat/>

between the file columns containing the ID of the sources from Capak et al. (2007).

This operation results in a sample of 1806 radiogalaxies with measured photometric redshift (hereafter this sample will be called the “radio-optical sample”). For every galaxy in the radio-optical sample are given the same fields which are listed in section 2.2 for both the optical and the radio sample.

3.2 Radio Flux, Redshift And Apparent Magnitude Distributions

A first analysis of the data consist in constructing and comparing apparent magnitude, redshift and radio flux distributions for the optical sample, the radio sample and the radio-optical sample.

3.2.1 Radio Flux Distribution

For every galaxy in the samples both the peak radio flux and the total radio flux are given. The radio flux of the peak is the one used to detect a source and distinguish it from the background noise. The ratio of the peak radio flux to the total radio flux is used to determine whether the source is extended or not.

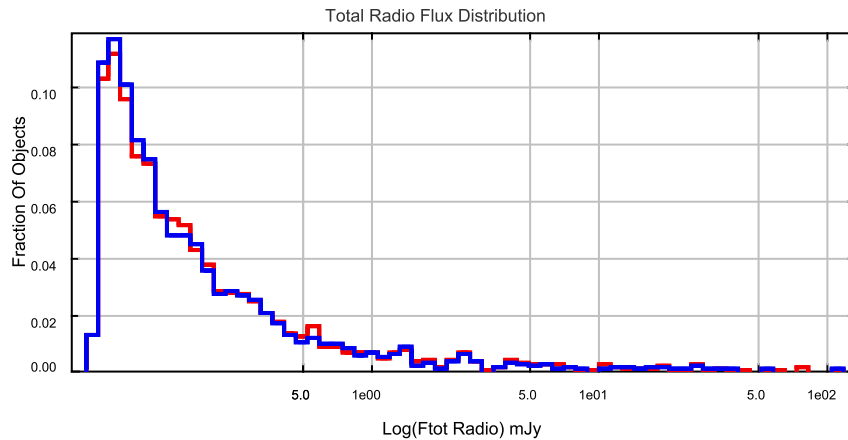


Figure 3.1: Total Radio Flux Distributions. The red line shows the distribution for the radio sample. The blue line shows the distribution for the radio-optical sample. The plot is normalized to 1.

Figure 3.1 shows the total radio flux distribution for the radio sample and the radio-optical sample. The red line shows the distribution for the radio sample, while the blue line shows the distribution for the radio-optical sample. The plot depicts a similarity between the two histograms, not showing any difference between the properties of the total radio emission of the two samples. Both samples have comparable mean total radio fluxes (respectively 0.59 mJy for the

radio-optical sample and 0.77 mJy for the radio sample) and the two curves peak at approximately the same value and they both have a long tail. The plot is normalized to unity.

3.2.2 Apparent I-Band Magnitude Distributions

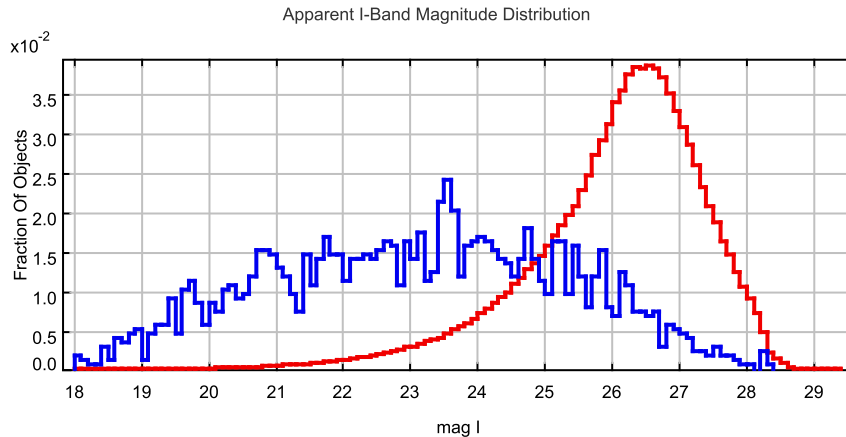


Figure 3.2: Apparent I-band Magnitude Distributions. The red line shows the distribution for the optical sample. The blue line shows the distribution for the radio-optical sample. The plot is normalized to unity.

Figure 3.2 shows the distributions for the apparent I-band magnitude, for the optical sample and the radio-optical sample. This plot is also normalized to unity. The red line shows the distribution for the optical sample. The blue line shows the distribution for the radio-optical sample, with the magnitude taken from the optical sample. This is possible because in the matching procedure the radio sample and the optical sample were unified while keeping distinct the quantities given for each entry of each sample (section 3.1). The mean I-band apparent magnitude of the radio-optical sample is close to 23. The distribution is quite smooth, not showing any particular peaks. Quite different is instead the distribution for the optical sample (red line). It shows a pronounced peak at about mag 26.5, having the bulk of the data at fainter magnitudes than the other sample (mean I-band magnitude is 26). After the peak it shows a steep decrease, probably due to the great difficulty in detecting objects fainter than magnitude 26.5. Therefore, in the following it will be often considered a cut in apparent I-band magnitude at 26.5 mag, considering this value the completeness limit of the sample.

3.2.3 Redshift Distributions

More interesting is the study of the redshift distributions.

Figure 3.3 shows the redshift distributions for the optical sample and for the radio-optical sample. A cut has been made, selecting only those galaxies with

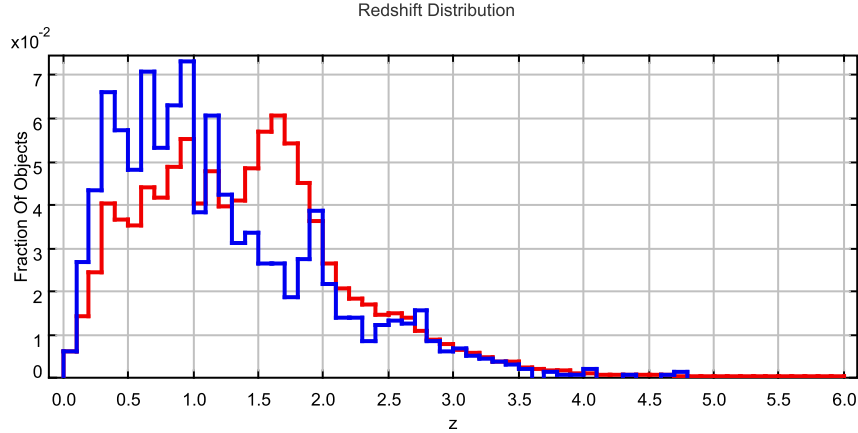


Figure 3.3: Redshift Distributions. The red line shows the distribution for the optical sample. The blue line shows the distribution for the radio-optical sample. A cut has been made, selecting only those galaxies with apparent I-band magnitude lower than 26.5. The plot is normalized to 1.

apparent I-band magnitude lower than 26.5. The red line shows the distribution for the optical sample. The blue line shows the distribution for the radio-optical sample. The plot is again normalized to unity as described above. In this case, a marked difference between the two curves can be easily seen, emphasizing distinct properties of the two samples. The optical sample has a wider distribution, two peaks, one at about $z = 1$ and the other at $z \sim 1.7$. The radio-optical sample has a different distribution, with more values in the range $0 < z < 1.5$. This sample is therefore made of closer galaxies than the optical sample. Although the redshift peak is at $z = 0.7$, the sample presents a consistent tail extending to high redshift. This tail allows us to concentrate on samples which are not local, therefore opening to the possibility of considerations on galaxy evolution. Mean redshifts for the two samples are also different, respectively 1.2 for the radio-optical sample and 1.7 for the optical one. It has been calculated that 52% of the total optical sample and 35% of the total radio-optical sample have redshift between 1 and 2. Applying the cut in apparent I-band magnitude to 26.5, the fractions of galaxies with redshift between 1 and 2 change to 47% for the optical sample and to 34% for the radio-optical sample. The change is therefore greater for the optical sample than for the radio-optical one.

In the redshift distribution of the radio-optical sample is quite peculiar the peak at $z = 2$. It could be due either to a real concentration of galaxies around that redshift (such as a cluster of galaxies, whose members are all at the same distance) or to galaxies whose redshift has been miscalculated (catastrophic errors, see section 2.1.2). In order to distinguish between the two situations it is useful to have a look at the distribution on the plane of the sky of the galaxies composing the redshift peak, *i.e.* chosen to have $1.75 < z < 2.25$, showed in figure 3.4.

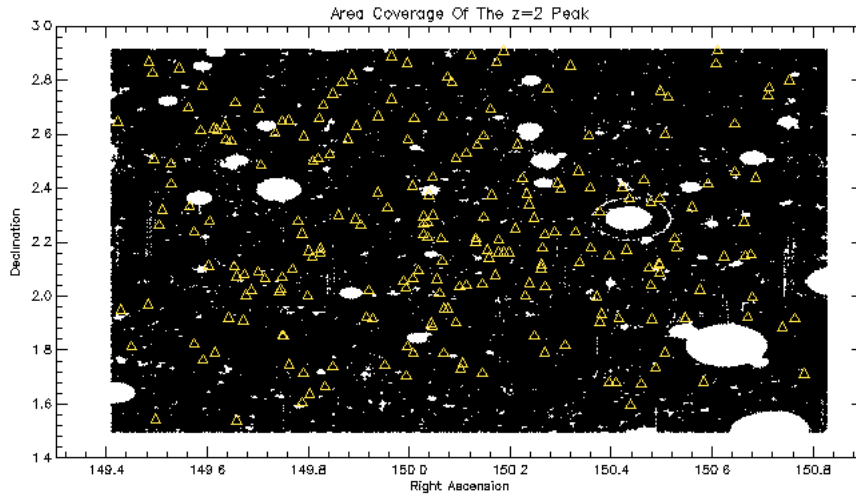


Figure 3.4: Distribution on the plane of the sky of galaxies composing the peak at $z = 2$. The black stars represent the total optical sample, while the yellow triangles represent the galaxies from the radio-optical sample with redshift between 1.75 and 2.25.

From this figure it can be seen that the galaxies of the radio-optical sample composing the $z = 2$ peak are uniformly distributed on the plane of the sky. The same test has been repeated progressively restricting the redshift range: the uniformity of the distribution of the galaxies composing the peak on the plane of the sky seems to be maintained. This means that the peak itself could be due to errors in the template fitting procedure. It is nevertheless impossible to distinguish between the case of errors in the template fitting procedure and the case of the presence of a Large Scale Structure (LSS) in the distribution of the galaxies composing the peak. In fact, such a structure as a Wall, could give the same distribution in redshift while maintaining a uniform distribution of the galaxies in the plane of the sky.

A summary of the results of the section can be found in table 3.1.

Quantity	Radio Sample	Optical Sample	Radio-Optical Sample
Number Of Galaxies	2417	1482993	1806
Mean Total Radio Flux	0.77 mJy	–	0.59 mJy
Mean I-Band Apparent Magnitude	–	26	23
Mean Redshift	–	1.7	1.2

Table 3.1: Mean Total Radio Flux, I-Band Apparent Magnitude And Redshift.

3.3 Absolute Magnitude, Radio Luminosity, Stellar Mass And Specific Star Formation Rate

Some further analysis can be done by focusing on the relations between the absolute I-band magnitude and the redshift and between the specific star

formation rate and the stellar mass.

3.3.1 Absolute Magnitude Distribution

The first of these relations depicts the effect of redshift on the absolute magnitude of the observed galaxies. In fact, when dealing with an apparent magnitude limited survey, such as the one used for this work (see chapter 2), the number of galaxies of a given absolute magnitude changes with redshift, since absolute magnitude, redshift and apparent magnitude are correlated. If apparent magnitude is kept constant, absolute magnitude depends on distance. Therefore the most distant galaxies observed in an apparent magnitude limited survey (those at higher redshift), are also the most luminous and, increasing the redshift of observations, fainter galaxies are lost. Therefore at high redshifts the sample is biased towards higher luminosities and this bias is known as the *Malmquist Bias*.

For the present sample, absolute magnitudes are calculated using the template fitting method described in section 2.2.1.

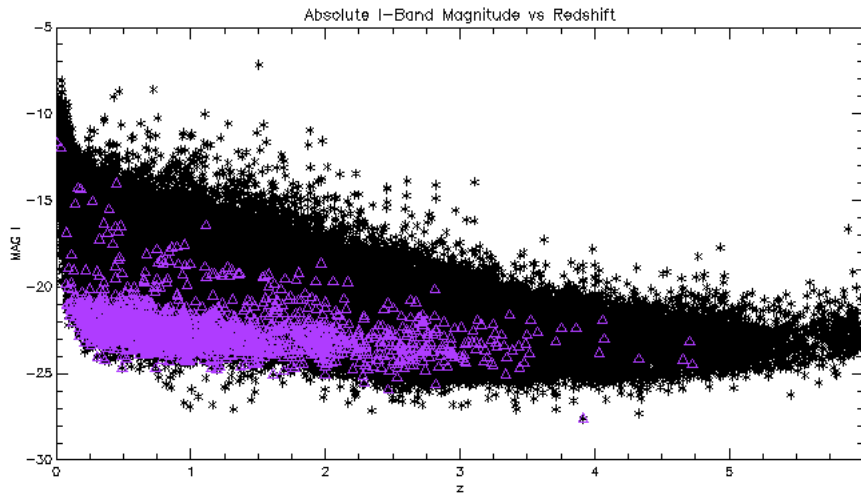


Figure 3.5: Absolute I-band Magnitude Vs. Redshift. The black stars represent the whole optical sample, the purple triangles represent the radio-optical sample. The cut to apparent I-band magnitude lower than 26.5 has been applied.

In figure 3.5 it can be seen how the Malmquist Bias affects the sample considered for this work. The black stars represent the whole optical sample, while the purple triangles represent the radio-optical sample. The cut to apparent I-band magnitude lower than 26.5 has been applied. It can be seen that the effect is great for the optical sample beyond redshift 2.7, while the sample can be considered complete down to an absolute magnitude of -20 in the whole redshift range. Objects fainter than that magnitude are lost at redshifts higher than 2.7. The completeness limit can be extended to an absolute magnitude of -17.5 when restricting the analysis to only those galaxies with a redshift lower than 3. For the radio-optical sample the completeness limit is more difficult to find, since the sample is less numerous, but it can conservatively be placed

3.3. ABSOLUTE MAGNITUDE, RADIO LUMINOSITY, STELLAR MASS AND SPECIFIC STAR FORMATION R.

around magnitude -20 out to $z = 3$. Points with absolute I-band magnitude lower than -25 are probably due to errors in the template fitting procedure used to calculate both redshift and absolute magnitude.

3.3.2 Radio Luminosity Distribution

It is interesting to derive a similar plot as the one showed in the previous section, using the radio luminosity at 1.4 GHz instead of the absolute I-band magnitude.

This quantity has been derived by converting the observed radio flux at 1.4 GHz to radio luminosity and applying the K-Correction to the formulas.

In figure 3.6, the correlation between radio luminosity and redshift is showed.

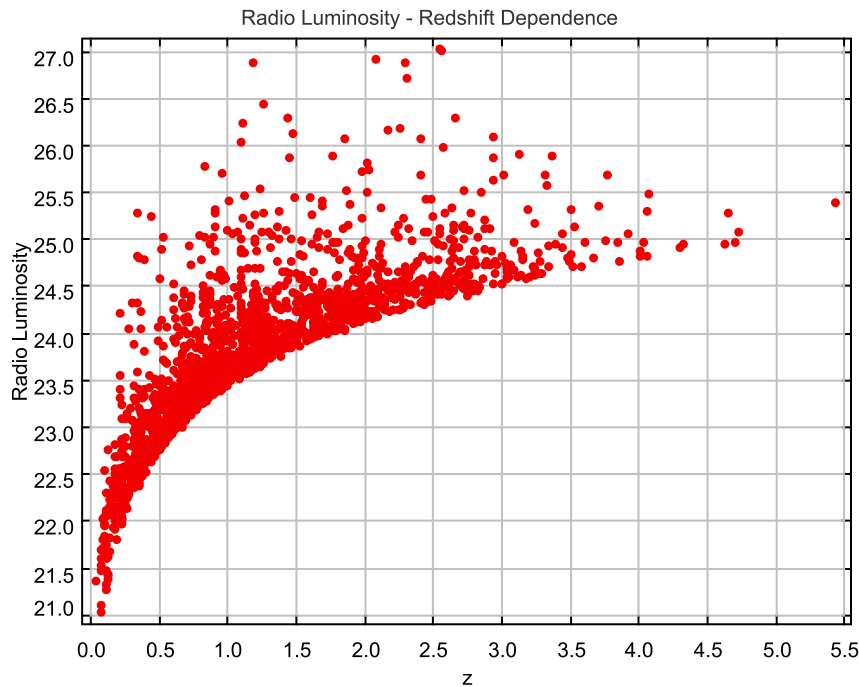


Figure 3.6: The correlation between radio luminosity at 1.4 GHz and redshift. The red dots represent the radio sample.

It can be seen again the tight correlation between intrinsic luminosity and redshift, referred to as the *Malmquist Bias*. In particular, in a flux limited sample, at higher redshifts only the most luminous objects will be observed, while the fainter ones will be lost.

For the present case, the sample can be considered complete down to a radio luminosity at 1.4 GHz of $\log(L_R) = 24.5$ out to redshift $z = 3$.

3.3.3 Specific Star Formation Rate And Stellar Mass

Another relation on which it is important to focus in order to better analyze the sample is the one between specific star formation rate (SSFR) and the stellar mass of the galaxy (M^*). This relation represents a way to visualize the evolution of a galaxy with time, since if a constant SSFR is assumed the galaxy will move on the plot from low to high M^* . When all the gas is consumed or SSFR is quenched, the galaxy will move at almost constant mass from high to low SSFR. Therefore the diagram can help segregate galaxies into early-type (with almost no SSFR, will be situated in the bottom right corner of the plot, at high M^* and low SSFR) and late-type (with high SSFR and usually less M^* than ellipticals).

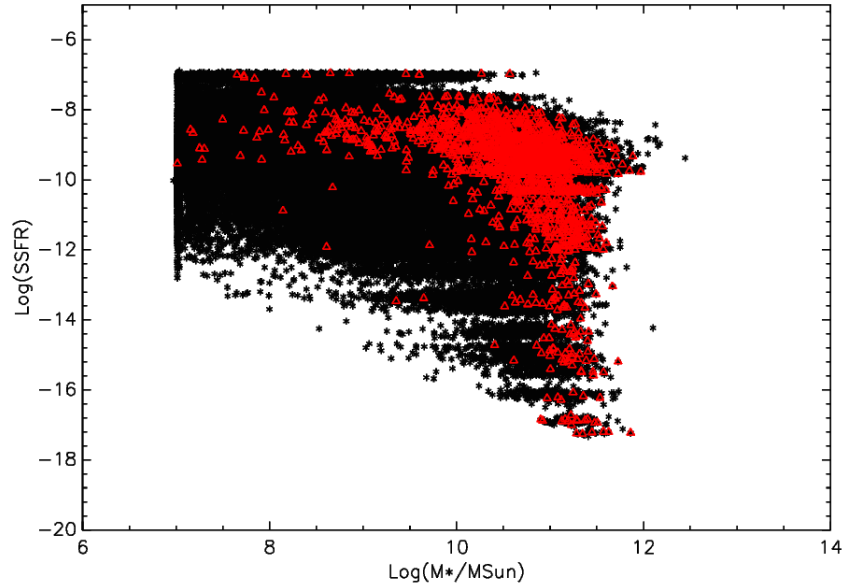


Figure 3.7: Specific Star Formation Rate Vs. Stellar Mass. The black stars represent the whole optical sample, the red triangles represent the radio-optical sample.

In figure 3.7 the relation between the SSFR and the stellar mass is derived for the optical sample (black stars) and for the radio-optical sample (red triangles). It is easily seen that the galaxies forming the radio-optical sample have a higher stellar mass than those forming the optical sample.

The specific star formation rate is defined as

$$\log\left(\frac{SSFR}{yr^{-1}}\right) = \log\left(\frac{SFR}{M_{\odot} yr^{-1}}\right) - \log\left(\frac{M^*}{M_{\odot}}\right) \quad (3.1)$$

where SFR is the star formation rate. The star formation rate and the stellar mass entering in the equation above are calculated through template fitting, as described in section 2.2.1.

The same plot is realized in figure 3.8 for the sole optical sample. The sample has been divided into three redshift bins in order to better evedentiate

3.3. ABSOLUTE MAGNITUDE, RADIO LUMINOSITY, STELLAR MASS AND SPECIFIC STAR FORMATION R.

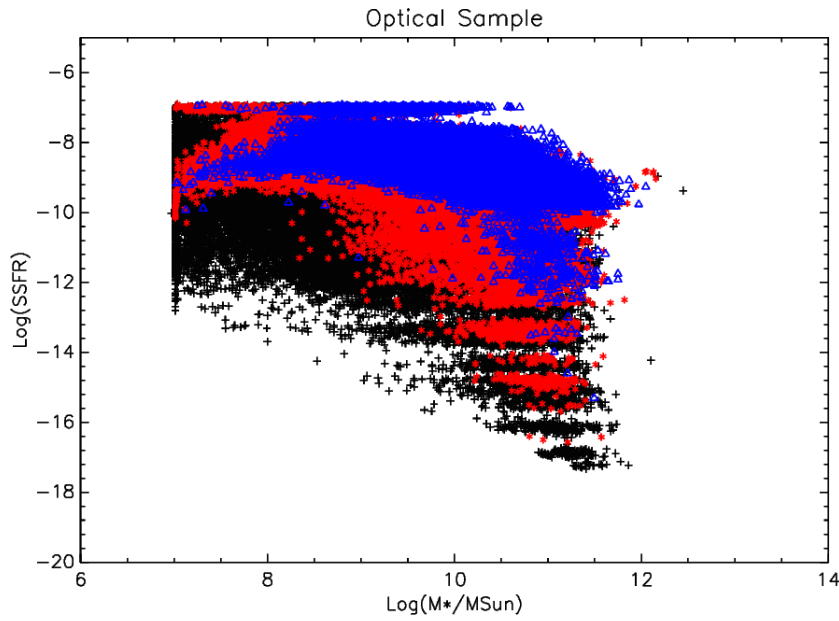


Figure 3.8: Specific Star Formation Rate Vs. Stellar Mass. The plot is derived for the optical sample in three redshift bins, as described in text. The black stars identify Bin 1, the red crosses Bin 2, the blue triangles Bin 3. The redshift bins are defined in the following way: Bin 1 refers to $z = 0 \div 1$, Bin 2 to $z = 1 \div 2$ and Bin 3 to $z = 2 \div 3$.

the evolution with time of the galaxy sample. The redshift bins are defined in the following way: Bin 1 refers to $z = 0 \div 1$, Bin 2 to $z = 1 \div 2$ and Bin 3 to $z = 2 \div 3$. The bins are referred to in the plot with black stars (Bin 1), red crosses (Bin 2) and blue triangles (Bin 3).

It is easily seen, with this distinction in redshift bins, the different evolutionary stage of the galaxies at different redshifts: moving from galaxies at lower redshift to those at higher redshift, the fraction of galaxies of high stellar mass reaching higher SSFR increases. In particular the galaxies are distributed in the following way: 57% of galaxies with redshift $0 < z < 1$ (Bin 1) have $\log(\frac{M^*}{M_\odot}) \geq 10$ and $\log(SSFR) \leq -10$, this fraction changes to 12% for Bin 2 and to 2% for Bin 3.

A similar plot is also realized for the radio-optical sample, with the same distinction of the galaxies in redshift bins and is shown in figure 3.9.

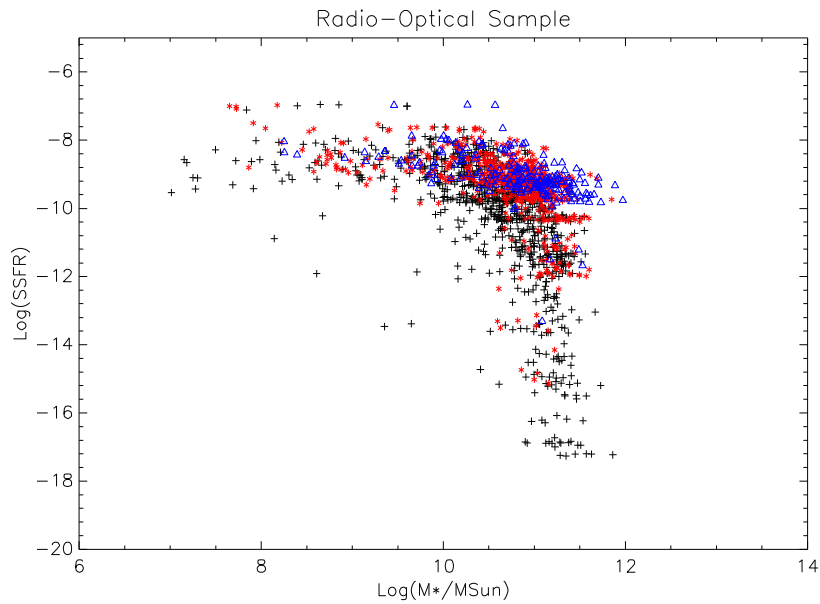


Figure 3.9: Specific Star Formation Rate Vs. Stellar Mass. The plot is derived for the radio-optical sample in three redshift bins, as described in text. The black stars identify Bin 1, the red crosses Bin 2, the blue triangles Bin 3. The redshift bins are defined in the following way: Bin 1 refers to $z = 0 \div 1$, Bin 2 to $z = 1 \div 2$ and Bin 3 to $z = 2 \div 3$.

In this plot the effect depicted above, of galaxies of high stellar mass reaching higher SSFR at high redshift is even more evident. A similar analysis as the one done for the optical sample yields the following fractions: 51% of galaxies in Bin 1 have $\log(\frac{M^*}{M_\odot}) \geq 10$ and $\log(SSFR) \leq -10$, the percent changes to 19% for galaxies in Bin 2 and to 3% for galaxies in Bin 3, therefore showing a faster evolution for radiogalaxies compared to normal ones.

3.3. ABSOLUTE MAGNITUDE, RADIO LUMINOSITY, STELLAR MASS AND SPECIFIC STAR FORMATION RATE

In all the plots above, the presence of points with very high SSFR (those with values of $\log(SSFR) \sim -7 \div -7.5$) are probably due to catastrophic errors in the template fitting procedure during the calculations of redshift, absolute magnitude, stellar mass and specific star formation rate.

These results are summarized in table 3.2. The errors on the fractions of galaxies are derived through error propagation from the counts of galaxies in each redshift bin satisfying the exposed stellar mass and specific star formation rate conditions.

Bin	Redshift Interval	Radio-Optical Sample Fraction Of Galaxies	Optical Sample Fraction Of Galaxies
Bin 1	$z = 0 \div 1$	$(51 \pm 3.3)\%$	$(57 \pm 0.7)\%$
Bin 2	$z = 1 \div 2$	$(19 \pm 2.1)\%$	$(12 \pm 0.2)\%$
Bin 3	$z = 2 \div 3$	$(3 \pm 1.4)\%$	$(2 \pm 0.08)\%$

Table 3.2: Fractions Of Galaxies With $\log(\frac{M^*}{M_\odot}) \geq 10$ And $\log(SSFR) \leq -10$

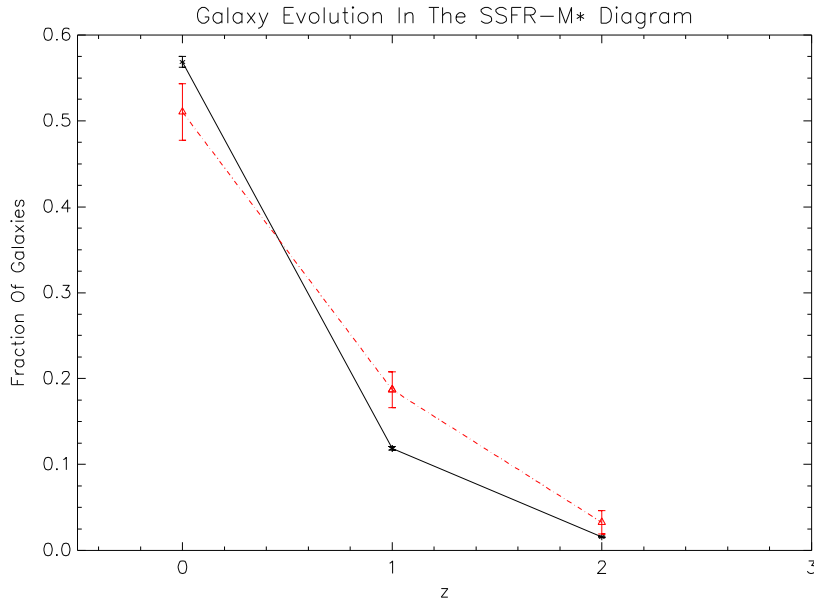


Figure 3.10: Evolution Of Galaxies In The $SSFR-M^*$ Plot. The solid black line represents the optical sample, while the red dash-dot one represents the radio-optical sample.

In figure 3.10 the result is shown in a more accessible way. The plot represents the change of the fraction of galaxies with $\log(\frac{M^*}{M_\odot}) \geq 10$ and $\log(SSFR) \leq -10$ as a function of redshift. The solid black line represents the optical sample, while the red dash-dot line represents the radio-optical sample. It can be

seen that at redshift higher than 1 the radio-optical sample undergoes a faster evolution, as the fraction of galaxies changes with a steeper slope.

3.4 Conclusions

In this chapter a preliminary analysis of the data has been made.

In first place the optical sample and the radio one have been matched, reducing the number of galaxies to 1806 that have radio and optical data, together with a measured photometric redshift, and which constitute the radio-optical sample.

The preliminary analysis of the sample has regarded the comparison between basic properties of the various samples. Total radio flux distributions (figure 3.1), redshift distributions (figure 3.3) and apparent I-band magnitude distributions (figure 3.2) have been analyzed. For the total radio flux distributions no differences have been found between the radio sample and the radio-optical sample. Different are instead the redshift distributions, which present some features which required a further analysis, such as the small peak at $z = 2$ in the redshift distribution of the radio-optical sample. Very different are also the apparent I-band magnitude distributions, with the optical sample reaching lower luminosities than the radio-optical sample. From these distributions, a completeness line at a magnitude of 26.5 has been assumed, and used to cut all the samples.

Moreover, some more complex analysis has been performed on the samples. The plot of figure 3.5 shows the correlation between absolute I-band magnitude and redshift. From this plot it is possible to place the completeness limit around an absolute magnitude of -20 . The following figures, instead, show the correlation between the stellar mass and the specific star formation rate. These plots help segregate the galaxies forming the various samples into early-type and late-type and, by making the same plots with the galaxies divided in various redshift bins, it is possible to appreciate the change in the various quantities associated with galaxy evolution. For the present samples, the general results are confirmed: radiogalaxies have a faster evolution than normal ones.

Chapter 4

The Study Of The Environment

THE most important part of the data analysis is the study of the environment of galaxies, based on the search in the data sample for overdensities of galaxies.

This chapter is structured as it follows: in section 4.1 the searching algorithm is described, in section 4.2 the so called “control sample ”is defined and the reason for its creation is explained. In section 4.3 the application of the searching algorithm to galaxies is discussed. In section 4.4 first improvements on the technique are described, in particular those regarding the dependence from redshift of the radius of the research. In section 4.5 an analysis of the significativity of the results is performed.

4.1 The Searching Algorithm

The search for groups of galaxies has been realized in several steps, each of which refines and improves the searching algorithm in order to account for several physical effects and to make both the sample of groups which is going to be created and the control sample the most possible homogeneous.

The searching algorithm operates in the following way: for every galaxy in the radio-optical sample, galaxies in the optical sample, which lay in a cylinder of defined radius and height centered around the radiogalaxy, are identified. The dimensions of this cylinder are comparable with the physical dimensions of a cluster of galaxies.

Since every galaxy is completely determined by a set of three coordinates (right ascension, declination and redshift) the search for groups is made by physically counting all the galaxies from the optical sample which have right ascension, declination and redshift within a defined distance from the coordinates of the radiogalaxy selected. The output of this search is a list of groups for each of which the number of elements composing the group and the right ascension, declination and redshift of the central radiogalaxy are given.

4.2 The Control Sample

In order to check the consistency of these results and to understand if these groups are real or just created by the extracion of selections from a greater sample, a control sample has been created. This sample (hereafter “control sample”) has been created in the following way: for every galaxy in the radio-optical sample, redshift and absolute magnitude are maintained, while right ascension and declination are substituted by values extracted randomly from the whole optical sample. The search for groups is run on it with the same algorithm used for the radio-optical sample. For every group the number of elements in the group as well as the coordinates of the control radiogalaxy in its center are given, as for the compilation of groups around the true sample of radiogalaxies.

The distributions of the number of groups of a given number of elements for both the radio-optical sample and for the control sample are confronted in the following through histograms, as explained the relative sections.

4.3 Fixed Distance

The first attempt to search for groups around the galaxies of the radio-optical sample has been carried out using coordinates at a fixed distance.

It has been chosen to search for groups in a volume of $1Mpc^3$ around every galaxy of the radio-optical sample.

The major issue in this setup of the problem is to find the angular dimension in arc seconds corresponding to 1 Mpc at a given redshift. This has been accomplished supposing, in first approximation, that all the galaxies are at the same redshift of $z = 1.5$. Using Ned Wright’s Javascript Cosmology Calculator¹ (Wright, 2006) it has been calculated that at $z = 1.5$ holds the equivalence $1'' = 8.539$ kpc. In order to derive this correspondence the Calculator set up has been changed to “Universe Type” = FLAT while for the cosmological parameters those in table 4.1, taken from Coles & Lucchin (2002), have been used.

Cosmological Parameter	Value
H_0	$71 \frac{\text{Km}}{\text{s} \times \text{Mpc}}$
Ω_{m0}	0.27
Ω_{r0}	$2.3 \times 10^{-5} h^{-2}$
$\Omega_{\Lambda 0}$	0.73
Ω_{tot}	1

Table 4.1: Cosmological Set Up

With the scale depicted above, it is calculated that $1 \text{ Mpc} = 1.95'$. The procedure is the following: for every galaxy in the radio-optical sample of given coordinates RA_r , Dec_r and z_r , galaxies from the optical sample are selected whose coordinates RA, Dec and z satisfy the conditions $RA_r - \Delta RA < RA < RA_r + \Delta RA$, $Dec_r - \Delta Dec < Dec < Dec_r + \Delta Dec$ and $z_r - \Delta z < z < z_r + \Delta z$ with $\Delta RA = \Delta Dec = 1.95'$ and $\Delta z = 0.1$. This value has been chosen for

¹<http://www.astro.ucla.edu/~wright/CosmoCalc.html>

it constitutes a first approximation of the true error value on the photometric redshift, corresponding to $\sigma_{\frac{\Delta z}{1+z_p}} = 0.06$. With this value of Δz , the search on the sample for groups is realized in a sphere of radius of 1 Mpc around every galaxy of the radio-optical sample.

The output of such a selection is shown in figure 4.1.

In the top panel of this figure the group richness distribution is shown, as the number of groups of a given richness as a function of the number of elements of each group. The two different histograms refer to different samples, namely the black solid line to the radio-optical sample and the red dash-dot line to the control sample. The two histograms are quite similar, both having the majority of groups composed of about 150 elements. They both also show a long tail, composed of groups made of a number of elements which can reach almost 700 units. Nevertheless, it has to be noticed that the distribution referring to the radio-optical sample is slightly shifted to higher group richnesses compared to the one referring to the control sample.

A χ^2 test performed on the distributions is showed in the second panel of the same figure, the algorithm of the test has been implemented following Press et al. (2007). In particular the formula used is

$$\chi^2 = \sum_{i=1}^{N_{bin}} \frac{(R_i - S_i)^2}{R_i + S_i} \quad (4.1)$$

where R_i and S_i are the number of counts in bin i for the two distributions that are tested and N_{bin} is the total number of bins. In particular, to derive the reduced χ^2 distribution showed in the second panel of figure 4.1, the formula implemented is

$$\chi_i = \xi_i \times \frac{R_i - S_i}{\sqrt{R_i + S_i} \times \nu} \quad (4.2)$$

where ν is the number of degrees of freedom and the function ξ_i is defined as

$$\xi_i = \begin{cases} -1 & \text{if } (R_i - S_i) < 0 \\ 0 & \text{if } (R_i - S_i) = 0 \\ 1 & \text{if } (R_i - S_i) > 0 \end{cases} \quad (4.3)$$

Therefore, the equation for χ^2 may be rewritten as

$$\chi^2 = \sum_{i=1}^{N_{bin}} \chi_i^2 \quad (4.4)$$

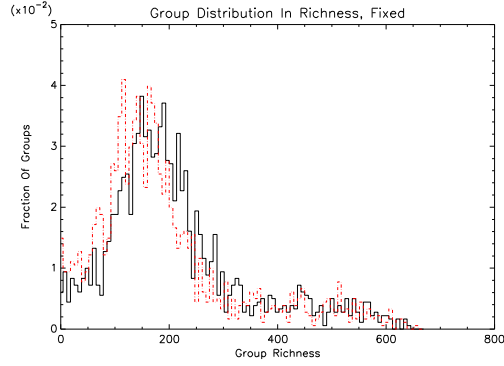
This implies that if the number of counts is higher in the control sample (*i.e.* if there are less groups around radiogalaxies at a given richness) it will be $\chi_i < 0$, otherwise, if there are more groups around radiogalaxies at a given richness, compared to the control sample, it will be $\chi_i > 0$.

The probability p is given by

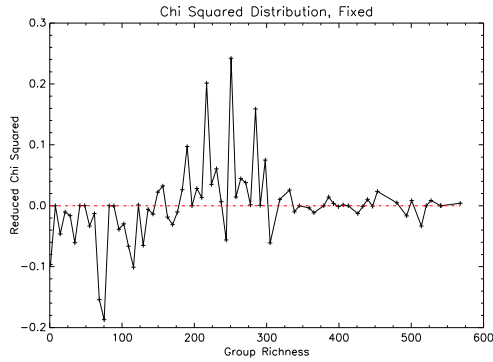
$$p = 1 - \gamma\left(\frac{\nu}{2}; \frac{\chi^2}{2}\right) \quad (4.5)$$

where ν is the number of degrees of freedom and γ is the Incomplete Euler Gamma Function, defined as

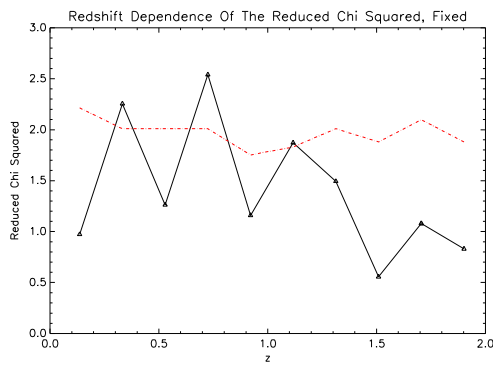
$$\gamma(a, x) = \frac{\int_0^x e^{-t} t^{a-1} dt}{\int_0^\infty e^{-t} t^{a-1} dt} \quad (4.6)$$



(a) *Group Richness Distribution.* The black solid line refers to the radio-optical sample, while the red dash-dot line to the control sample. The whole richness range has been divided in 100 bins.



(b) χ^2 *Distribution.* The χ^2 test has been applied to the two distributions above. The test results in $\chi^2 = 169.5$ and $p = 3.1 \times 10^{-10}$. A KS test results in $p = 9.64 \times 10^{-15}$ of the two distributions coming from the same parent population.



(c) *Redshift Dependence Of The Reduced χ^2 .* The red dash-dot line represents the tabulated χ^2 value for a significativity value of 0.05.

Figure 4.1: Fixed Coordinates

For the present work, the number of degrees of freedom has been put equal to the number of bins containing at least 5 elements minus one when the two distributions have the same number of total elements and to the number of bins with at least 5 elements when the total number of elements in the two distributions is different. A table of the values of the χ^2 distribution for various numbers of degrees of freedom may be found in the Appendix.

The reduced χ^2 distribution is quite irregular, with a few pronounced spikes between 200 and 300 elements and a deep fall around 75 elements. The value of χ^2 is 169.5, which is above the value listed in the tables for the number of degrees of freedom of this test for every significance level (the number of degrees of freedom is 70). The probability of the two distributions being drawn from the same population is 3.1×10^{-10} . Therefore it is possible to exclude the fact that the groups found by the algorithm are due to the simple extraction of a subsample from a much wider compilation of data, confirming the presence of a difference between the environment around radiogalaxies and around normal galaxies.

Moreover, a Kolmogorov-Smirnov test has been performed on the distributions, using the apposite supplied IDL routine.

The Kolmogorov-Smirnov test is a statistical tool which allows to determine the probability of two distributions of coming from the same parent population. This probability is determined by calculating the maximum difference between the cumulative distribution functions of the two datasets. Following Press et al. (2007), the Kolmogorov-Smirnov statistic is

$$D = \max_{-\infty < x < +\infty} (|S_{N_1}(x) - S_{N_2}(x)|) \quad (4.7)$$

where $S_{N_1}(x)$ and $S_{N_2}(x)$ are the cumulative distribution functions.

This statistic is very useful, since it works on unbinned data and it is invariant under the reparametrization of x . Therefore it is quite straightforward to apply to the datasets and gives reliable information on the probability of the two distributions being different.

The probability is defined by

$$p = Q \times \left(\left[\sqrt{N_e} + 0.12 + \frac{0.11}{\sqrt{N_e}} \right] \times D \right) \quad (4.8)$$

where D is the Kolmogorov-Smirnov statistic, defined above, N_e is the effective number of data points defined as

$$N_e = \frac{N_1 N_2}{N_1 + N_2} \quad (4.9)$$

and Q is the Kolmogorov-Smirnov Distribution, defined as

$$Q(z) = 2 \sum_{j=1}^{\infty} (-1)^{j-1} e^{-2j^2 z^2} \quad (4.10)$$

N_1 and N_2 are the number of points in each dataset.

For the present case the result of the Kolmogorov-Smirnov test is a probability $p = 9.64 \times 10^{-15}$ of the two distributions coming from the same parent population.

A further analysis has been performed on the data, in order to investigate the presence of redshift effects in the group distributions. Both the group richness

distributions have been segregated in a number of redshift bins from 2 to 10 in the range $0 < z < 2$ (depending on the total number of elements of the various samples, varying with the cuts performed as described in the following sections). In each redshift bin the group richness distributions for both the radio-optical and the control samples have been derived, binning the samples in a number of bins ranging from 5 to 15 according to the number of counts (here too, depending on the total number of elements of the various samples, varying with cuts performed as described in the following sections). The χ^2 test has then been performed on the distributions derived in each redshift bin.

For the present case the result is showed in the third panel of figure 4.1. The number of redshift bins is 10. The dependence of the reduced χ^2 from redshift is showed together with a red dash-dot line representing the tabulated value of the reduced χ^2 for a significance level of 0.05. The redshift dependence is not very strong since the curve remains more or less constant in the redshift interval. It can be seen that in a few redshift bins the reduced χ^2 value is above the tabulated one.

4.3.1 Fixed Distance, Apparent Magnitude Cut

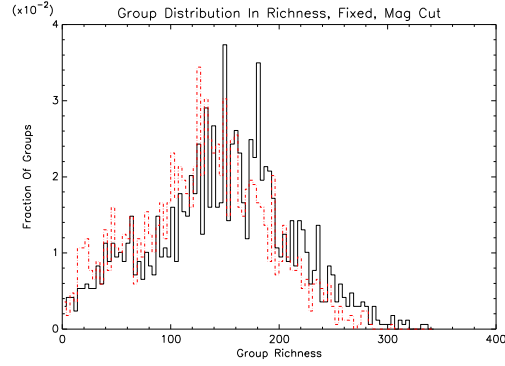
As said in chapter 3, the sample can be considered complete only up to an apparent I-band magnitude of 26.5. Therefore a cut to that apparent magnitude has been applied to the sample, excluding fainter objects and the group search algorithm has been run again.

From the total optical and radio-optical sample only the galaxies with apparent I-band magnitude lower than 26.5 have been selected. This reduces the total samples to 823939 and 1687 galaxies. The output of the group search is shown in the upper panel of figure 4.2. It can be seen that the shape of the distributions is slightly different from before. The two distributions are wider, their peaks are less pronounced, while still reached for groups of about 150 elements. Moreover, the tail extends less, reaching at maximum groups with less than 400 units.

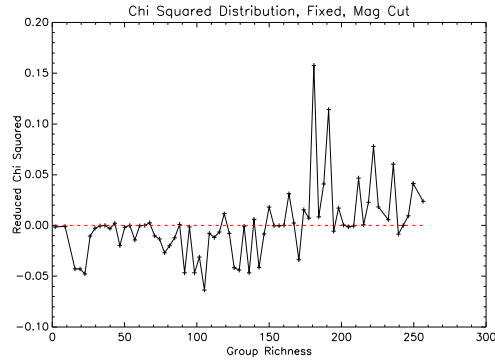
A χ^2 test performed on the distributions is showed in the second panel of the same figure. The distribution shows a peak around 200 elements, although it is quite irregular. The value of χ^2 is 103.03, with a probability of the two distributions of being drawn from the same parent population of 0.006. This value of χ^2 is above the tabulated values for every significance value above 0.005. It is therefore possible to exclude that the two distributions come from the same parent population in a fairly consistent way. The χ^2 test has been applied considering only the 70 bins which have at least 5 elements.

As in the previous case a KS test has been performed on the distributions, resulting in a probability $p = 1.10 \times 10^{-13}$ of the two distributions coming from the same parent population.

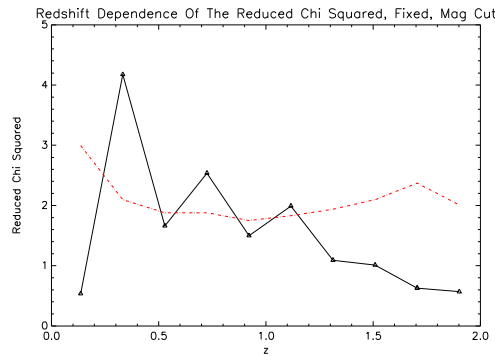
As before, the distributions have been analyzed with redshift, dividing them in 10 redshift bins and executing a χ^2 test in each bin. The result is shown in the third panel of the same figure. The χ^2 does not depend strongly on redshift, not varying much in the redshift range. A few points are however over the tabulated value.



(a) *Group Richness Distribution.* The solid black line refers to the radio-optical sample, while the red dash-dot line to the control sample. The whole richness range has been divided in 100 bins. The apparent magnitude cut $magI < 26.5$ has been applied.



(b) χ^2 *Distribution.* The χ^2 test has been applied to the two distributions above and results in $\chi^2 = 103.03$ and probability $p = 0.006$. A KS test results in $p = 1.10 \times 10^{-13}$ of the two distributions coming from the same parent population.



(c) *Redshift Dependence Of The Reduced χ^2 .* The red dash-dot line represents the tabulated χ^2 value for a significance value of 0.05.

Figure 4.2: Fixed Coordinates, I-Band Apparent Magnitude Cut

4.3.2 Stellar Mass And Specific Star Formation Rate Selections

Further cuts have been introduced on the galaxies considered, in order to examine the effects of differences in the samples on the search for galaxy groups. In particular, the radio-optical sample and the control sample have been furtherly reduced by adding to the cut to apparent I-band magnitude at 26.5 a further distinction based on the logarithm of stellar mass and on the logarithm of specific star formation rate (calculated and discussed in section 2.2.1).

From both the radio-optical and the control samples only galaxies with $\log(\frac{M^*}{M_\odot}) > 10$ have been selected. A further distinction has been made, by selecting galaxies having $\log(SSFR)$ either greater than or lower than -11. Given these cuts, the number of galaxies in each sample becomes: 276 galaxies with $\log(\frac{M^*}{M_\odot}) > 10$ and $\log(SSFR) < -11$ for both the radio-optical sample and the control sample and 1172 galaxies with $\log(\frac{M^*}{M_\odot}) > 10$ and $\log(SSFR) > -11$ for both the radio-optical sample and the control sample.

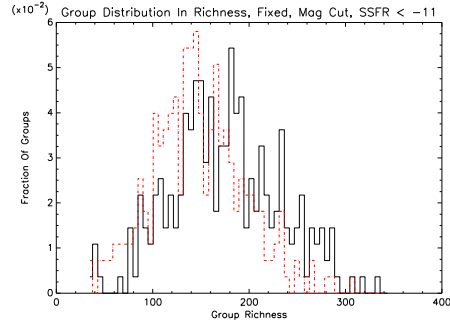
The group search algorithm has been run separately on the four distinct compilations of data. In figure 4.3 it is shown the result of the search for groups on the radio-optical and control sample with I-band apparent magnitude lower than 26.5, $\log(\frac{M^*}{M_\odot}) > 10$ and $\log(SSFR) < -11$. In the upper panel the two group richness distributions are shown (group search on the radio-optical sample, solid black line, and on the control sample, red dash-dot line). The two distributions are similar, they both have a peak for groups composed of about 160 elements, while maximum values are lower than 350 units. Again, however, the group richness distribution of the radio-optical sample is slightly shifted towards higher richness values, compared to the control sample one.

A χ^2 test applied on the two distributions results in $\chi^2 = 18.73$, a value below the tabulated values even for a significance level of 0.10, with a probability of the two distributions (radio-optical and control sample) of being drawn from the same parent population of 0.54. It is therefore really hard to state the presence of a difference in the properties of groups around radio galaxies from those found around normal galaxies. The χ^2 distribution is shown in the second panel of figure 4.3. Again it is rather irregular, with its most pronounced peak around 190 units and a deep valley around 165 elements. The χ^2 test has been applied using only the 69 bins which have at least 5 elements.

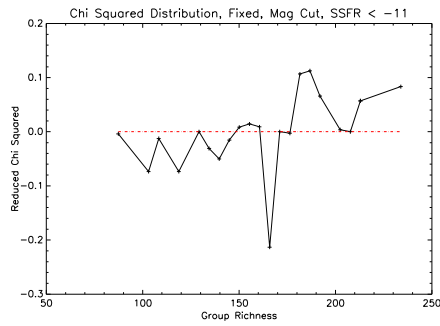
Nevertheless, a KS test results in $p = 4.4 \times 10^{-8}$ of the two distributions coming from the same parent population, a very low value.

The sample has been furtherly analyzed by subdividing both distributions in two redshift bins and applying the χ^2 test in each of them. The dependence of the reduced χ^2 from redshift is explicit in the third panel of the same figure. The dependence is quite strong as the reduced χ^2 changes a lot in the redshift range, going from above to below the tabulated values for the 0.05 significance level (red dash-dot line).

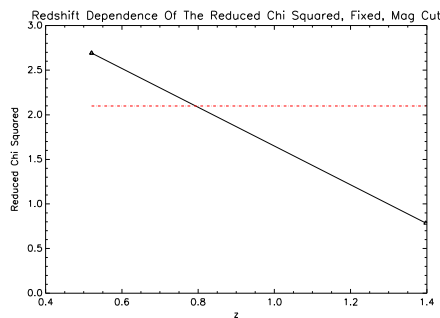
The situation is different for the complementary sample. In figure 4.4 it is shown the result of the search for groups on the radio-optical and control samples with I-band apparent magnitude lower than 26.5, $\log(\frac{M^*}{M_\odot}) > 10$ and $\log(SSFR) > -11$. In the upper panel the group richness distributions are shown, the solid black line refers to the radio-optical sample, the red dash-dot line to the control sample. The distributions are better defined, since the



(a) *Group Richness Distribution.* The solid black line refers to the radio-optical sample, while the red dash-dot line to the control sample. The whole richness range has been divided in 60 bins. The apparent magnitude cut $magI < 26.5$ has been applied, together with the cuts $\log(\frac{M^*}{M_\odot}) > 10$ and $\log(SSFR) < -11$.



(b) χ^2 *Distribution.* The χ^2 test has been applied to the group distributions shown in the panel above and results in $\chi^2 = 18.73$ with a probability p of 0.56. A KS test results in $p = 4.4 \times 10^{-8}$ of the two distributions coming from the same parent population.



(c) *Redshift Dependence Of The Reduced χ^2 .* The red dash-dot line represents the tabulated χ^2 value for a significativity value of 0.05.

Figure 4.3: Fixed Coordinates, I-Band Apparent Magnitude Cut, Stellar Mass And SSFR Cut

number of counts is higher for this case than for the previous one. The peak is reached again for groups of about 160 elements, but there is also a tail extending to groups with fewer elements, absent for the sample with logarithm of $\log(SSFR) < -11$.

A χ^2 test applied on the two distributions results in $\chi^2 = 66.47$, a value which is never above the tabulated values for every significance level, with a probability of the two distributions (radio-optical and control sample) of being drawn from the same parent population of 0.56. It is again really hard to state the presence of differences in the environment of radiogalaxies, compared to normal ones, on the basis of this test. The χ^2 distribution is showed in the second panel of figure 4.4. It is quite irregular, with a few peaks above 150 elements and a fall around 95 elements. The χ^2 test has been applied using only the 20 bins which have at least 5 elements.

Nevertheless, a KS test results in a promising value $p = 6.6 \times 10^{-6}$ of the two distributions coming from the same parent population, again quite low.

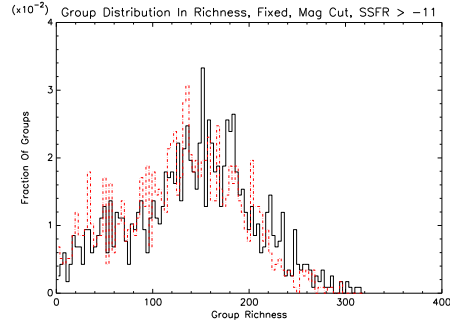
The distributions showed in figure 4.4 have been furtherly analyzed, in order to check whether any redshift effects are present. The groups plotted in figure 4.4 have been segregated in ten redshift bins, from $z = 0$ to $z = 2$ and the reduced χ^2 has been calculated in each redshift bin. The third panel of the same figure shows the dependence from redshift of the reduced χ^2 . It is seen that the value of the reduced χ^2 is fairly irregular, changing a lot over the redshift range and crossing a few times the tabulated value for a significance level of 0.05 (red dash-dot line).

4.3.3 Stellar Mass And Specific Star Formation Rate Selections Applied Also To The Optical Sample

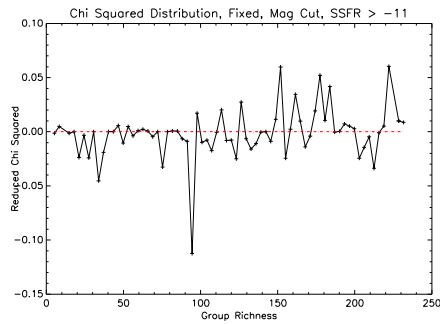
The same cuts in SSFR and stellar mass applied to the radio-optical and control samples have been applied also to the optical sample and the group search algorithm has been run again.

This implies a further step in the study of the environment. Previously, no limits (excluding the cut in apparent magnitude due to the completeness limit of the sample) had been applied to the optical sample, *i.e.* to those galaxies which compose the groups. Now, cuts have been applied not only to the radiogalaxies around which groups are searched, but also to the galaxies which compose the groups themselves (optical sample). Therefore, galaxies composing the groups are required to have the same specific star formation and stellar mass properties as the radiogalaxies assumed to be at the center of each group.

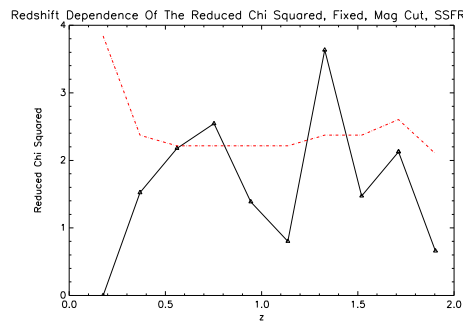
In figure 4.5 the results of the search for groups around radiogalaxies with $\log(\frac{M^*}{M_\odot}) > 10$ and $\log(SSFR) < -11$ made on the optical sample with the same cuts is shown. In the upper panel the group richness distributions are showed (the solid black line refers to the radio-optical sample, the red dash-dot line to the control sample). The richness of the groups is lower than in the previous cases, since the samples themselves are less numerous. The distributions both peak at really low values and then decrease rapidly. A χ^2 test has been run on the distributions and it results in a value of 33.58 well above the tabulated values for every significance level for a number of degrees of freedom of 7, corresponding to the number of bins with more than 5 elements. The probability is 2.1×10^{-5} that the two distributions come from the same parent population. Therefore



(a) *Group Richness Distribution.* The solid black line refers to the radio-optical sample, while the red dash-dot line to the control sample. The whole richness range has been divided in 100 bins. The apparent magnitude cut $magI < 26.5$ has been applied, together with the cuts $\log(\frac{M^*}{M_\odot}) > 10$ and $\log(SSFR) > -11$.



(b) χ^2 *Distribution.* The χ^2 test has been applied to the group distributions shown in the panel above. The result is $\chi^2 = 66.47$ and $p = 0.56$. A KS test results in $p = 6.6 \times 10^{-6}$ of the two distributions coming from the same parent population.



(c) *Redshift Dependence Of The Reduced χ^2 .* The red dash-dot line represents the tabulated χ^2 value for a significativity value of 0.05.

Figure 4.4: Fixed Coordinates, I-Band Apparent Magnitude Cut, Stellar Mass And SSFR Cut

the two distributions are different. The χ^2 distribution is showed in the second panel of the same figure. It is essentially composed of a smooth curve covering the range between 2 and 10 elements. In the third panel of the same figure the same analysis with redshift of the χ^2 value as before is showed. The distributions have been divided in 2 redshift bins and the change of the reduced χ^2 value is great in the redshift range.

A KS test has been performed on the distributions and results in $p = 3.45 \times 10^{-16}$ of the two distributions coming from the same parent population.

In figure 4.6 the result of the study of the environment around galaxies from the complementary sample (the one with $\log(\frac{M^*}{M_\odot}) > 10$ and $\log(SSFR) > -11$, made on the optical sample with the same cuts) is showed. In the upper panel the group richness distributions are showed, solid black line for the radio-optical sample and red dash-dot line for the control sample. The distributions are quite wide, they peak for groups with a number of elements around 10 and they have a tail extending almost to groups with 40 elements. In the lower panel the χ^2 distribution resulting from the χ^2 test applied to the histograms above is showed. It consists of a few peaks covering the range from 10 to 40 units and a couple of valleys in the range from 0 to 5 elements. The result of the χ^2 test is $\chi^2 = 95.34$ a value highly above the tabulated values for every significance level showing that the two distributions are different. The probability p that the two distributions come from the same parent population is $p = 3.8 \times 10^{-10}$. The χ^2 test has been applied using only the 25 bins which have at least 5 elements.

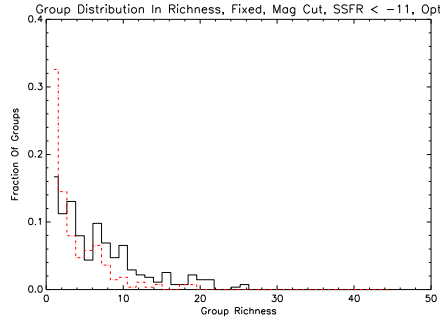
A KS test results in $p = 1.82 \times 10^{-16}$ of the two distributions coming from the same parent population.

The third panel of figure 4.6 shows the dependence of the reduced χ^2 on redshift, result of an analysis similar to the one done above. The plot shows a great change in the reduced χ^2 , demonstrating a dependence on redshift. The values in every redshift bin are always above the tabulated ones for a significance level of 0.05 (red dash-dot line).

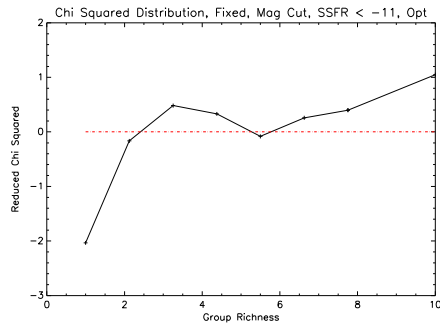
In table 4.2 a summary of the results obtained for the search for groups with fixed distance is given. With N_{RO} and N_C the number of galaxies in the Radio-Optical sample and in the Control sample are indicated. In the last column the probability p_{KS} from the Kolmogorov-Smirnov test of the two distributions coming from the same parent population is indicated.

Type Of Sample	N_{RO}	N_C	p_{KS}
Total Sample	1806	1806	9.64×10^{-15}
$magI < 26.5$	1687	1687	1.10×10^{-13}
$\log(\frac{M^*}{M_\odot}) > 10$ And $\log(SSFR) < -11$	276	276	4.4×10^{-8}
$\log(\frac{M^*}{M_\odot}) > 10$ And $\log(SSFR) > -11$	1172	1172	6.6×10^{-6}
$\log(\frac{M^*}{M_\odot}) > 10$ And $\log(SSFR) < -11$, Also To Optical Sample	276	276	3.45×10^{-16}
$\log(\frac{M^*}{M_\odot}) > 10$ And $\log(SSFR) > -11$, Also To Optical Sample	1172	1172	1.82×10^{-16}

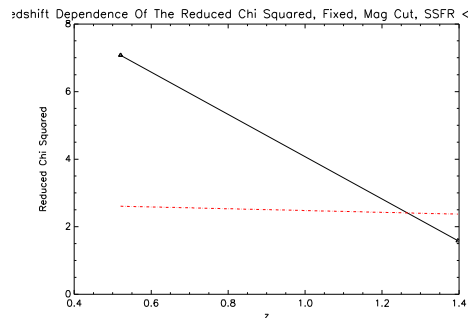
Table 4.2: The Study Of The Environment, Fixed Distance



(a) *Group Richness Distribution.* The solid black line refers to the radio-optical sample, while the red dash-dot line to the control sample. The whole richness range has been divided in 40 bins. The apparent magnitude cut $magI < 26.5$ has been applied, together with the cuts $\log(\frac{M^*}{M_{\odot}}) > 10$ and $\log(SSFR) < -11$ to the radio-optical sample, the control sample and the optical sample.

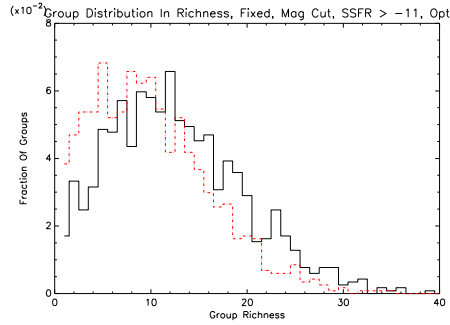


(b) χ^2 *Distribution.* The χ^2 test has been applied to the group richness distributions shown in the panel above, the results are $\chi^2 = 33.58$ and $p = 2.1 \times 10^{-5}$. A KS test results in $p = 3.45 \times 10^{-16}$ of the two distributions coming from the same parent population.

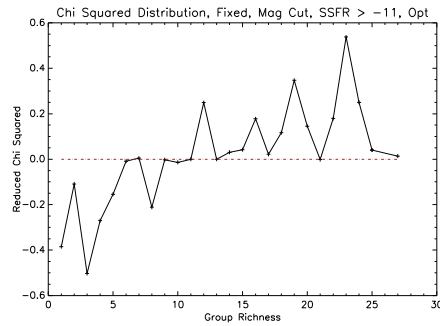


(c) *Redshift Dependence Of The Reduced χ^2 .* The red dash-dot line represents the tabulated χ^2 value for a significance value of 0.05 and a number of degrees of freedom of 4.

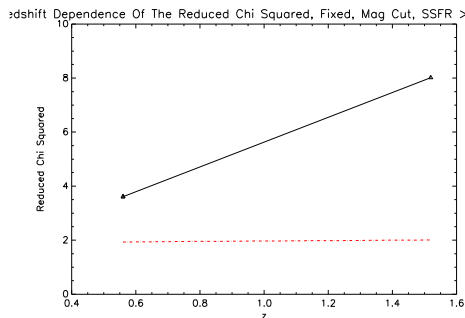
Figure 4.5: Fixed Coordinates, I-Band Apparent Magnitude Cut, Stellar Mass And SSFR Cut, Applied Also To The Optical Sample.



(a) *Group Richness Distribution.* The solid black line refers to the radio-optical sample, while the red dash-dot line to the control sample. The whole richness range has been divided in 40 bins. The apparent magnitude cut $magI < 26.5$ has been applied, together with the cuts $\log(\frac{M^*}{M_\odot}) > 10$ and $\log(SSFR) > -11$ to the radio-optical sample, the control sample and the optical sample.



(b) χ^2 *Distribution.* The χ^2 test has been applied to the group distributions shown in the panel above and it returns a value of 95.34 and $p = 3.8 \times 10^{-10}$. A KS test results in $p = 1.82 \times 10^{-16}$ of the two distributions coming from the same parent population.



(c) *Redshift Dependence Of The Reduced χ^2 .* The red dash-dot line represents the tabulated χ^2 value for a significativity value of 0.05.

Figure 4.6: Fixed Coordinates, I-Band Apparent Magnitude Cut, Stellar Mass And SSFR Cut, Applied Also To The Optical Sample.

4.4 Redshift Dependent Radius

The first step that can be taken to improve the search for groups is to include in the searching algorithm the dependence of the angular dimension from the redshift.

In the previous section it has been stated that at a redshift of $z = 1.5$, 1 Mpc corresponds to $1.95'$. This represents quite a rough assumption, since actually the situation is quite different. In fact, at redshift $z = 1$, 1 Mpc corresponds to $2.07'$, while at $z = 2$, 1 Mpc corresponds to $1.97'$. Assuming a constant value of $z = 1.5$ represents, therefore, a bias, since the redshift distributions of the two samples cannot be approximated by a constant value. This can lead to unphysical results. In order to resolve the problem it is necessary to implement an angular dimension corresponding to the scale length on which groups are searched for as a function of the redshift of the galaxy of the radio-optical sample around which the group is searched.

This is achieved by considering where the dependence from redshift is explicated in the coordinate shifts expressed in section 4.3. In particular, it is true the following expression (taken from the algorithm used by Ned Wright's Javascript Cosmology Calculator², see also Wright (2006)):

$$\Delta RA = \Delta Dec \propto \frac{\theta}{d} \propto D_A(z) \quad (4.11)$$

where ΔRA and ΔDec are the coordinate shifts, d is the source linear dimension, θ is its angular dimension and $D_A(z)$ is the angular diameter distance, with its redshift dependence explicated.

It is possible to derive an analytical form for $D_A(z)$:

$$D_A(z) = \frac{cZ(z)}{H_0} \frac{J([1 - \Omega_{tot}]Z(z)^2)}{1 + z} \quad (4.12)$$

where H_0 is the Hubble Constant, c is the speed of light, z is the redshift. Z and J are functions whose analytical form can be derived:

$$J(x) = \begin{cases} \frac{\sin(\sqrt{-x})}{\sqrt{-x}} & \text{if } x < 0, \\ \frac{\sinh(\sqrt{x})}{\sqrt{x}} & \text{if } x > 0, \\ 1 + \frac{x}{6} + \frac{x^2}{120} + \dots + \frac{x^n}{(2n+1)!} + \dots & \text{if } x \approx 0. \end{cases} \quad (4.13)$$

$$Z(z) = \int_{\frac{1}{1+z}}^1 \frac{da}{a\sqrt{X}} \quad (4.14)$$

where

$$X(a) = \frac{\Omega_{m0}}{a} + \frac{\Omega_{r0}}{a^2} + \Omega_{\Lambda 0} a^2 + (1 - \Omega_{tot}) \quad (4.15)$$

In these equations a is the scale parameter, Ω_{m0} is the matter density parameter at t_0 , where t_0 is now, Ω_{r0} is the radiation density parameter at t_0 , $\Omega_{\Lambda 0}$ is the vacuum density parameter at t_0 and Ω_{tot} is the total density parameter.

In this data analysis all of the formulas above have been implemented as described in the text and the integral has been calculated with the trapezoid method (for a theoretical description see Press et al. (2007)).

²http://www.astro.ucla.edu/~wright/Distances_details.gif

The parameters inserted in the formulas are those found in table 4.1, all of the parameters have been chosen so to have a flat universe. These values have been taken from Coles & Lucchin (2002).

The output of this improvement in the searching algorithm is showed in figure 4.7.

Again the solid black line refers to the radio-optical sample, while the red dash-dot line to the control sample. The plot has been realized with ΔRA and ΔDec calculated following the formulas above and with $\Delta z = 0.06 \times (1 + z) \times 3$ where z is the redshift of the radiogalaxy around which the search is conducted, following the prescription of Ilbert et al. (2009). Both distributions have a peak for groups with less than a thousand elements, with a tail reaching almost groups with 2500 elements.

The χ^2 test performed on the two distributions gives a result of 110.53, a value above the tabulated values for every significativity level for a number of degrees of freedom of 49, corresponding to the number of bins with at least 5 elements. The probability p of the two distributions coming from the same parent population is 1.2×10^{-6} . The χ^2 distribution (second panel of figure 4.7) is quite irregular, with a deep valley values around 500 elements.

As in the previous situations a Kolmogorov-Smirnov test has been applied to the data and it results in a probability 3.21×10^{-11} of the two distributions being drawn from the same parent population.

The same redshift analysis as before has been done on the distributions, dividing them in ten redshift bins and applying the χ^2 test in each bin. The dependence of the reduced χ^2 from redshift is explicited in the third panel of figure 4.7. The curve is quite constant in the whole redshift range, with only one point far above the tabulated value of the χ^2 distribution for a significance level of 0.05 (red dash-dot line).

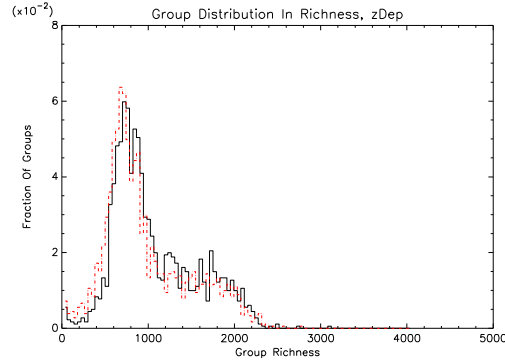
4.4.1 Apparent Magnitude Cut

The sample has been further restrained following the same procedure as in section 4.3.1. Only those galaxies in both the radio-optical sample and the control sample having apparent I-band magnitude lower than 26.5 have been selected. The group search algorithm has been run again on both the samples and the output is showe in figure 4.8.

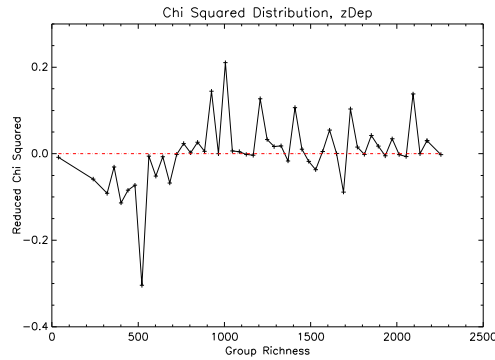
In the upper panel the richness distributions of groups are showed. The solid black line refers to the radio-optical sample and the red dash-dot line to the control sample. The two distributions are again different, but they both peak for groups of slightly less than 1000 members. The tail extends almost to 2000 elements.

The χ^2 test applied to the distributions confirms their difference, with a value of 80.13, always above the tabulated values for every significance level, for a number of degrees of freedom of 28, corresponding to the number of bins with more than 5 elements. The probability is $p = 6 \times 10^{-7}$. The reduced χ^2 distribution is showed in the second panel of the same figure and is consituted of two valleys, one around 500 units and the other around 600 units and of two peaks, around 700 and 900 elements.

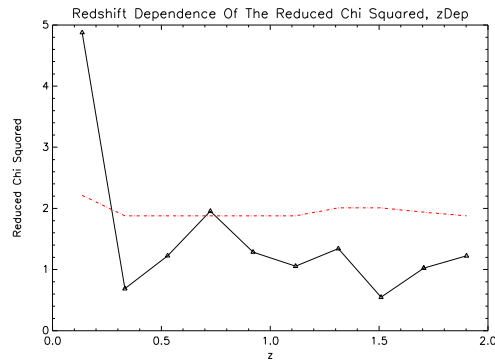
A KS test applied to the data results in a probability 9.16×10^{-13} of the two distributions being drawn from the same parent population.



(a) *Group Richness Distribution.* The solid black line refers to the radio-optical sample, while the red dash-dot line to the control sample. The whole richness range has been divided in 100 bins.

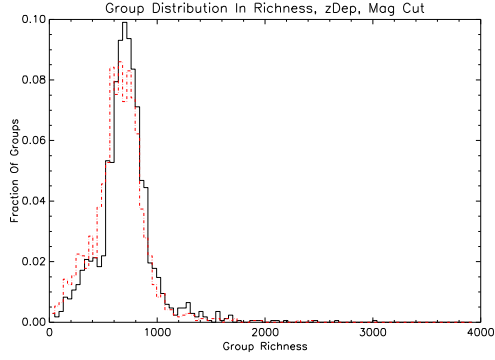


(b) *Reduced χ^2 Distribution.* The χ^2 test has been applied to the distributions above and it results in $\chi^2 = 110.53$ and $p = 1.2 \times 10^{-6}$. A KS test applied to the data results in a probability 3.21×10^{-11} of the two distributions being drawn from the same parent population.

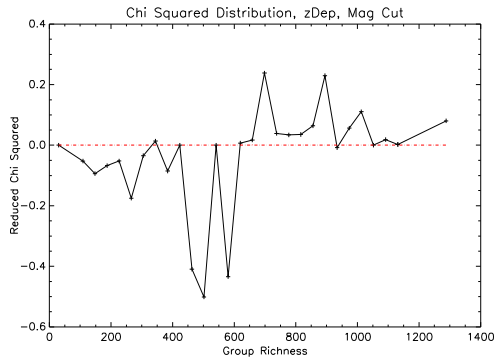


(c) *Redshift Dependence Of The Reduced χ^2 .* The red dash-dot line represents the tabulated χ^2 value for a significance value of 0.05.

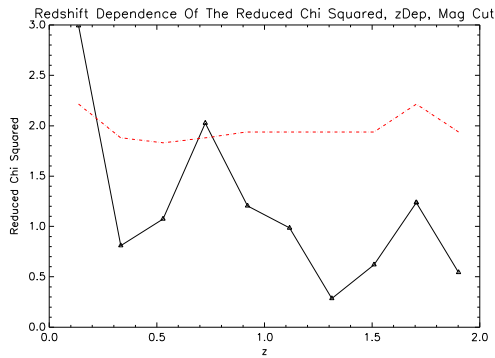
Figure 4.7: Redshift Dependent Coordinates



(a) *Group Richness Distribution.* The solid black line refers to the radio-optical sample, while the red dash-dot line to the control sample. The whole size range has been divided in 100 bins. The cut in apparent magnitude to 26.5 has been applied.



(b) *Reduced χ^2 Distribution.* The χ^2 test has been applied to the distributions above, with a result of $\chi^2 = 80.13$ and $p = 6 \times 10^{-7}$. A KS test applied to the data results in a probability 9.16×10^{-13} of the two distributions being drawn from the same parent population.



(c) *Redshift Dependence Of The Reduced χ^2 .* The red dash-dot line represents the tabulated χ^2 value for a significativity value of 0.05.

Figure 4.8: Redshift Dependent Coordinates, Apparent Magnitude Cut.

In the third panel of the same figure the results of the redshift analysis of the group richness distributions are given. The two distributions have been divided in 10 redshift bins. The dependence of the reduced χ^2 from redshift is quite strong. A few points are above the tabulated value of the χ^2 distribution for the 0.05 significance level (red dash-dot line).

4.4.2 Specific Star Formation Rate And Stellar Mass Cut

A procedure similar to the one described in section 4.3.2 has been applied to the radio-optical sample and to the control sample, before running the group search algorithm on both. The samples have both been cut to apparent I-band magnitude lower than 26.5 and to stellar mass $\log(\frac{M^*}{M_\odot}) > 10$. They have then been divided into galaxies having $\log(SSFR) > -11$ and $\log(SSFR) < -11$. The outputs of the groupsearch algorithm applied on both samples are showed in figures 4.9 and 4.10.

A χ^2 test has been executed to the four distributions (radio-optical samples and control samples with both cuts). The results are showed in the same figures. Values of χ^2 are 38.14 for galaxies from the $\log(SSFR) < -11$ sample and of 52.56 from the complementary sample, with probabilities p respectively 0.004 and 0.07. The first value of χ^2 is always above the tabulated values for every significativity level for a number of degrees of freedom of 18, while the second is above the tabulated values for a significance level of 0.1, with a number of degrees of freedom of 39, therefore seeming to exclude the possibility of the various distributions being different.

Nevertheless, Kolmogorov-Smirnov tests have been performed on both the samples. They result in probabilities of the distributions coming from the same parent population of $p = 1.56 \times 10^{-8}$ and of $p = 1.5 \times 10^{-6}$ respectively for the $\log(SSFR) < -11$ and for the complementary sample, both very low values.

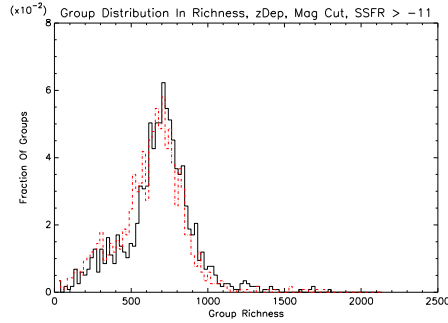
In the upper panel of figure 4.9 the group richness distributions for the radio-optical sample (solid black line) and for the control sample (red dash-dot line) are showed, for the $\log(SSFR) > -11$ sample. They both have a wide peak for group of about 700 elements, but the group distribution around galaxies from the radio-optical sample is slightly shifted towards higher richness values.

The χ^2 distribution is showed in the second panel of the same figure. It is composed of a peak around 950 elements and of a deep valley around 500 units.

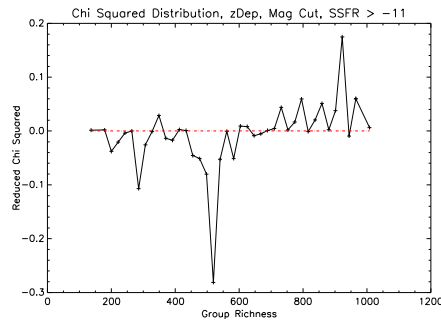
As before the redshift dependence of the reduced χ^2 has been examined, dividing the distributions in 10 redshift bins. The result is showed in the third panel of the same figure. It can be seen that the reduced χ^2 dependency from redshift is present, although all of the redshift bins have reduced χ^2 values under the tabulated ones for a significativity value of 0.05.

In the upper panel of figure 4.10 the group richness distributions for the radio-optical sample (solid black line) and for the control sample (red dash-dot line) for the $\log(SSFR) < -11$ are plotted. They are both constituted of a large peak for groups situated between 600 and 1000 elements, although in a less definite way, since there are less elements constituting the distributions. In the second panel of the same figure the χ^2 distribution is showed. It is quite irregular, with a broad peak around 800 elements and a deep valley at 700 units.

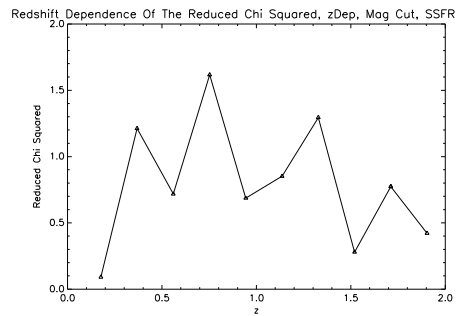
As in the previous cases the redshift dependence inspection on the distributions has been performed, the results are showed in the third panel of the same figure. The redshift dependence seems to be quite strong as the reduced



(a) *Group Richness Distribution.* The solid black line refers to the radio-optical sample, while the red dash-dot line to the control sample. The whole size range has been divided in 100 bins. The cut in apparent magnitude to 26.5 has been applied. The cuts in stellar mass and to $\log(SSFR) > -11$ have been applied.

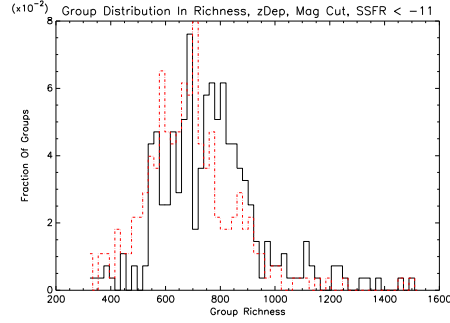


(b) *Reduced χ^2 Distribution.* The χ^2 test has been applied to the distributions above. The result is 52.56, with a probability $p = 0.07$. A KS test applied to the data results in a probability 1.5×10^{-6} of the two distributions being drawn from the same parent population.

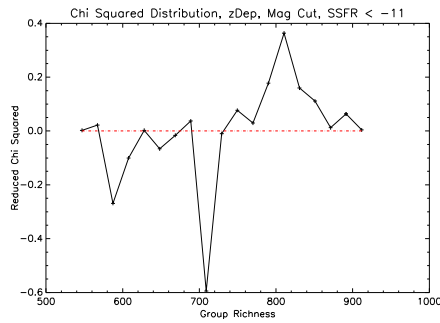


(c) *Third Panel: Redshift Dependence Of The Reduced χ^2 .* The red dash-dot line (here not showed since situated far above the upper edge of the plot) represents the tabulated χ^2 value for a significativity value of 0.05.

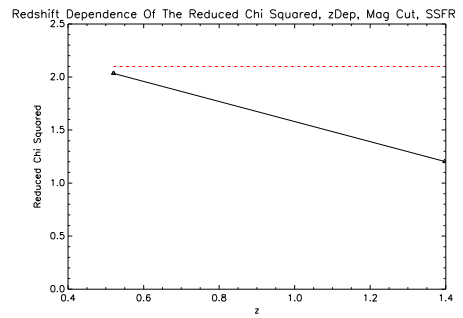
Figure 4.9: Redshift Dependent Coordinates, Apparent Magnitude Cut, SSFR And Stellar Mass Cut



(a) *Group Richness Distribution.* The solid black line refers to the radio-optical sample, while red the dash-dot line to the control sample. The whole richness range has been divided in 60 bins. The cut in apparent magnitude to 26.5 has been applied. The cuts in stellar mass and to $\log(SSFR) < -11$ have been applied.



(b) *Reduced χ^2 Distribution.* The χ^2 test has been applied to the distributions above, resulting in $\chi^2 = 38.14$ and $p = 0.004$. A KS test applied to the data results in a probability 1.56×10^{-8} of the two distributions being drawn from the same parent population.



(c) *Redshift Dependence Of The Reduced χ^2 .* The red dash-dot line represents the tabulated χ^2 value for a significance value of 0.05.

Figure 4.10: Redshift Dependent Coordinates, Apparent Magnitude Cut, SSFR And Stellar Mass Cut

χ^2 varies of a great amount in the redshift range examined. Values in the two redshift bins are always under the tabulated ones for a significativity level of 0.05 (red dash-dot line).

4.4.3 Stellar Mass And Specific Star Formation Rate Selections Applied Also To The Optical Sample

As in the case of the fixed distance (previous section, 4.3.2), the samples have been furtherly reduced by applying to the optical sample the same cuts in stellar mass and specific star formation rate as those applied to the radio-optical sample and the control sample. The group search algorithm has been run again on the radio-optical and control samples with the stellar mass and specific star formation rate cuts, searching for galaxies to be in groups between those belonging to the optical sample cut in the same way as the other samples.

The following figures show the results of the search for groups.

In the upper panel of figure 4.11 the group richness distributions for the radio-optical sample (solid black line) and for the control sample (red dash-dot line) for the cut to $\log(\frac{M^*}{M_\odot}) > 10$ and $\log(SSFR) < -11$ also to the optical sample are given. The plot shows two distributions with a wide peak for groups with a number of elements from 0 to less than 50 elements.

A χ^2 test performed on the distributions results in a value of 22.87, above the tabulated values only down to a significativity level of 0.1 for a number of degrees of freedom of 15. The probability of the two distributions being drawn from the same parent population is of 0.08. The χ^2 distribution is showed in the second panel of figure 4.11. It is very irregular, due to the low number of counts in each bin, with a few valleys in the range from 0 to 20 units.

A KS test applied to the data results in a very low probability of 9.19×10^{-9} of the two distributions being drawn from the same parent population.

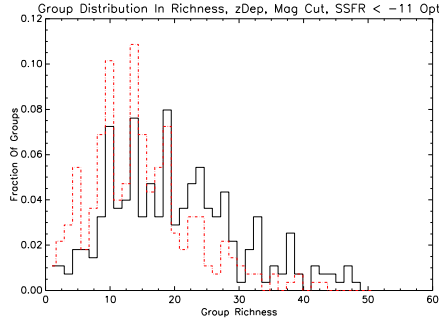
The results of the redshift analysis of the distributions are showed in the third panel of the same figure. The reduced χ^2 has a strong variation in the redshift range, suggesting a strong redshift effect, although the number of redshift bins is low.

In the upper panel of figure 4.12 the group richness distributions for the radio-optical sample (solid black line) and for the control sample (red dash-dot line) for the cut to $\log(\frac{M^*}{M_\odot}) > 10$ and $\log(SSFR) > -11$ also to the optical sample are given. The plot shows two distributions with a wide peak for groups with a number of elements from 0 to about 120 elements. The distributions are similar in shape.

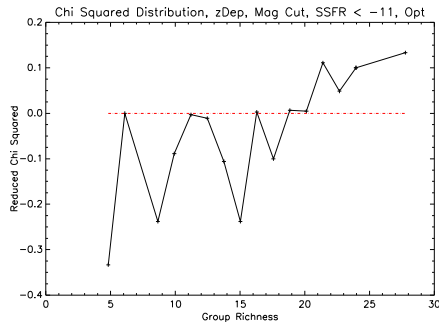
A χ^2 test performed on the distributions results in a value of 50.5, above the tabulated values only down to a significativity level of 0.025 for a number of degrees of freedom of 30, corresponding to the number of bins with at least 5 elements. The probability of the two distributions of being drawn from the same parent population is of 0.01. The χ^2 distribution is showed in the second panel of figure 4.12. It is very irregular, due to the low number of counts in each bin.

A KS test applied to the data results again in a low probability value of 1.0×10^{-7} of the two distributions being drawn from the same parent population.

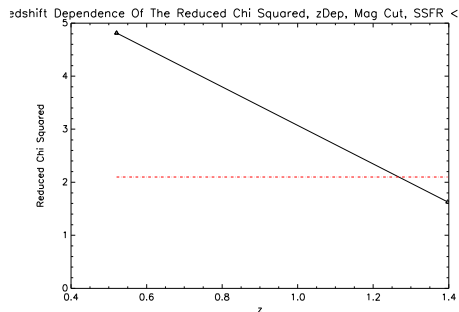
The redshift dependence of the reduced χ^2 is showed in the third panel of the same figure. The dependence is not very strong but the values are always



(a) *Group Richness Distribution.* The solid black line refers to the radio-optical sample, while the red dash-dot line to the control sample. The whole richness range has been divided in 40 bins. The cut in apparent magnitude to 26.5 has been applied. The cuts in stellar mass and to $\log(SSFR) < -11$ have been applied, the optical sample has been cut in the same way.

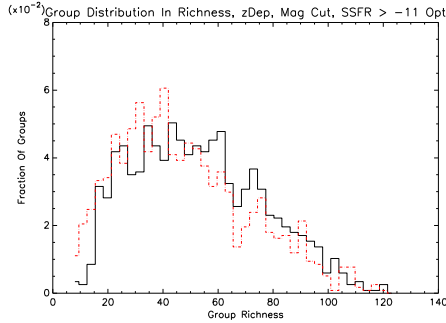


(b) *Reduced χ^2 Distribution.* The χ^2 test has been applied to the distributions above. The results are $\chi^2 = 22.87$ and $p = 0.08$. A KS test applied to the data results in a probability 9.19×10^{-9} of the two distributions being drawn from the same parent population.

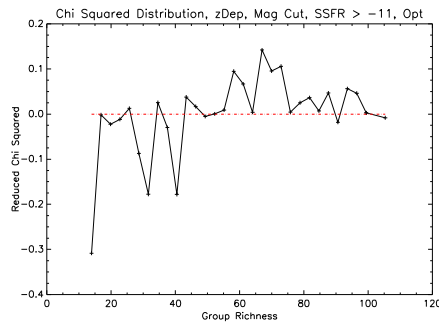


(c) *Redshift Dependence Of The Reduced χ^2 .* The red dash-dot line represents the tabulated χ^2 value for a significance value of 0.05.

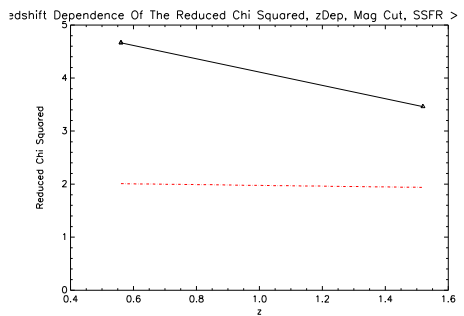
Figure 4.11: Redshift Dependent Coordinates, Apparent Magnitude Cut, SSFR And Stellar Mass Cut Applied Also To The Optical Sample



(a) *Group Richness Distribution.* The solid black line refers to the radio-optical sample, while the red dash-dot line to the control sample. The whole richness range has been divided in 40 bins. The cut in apparent magnitude to 26.5 has been applied. The cuts in stellar mass and to $\log(SSFR) > -11$ have been applied, the optical sample has been cut in the same way.



(b) *Reduced χ^2 Distribution.* The χ^2 test has been applied to the distributions above. The results are $\chi^2 = 50.5$ and $p = 0.01$. A KS test applied to the data results in a probability 1.0×10^{-7} of the two distributions being drawn from the same parent population.



(c) *Redshift Dependence Of The Reduced χ^2 .* The red dash-dot line represents the tabulated χ^2 value for a significance value of 0.05.

Figure 4.12: Redshift Dependent Coordinates, Apparent Magnitude Cut, SSFR And Stellar Mass Cut Applied Also To The Optical Sample

above the tabulated ones for a χ^2 distribution for a significance level of 0.05 (red dash-dot line).

A summary of the results exposed in the present section are given in table 4.3. In every line the type of the sample, the number of galaxies in the radio-optical sample (N_{RO}), the number of galaxies in the control sample (N_C) and the probability p_{KS} of the Kolmogorov-Smirnov test of the two distributions coming from the same parent population are given.

Type Of Sample	N_{RO}	N_C	p_{KS}
Total Sample	1806	1806	3.21×10^{-11}
$magI < 26.5$	1687	1687	9.16×10^{-13}
$\log(\frac{M^*}{M_\odot}) > 10$ And $\log(SSFR) < -11$	276	276	1.56×10^{-8}
$\log(\frac{M^*}{M_\odot}) > 10$ And $\log(SSFR) > -11$	1172	1172	1.5×10^{-11}
$\log(\frac{M^*}{M_\odot}) > 10$ And $\log(SSFR) < -11$, Also To Optical Sample	276	276	9.19×10^{-19}
$\log(\frac{M^*}{M_\odot}) > 10$ And $\log(SSFR) > -11$, Also To Optical Sample	1172	1172	1.0×10^{-7}

Table 4.3: The Study Of The Environment, Redshift Dependent Radius

4.5 The Check For Significativity

The results discussed in the sections above, although quite interesting and well defined, have to be tested in order to check whether they are truly significant. To do so, the number of extractions of the control sample has been increased, in order to augment the statistic of the analysis.

To begin, a set of 100 extractions of 1806 random Right Ascensions and Declinations has been performed, in order to create the equivalent of 100 control samples comparable to the one described in section 4.3.

The group search algorithm has been run on each of these 100 control samples and the group richness distribution has been derived for each of them.

A comparison of the group richness distributions between the radio-optical sample and each one of the 100 control samples has been carried out, together with a χ^2 test, creating a list of a 100 values of reduced χ^2 .

An histogram representing the reduced χ^2 value distribution has been drawn and it is showed in figure 4.13.

It can be seen that the value of the reduced χ^2 for the same samples, derived from the quantities in the caption of the first panel of figure 4.1, is of 2.42, therefore falling to the right edge of the distribution. The solid red line in the plot represents the tabulated value of the reduced χ^2 for a significativity level of 0.005. It can be seen that the whole distribution falls in a range of higher values than the tabulated ones. Therefore, even with such a large statistic, the differences between the radio-optical sample and the control one are real, confirming a difference in the properties of protogroups around radio-galaxies.

A similar analysis has been carried out also for the samples described in section 4.3.1. In particular, a sample of 100 extractions of 1687 galaxies has been created, and the group search algorithm has been run on each of them, together with the 1687 galaxies from the radio-optical sample. Every one of the 100 extractions, similar to 100 control samples, has been compared to the radio-optical sample and the group richness distributions have been derived for

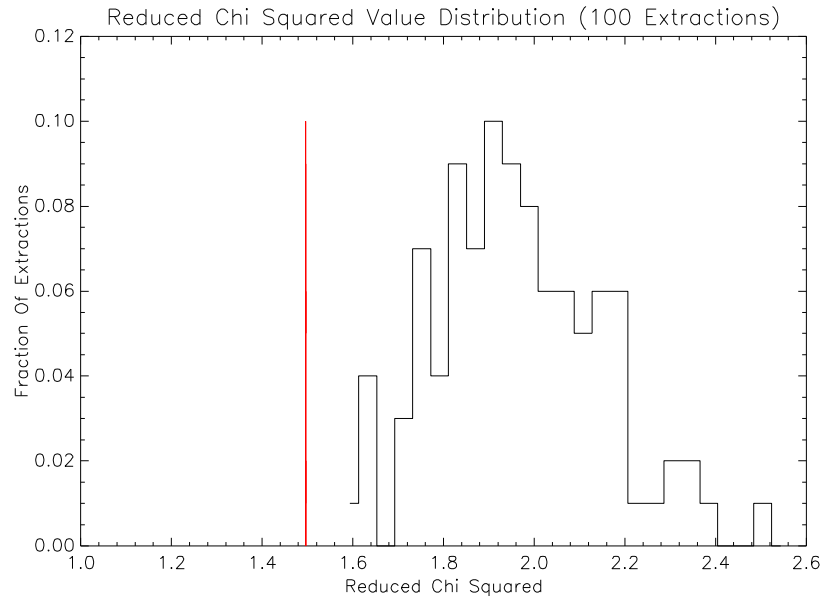


Figure 4.13: Reduced χ^2 Value Distribution. The black line represents the distribution of the 100 reduced χ^2 values obtained by comparing the radio-optical sample to the 100 control samples extracted as described in text. The red line represents the tabulated value for a significativity level of 0.005.

both. They have been compared through a χ^2 test, similar to what done in figure 4.2, gathering a sample of 100 values of reduced χ^2 . A distribution of these values has been created and it is shown in figure 4.14.

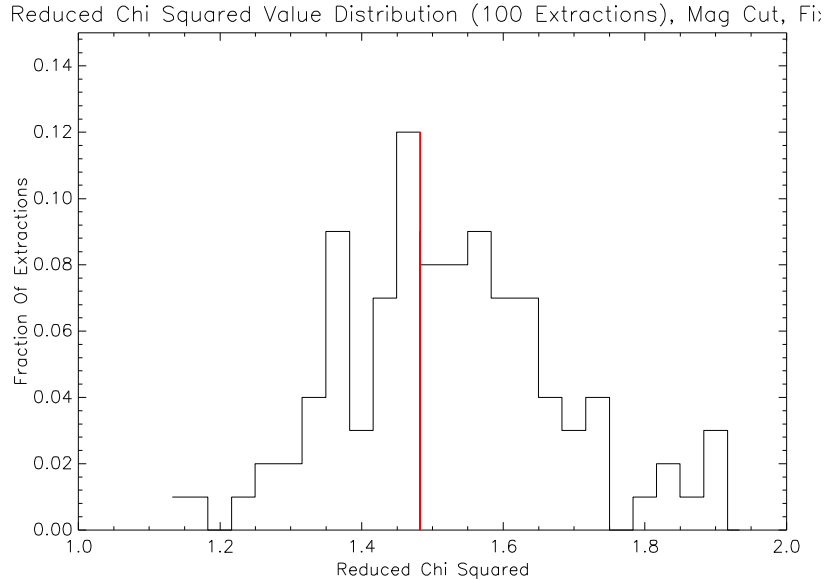


Figure 4.14: Reduced χ^2 Value Distribution. The black line represents the distribution of the 100 reduced χ^2 values obtained by comparing the radio-optical sample to the 100 control samples extracted as described in text. The red line represents the tabulated value for a significance level of 0.005. The magnitude cut to 26.5 has been applied to the data.

It can be seen that the value of reduced χ^2 of 1.47 derived from the quantities in caption of figure 4.2 falls in the middle of the distribution. Again the solid line represents the reduced χ^2 distribution for the radio-optical sample and the 100 control samples, while the red line represents the tabulated value for a significance value of 0.005. It can be seen that a consistent portion of the distribution is above the tabulated threshold therefore opening a chance of significance for the difference between the radio-optical and the control samples with the magnitude cut.

Quite different is instead the situation for the sample with the 26.5 apparent I-band magnitude cut and the cut to $\log(\frac{M^*}{M_\odot}) > 10$ and to $\log(SSFR) < -11$, described in section 4.3.2, and whose group richness distributions are showed in figure 4.3. The same analysis as before has been performed, *i.e.* a comparison between the 276 galaxies of the radio-optical sample with the cuts described and a sample of 100 extractions of 276 galaxies each. This results in a sample of 100 values of reduced χ^2 whose distribution is showed in figure 4.15. The red line represents the tabulated value for a significance level of 0.005.

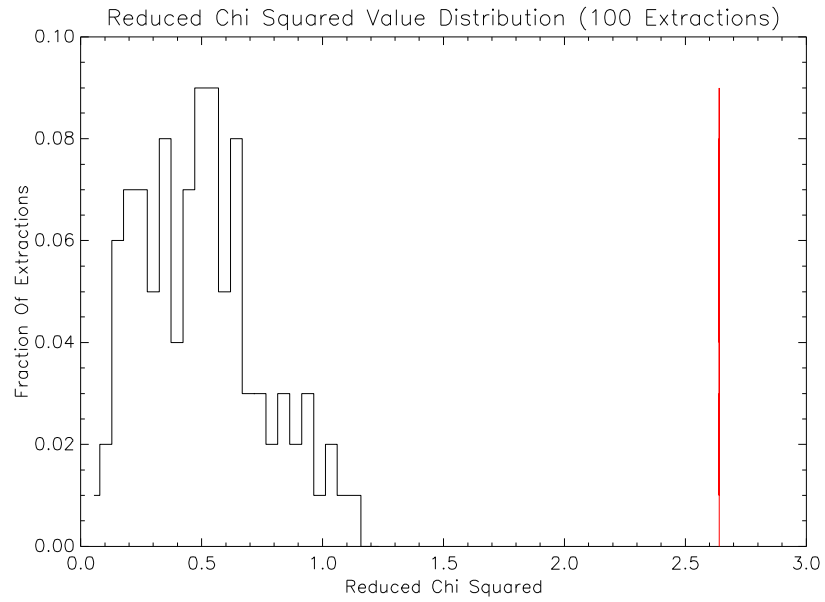


Figure 4.15: Reduced χ^2 Value Distribution. The black line represents the distribution of the 100 reduced χ^2 values obtained by comparing the radio-optical sample to the 100 control samples extracted as described in text. The red line represents the tabulated value for a significativity level of 0.005. The magnitude cut to 26.5 and the cuts to $\log(\frac{M^*}{M_\odot}) > 10$ and to $\log(SSFR) < -11$ have been applied to the data.

It can be seen that the value of reduced χ^2 of 0.27 derived from the quantities in the caption of figure 4.3 falls in the middle of the distribution. For this sample all of the differences found in the properties of protogroups around radiogalaxies cannot be considered as significant on the basis of this test, since the whole reduced χ^2 values distribution is under the tabulated value.

A similar result is found for the sample with the magnitude cut to 26.5 and the cuts to $\log(\frac{M^*}{M_\odot}) > 10$ and to $\log(SSFR) > -11$, complementary to the one described above. The reduced χ^2 value distribution is showed in figure 4.16.

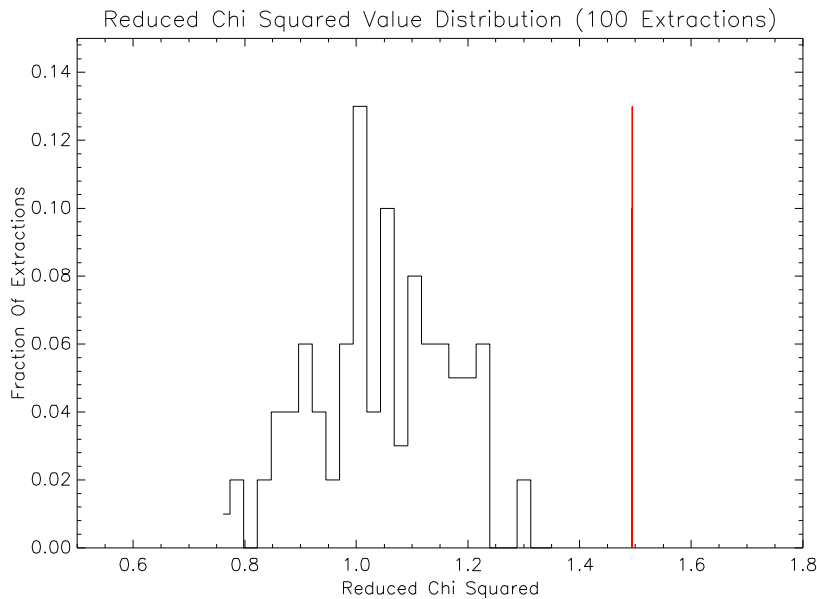


Figure 4.16: Reduced χ^2 Value Distribution. The black line represents the distribution of the 100 reduced χ^2 values obtained by comparing the radio-optical sample to the 100 control samples extracted as described in text. The red line represents the tabulated value for a significance level of 0.005. The magnitude cut to 26.5 and the cuts to $\log(\frac{M^*}{M_\odot}) > 10$ and to $\log(SSFR) > -11$ have been applied to the data.

The distribution of values is always below the tabulated value for a significance level of 0.005 (red line). This confirms the lack of significance for the differences found between the group richness distributions showed in figure 4.4, on the basis of the χ^2 test.

The same analysis has also been performed on the samples discussed in section 4.3.3, figures 4.5 and 4.6. In particular, in figure 4.17, the sample with the apparent I-band magnitude cut to 26.5 and the cuts to $\log(\frac{M^*}{M_\odot}) > 10$ and to $\log(SSFR) > -11$ applied to both the radio-optical and the optical sample has been analyzed through the extraction of 100 control samples of 1172 galaxies each and the comparison of the group richness distributions of each of them

with the distribution coming from the radio-optical sample. The reduced χ^2 value distribution is showed in figure 4.17.

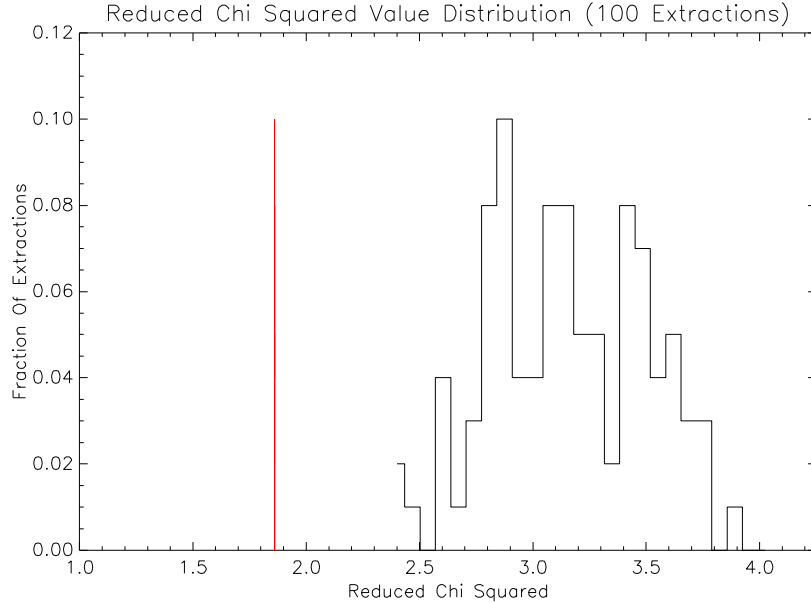


Figure 4.17: Reduced χ^2 Value Distribution. The black line represents the distribution of the 100 reduced χ^2 values obtained by comparing the radio-optical sample to the 100 control samples extracted as described in text. The red line represents the tabulated value for a significativity level of 0.005. The magnitude cut to 26.5 and the cuts to $\log(\frac{M^*}{M_\odot}) > 10$ and to $\log(SSFR) > -11$ have been applied to the data, including the optical sample.

It can be seen that the value of reduced χ^2 of 3.81 calculated from the data in caption of figure 4.6 falls close to the right edge of the distribution. The whole distribution of the reduced χ^2 values is above the tabulated value for a significativity level of 0.005 (red line in plot), therefore granting significativity for the results regarding the sample.

The complementary sample, with apparent I-band magnitude cut to 26.5 and cuts to $\log(\frac{M^*}{M_\odot}) > 10$ and to $\log(SSFR) < -11$ applied both to the radio-optical and to the optical sample is analyzed in figure 4.18.

The reduced χ^2 value of 4.79 calculated from the data in caption of figure 4.5 is situated in the right part of the distribution. The reduced χ^2 value distribution is for its majority above the tabulated value for a significativity level of 0.005, which means that the difference between the properties of the radio-optical sample with the cuts applied and the properties of the normal galaxies, such as those from the control sample, are significant.

The whole analysis described in the paragraphs above has been done also for the groups found around the galaxies from the radio-optical and the control

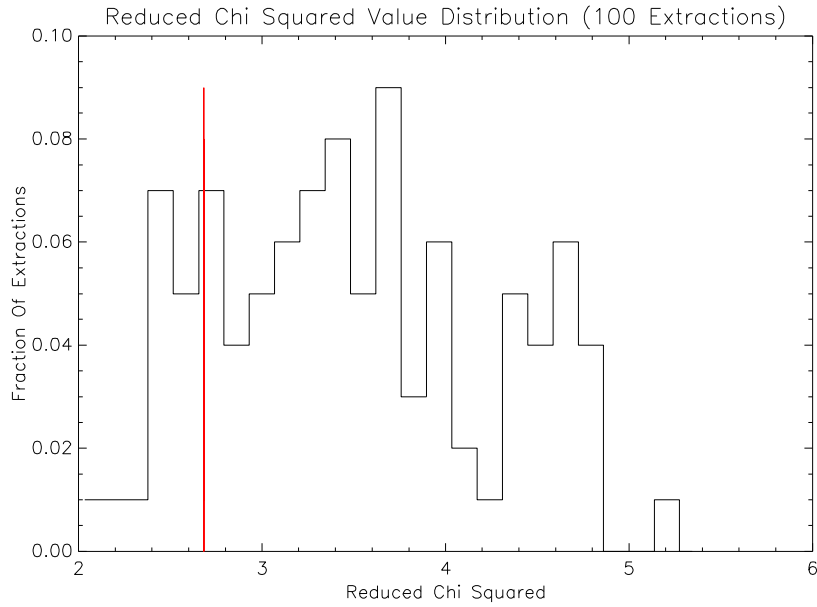


Figure 4.18: Reduced χ^2 Value Distribution. The black line represents the distribution of the 100 reduced χ^2 values obtained by comparing the radio-optical sample to the 100 control samples extracted as described in text. The red line represents the tabulated value for a significance level of 0.005. The magnitude cut to 26.5 and the cuts to $\log(\frac{M^*}{M_\odot}) > 10$ and to $\log(SSFR) < -11$ have been applied to the data, including the optical sample.

sample, with the implementation of the dependence from redshift in the group search algorithm, as described and discussed in section 4.4.

The first output of the analysis is showed in figure 4.19.

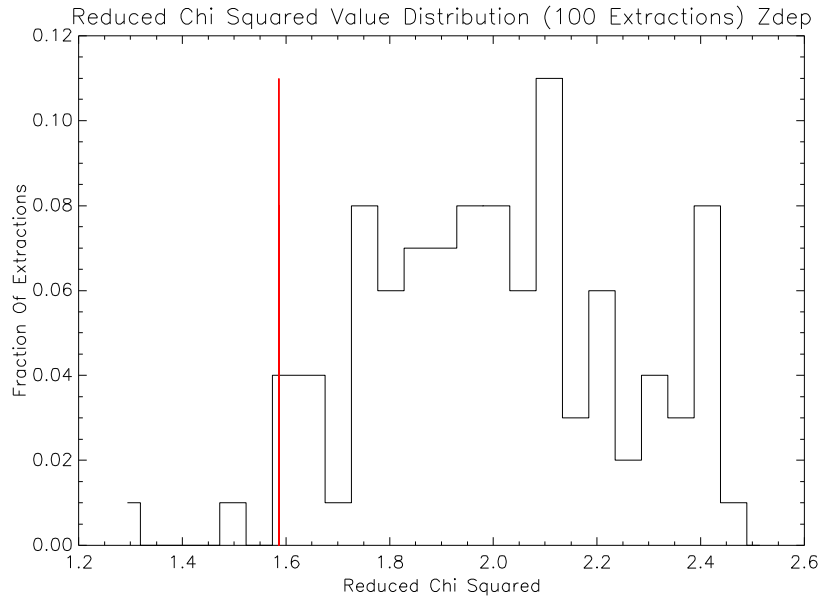


Figure 4.19: Reduced χ^2 Value Distribution. The black line represents the distribution of the 100 reduced χ^2 values obtained by comparing the radio-optical sample to the 100 control samples extracted as described in text. The red line represents the tabulated value for a significance level of 0.005. The redshift dependence has been implemented.

The analysis performed is exactly the same as for the samples above. The group richness distribution of the radio-optical sample has been compared through a reduced χ^2 test with the 100 extractions of 1806 galaxies each. The reduced χ^2 value distribution has been derived and is showed in figure 4.19. It can be seen that the great majority of the distribution is above the tabulated value for a significance level of 0.005 (red line). Therefore the difference in group properties around galaxies from the radio-optical sample compared to those around normal galaxies is significant. The value of reduced χ^2 calculated from the quantities in caption of figure 4.7 is $\chi^2 = 2.26$ which falls perfectly inside the distribution showed in the figure.

As in the case of the group search without redshift dependence, a cut to apparent I-band magnitude 26.5 has been applied to the data. The analysis has then been realized in the same way, by comparing the group richness distributions of the radio-optical sample and of the 100 extractions of random galaxies. The reduced χ^2 value distribution resulting is showed in figure 4.20.

It is easily seen that all of the values of the distribution are above the tab-

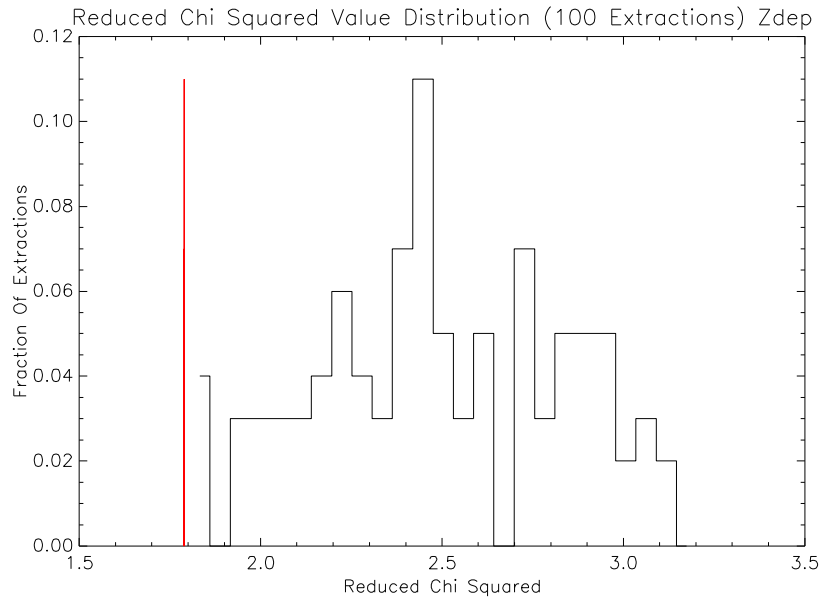


Figure 4.20: Reduced χ^2 Value Distribution. The black line represents the distribution of the 100 reduced χ^2 values obtained by comparing the radio-optical sample to the 100 control samples extracted as described in text. The red line represents the tabulated value for a significance level of 0.005. The redshift dependence has been implemented. The apparent I-band magnitude cut to 26.5 has been applied to the data.

ulated one for a significance level of 0.005 (red line), therefore making the results for the sample significant. The value of reduced χ^2 of 2.86, calculated from the quantities in the caption of figure 4.8 is perfectly situated inside the value distribution.

In figure 4.21 is showed the reduced χ^2 value distribution for the comparison between the radio-optical sample and the 100 control samples both with the cuts to apparent I-band magnitude 26.5, $\log(\frac{M^*}{M_\odot}) > 10$ and $\log(SSFR) > -11$, described in section 4.4.2.

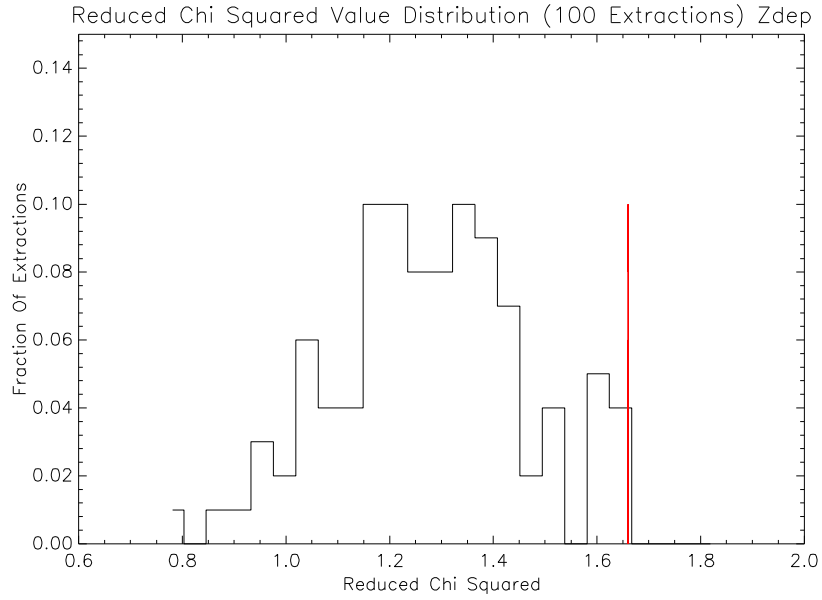


Figure 4.21: Reduced χ^2 Value Distribution. The black line represents the distribution of the 100 reduced χ^2 values obtained by comparing the radio-optical sample to the 100 control samples extracted as described in text. The red line represents the tabulated value for a significance level of 0.005. The redshift dependence has been implemented. The apparent I-band magnitude cut to 26.5 has been applied to the data, as well as the cuts to $\log(\frac{M^*}{M_\odot}) > 10$ and $\log(SSFR) > -11$.

The significance for this sample cannot be assured since all of the reduced χ^2 value distribution is under the tabulated value for a significance level of 0.005 (red-line). The value of reduced χ^2 of 1.35, calculated from the values found in the caption of figure 4.9, falls in the distribution.

The same situation is found also for the complementary sample, with the cuts to apparent I-band 26.5, to $\log(\frac{M^*}{M_\odot}) > 10$ and $\log(SSFR) < -11$. The reduced χ^2 value distribution is showed in figure 4.22. The significance for the sample is questionable since all of the values of the distribution are under the tabulated one for a significance value of 0.005 (red line).

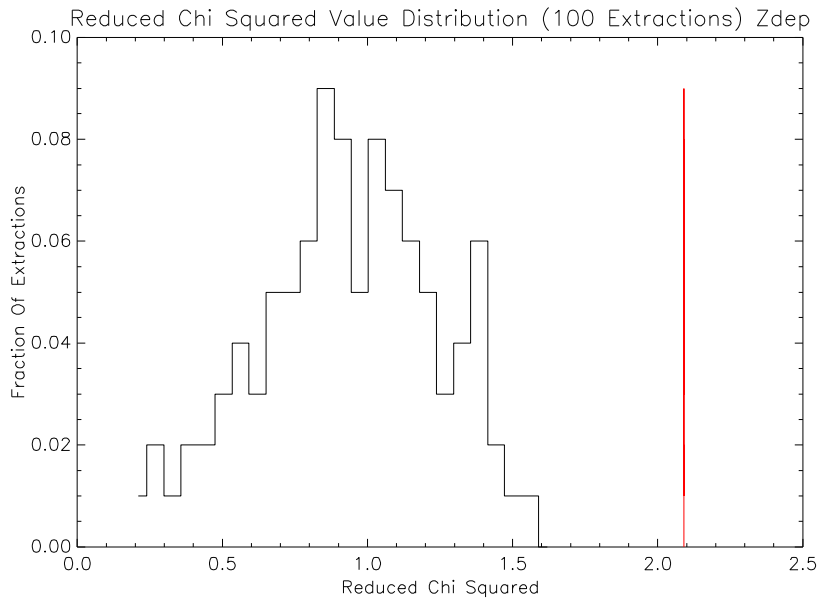


Figure 4.22: Reduced χ^2 Value Distribution. The black line represents the distribution of the 100 reduced χ^2 values obtained by comparing the radio-optical sample to the 100 control samples extracted as described in text. The red line represents the tabulated value for a significance level of 0.005. The redshift dependence has been implemented. The apparent I-band magnitude cut to 26.5 has been applied to the data, as well as the cuts to $\log(\frac{M^*}{M_\odot}) > 10$ and $\log(SSFR) < -11$.

The same cuts to stellar mass and specific star formation rate have been applied also to the optical sample. The 100 extractions have been realized and the check for significativity has been done. Figure 4.23 shows the reduced χ^2 value distribution, obtained comparing the groups from the radio-optical sample and the 100 control samples, using for the optical sample the same cuts as for the radio-optical and each one of the control samples, namely to apparent I-band magnitude 26.5, $\log(\frac{M^*}{M_\odot}) > 10$ and to $\log(SSFR) > -11$, as described in section 4.4.3. It can be seen that the reduced χ^2 distribution is always below the tabulated reduced χ^2 value for a significance level of 0.005.

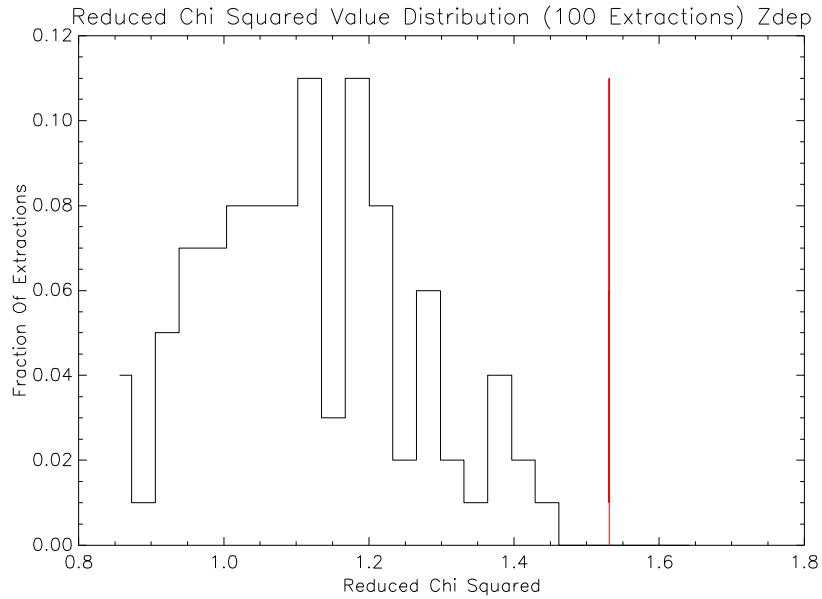


Figure 4.23: Reduced χ^2 Value Distribution. The black line represents the distribution of the 100 reduced χ^2 values obtained by comparing the radio-optical sample to the 100 control samples extracted as described in text. The red line represents the tabulated value for a significativity level of 0.005. The redshift dependence has been implemented. The apparent I-band magnitude cut to 26.5 has been applied to the data, as well as the cuts to $\log(\frac{M^*}{M_\odot}) > 10$ and $\log(SSFR) > -11$, also to the optical sample.

The same analysis has been performed also on the complementary sample, the one with the cuts to $\log(\frac{M^*}{M_\odot}) > 10$ and $\log(SSFR) < -11$. The reduced χ^2 value distribution (showed in figure 4.24) is always below the tabulated value for a significativity level of 0.005, therefore not assuring the significance of the results.

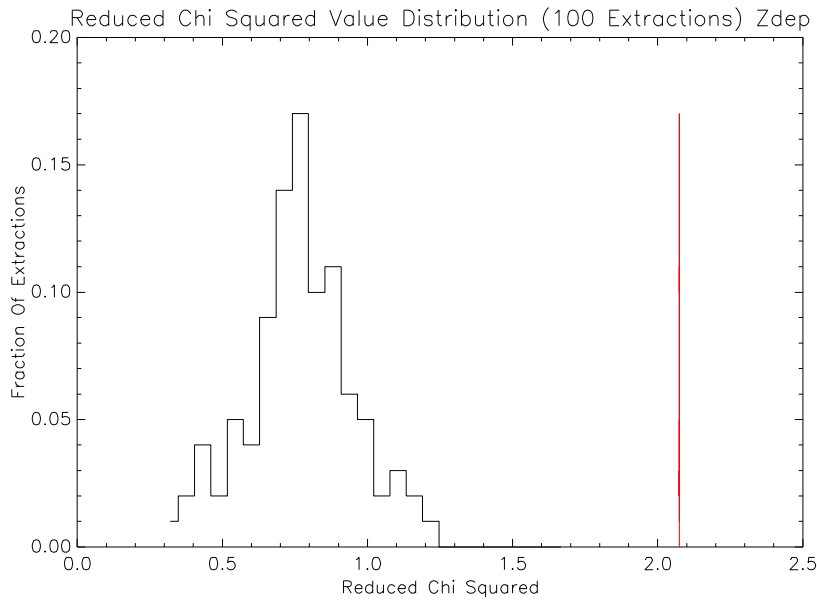


Figure 4.24: Reduced χ^2 Value Distribution. The black line represents the distribution of the 100 reduced χ^2 values obtained by comparing the radio-optical sample to the 100 control samples extracted as described in text. The red line represents the tabulated value for a significance level of 0.005. The redshift dependence has been implemented. The apparent I-band magnitude cut to 26.5 has been applied to the data, as well as the cuts to $\log(\frac{M^*}{M_\odot}) > 10$ and $\log(SSFR) > -11$, also to the optical sample.

4.6 Conclusions

In this chapter the core of the data analysis is performed and described. This analysis consists in the study of the environment around the galaxies of the radio-optical sample.

The searching algorithm which has been created for the study of the environment is optimized to search galaxies in the optical sample that have coordinates equal, within a small interval, to the coordinates of the galaxies from the radio-optical sample. By choosing the interval wisely it is possible to study the environment around every radiogalaxy.

It has been chosen to study the presence of galaxies from the optical sample around the galaxies of the radio-optical sample on a scale of 1 Mpc, typical of clusters of galaxies. In order to check the consistency of the results a control sample has been created by substituting the coordinates of every radiogalaxy with others extracted randomly from the optical sample. It is possible to consider this control sample as a compilation of galaxies not showing radio emission. The group search algorithm has been run on each galaxy of the control sample.

The first attempt in the research for groups of galaxies has been made by ignoring the dependence from redshift of the coordinate variations corresponding to the radius of the research. The algorithm has been applied both on the radio-optical sample and the control sample. The two distributions have been compared and a χ^2 test has been run, together with a Kolmogorov-Smirnov test. Results are summarized in the table at the end of the section (table 4.2). Various cuts have been applied to both the radio-optical, the optical and the control samples: a cut to apparent I-band magnitude 26.5, a cut to $\log(\frac{M^*}{M_\odot}) > 10$ and a distinction between galaxies with $\log(SSFR)$ greater and lower than -11 . Everytime the group search algorithm has been run again and the distributions have been compared through a χ^2 test and a KS test. The results are showed in the same table.

An improvement has been made by implementing in the algorithm the dependence from redshift, through the integration of the cosmological equations. The search for groups together with the cuts described in the paragraph above have been re-run with the new changes and the various distributions have been compared through the χ^2 test and the Kolmogorov-Smirnov test. The results are summarized in table 4.3.

The significativity of the results has been tested by increasing the number of control samples to a total of 100 random extractions and deriving the distribution of the reduced χ^2 values.

Chapter 5

The Study Of The Environment - A Restriction To $1 \leq z \leq 2$

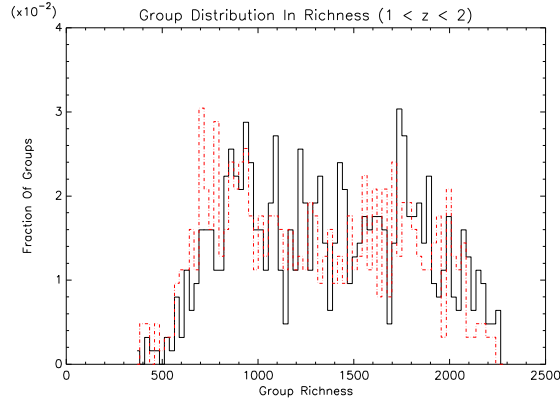
THE analysis performed in the previous chapter has been taken to a further refined step, by considering only a restriction of the samples to redshifts between 1 and 2. This restriction has been made since it is assumed that in the redshift interval considered the bulk of the cluster aggregation should be performed. Moreover it is possible to compare this work of thesis with other similar works which analyzed samples with $1 \leq z \leq 2$. This will be achieved in chapter 6. This chapter is structured as it follows: in section 5.1 the analysis of the group richness distributions for the samples restricted to $1 \leq z \leq 2$ will be discussed, while in section 5.2 a cut in absolute radio luminosity will be applied, in order to analyze the effect of a distinction in the radio-optical sample based on the belonging of the sources to various kinds of AGNs based on their intrinsic radio power (namely Fanaroff-Riley class I and II objects.)

5.1 Analysis Of The Redshift Range $1 \leq z \leq 2$

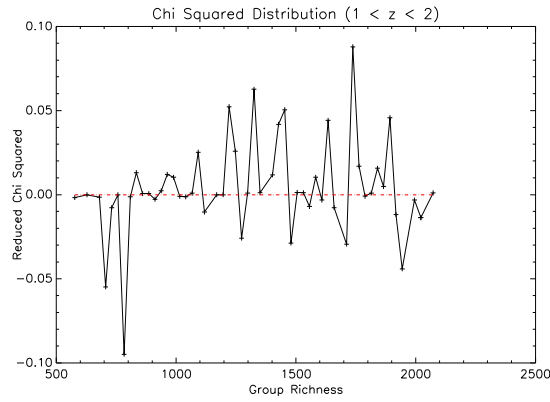
A restriction to the redshift range $1 \leq z \leq 2$ has been applied to the data composing the various compilations of groups. In particular, hereafter, the analysis of the group richness distributions for the groups found around galaxies from the radio-optical sample with the various cuts is proposed, with the cut in redshift. The groups analyzed are those found with the implementation of the dependence on redshift of the group search algorithm, as described in the sections 4.4, 4.4.1, 4.4.2 and 4.4.3.

In figure 5.1, the group richness distributions for galaxies of the radio-optical sample and of the control sample are given (upper panel, respectively solid black line and red dash-dot line).

The restriction to $1 \leq z \leq 2$ seems to have selected only groups with a number of elements from 500 to slightly less than 2500. The distributions are wide, with no pronounced peaks. A χ^2 test has been performed on the distributions (the reduced χ^2 distribution is showed in the lower panel of the same figure). The results are $\chi^2 = 45.66$ and $p = 0.69$, with a number of degrees of freedom



(a) *Group Richness Distribution.* The solid black line refers to the radio-optical sample, while the red dash-dot line to the control sample. The selection to $1 \leq z \leq 2$ has been applied, the number of galaxies in the sample is of 626.



(b) *Reduced χ^2 Distribution.* The χ^2 test has been applied to the distributions above. The results are $\chi^2 = 45.66$ and $p = 0.69$, with a number of degrees of freedom of 51. A KS test has been applied to the data and results in a probability of 0.0013 of the two distributions coming from the same parent population.

Figure 5.1: Redshift Dependent Coordinates, $1 \leq z \leq 2$.

of 51. The χ^2 value is never above the tabulated value for every significance level, therefore the difference between the two distributions cannot be considered significant. A Kolmogorov-Smirnov test has, nevertheless, been applied to the data and results in a probability of 0.0013 of the two distributions coming from the same parent population.

As done before, a cut in apparent I-band magnitude to 26.5 has been applied to the data. The group richness distributions for the radio-optical sample (solid black line) and for the control sample (red dash-dot line) in the case of $1 \leq z \leq 2$ have been derived and are showed in the upper panel of figure 5.2. In the lower panel of the same figure the reduced χ^2 distribution is showed.

Again, the distributions lack the groups with less than 400 elements and with more than 1000 elements. The distributions peak around 700 units. The χ^2 test has been applied to the distributions, results are $\chi^2 = 41.59$ and $p = 0.11$, with a number of degrees of freedom of 32. The value is above the tabulated one only for a significance level of 0.10. A KS test has also been applied to the data and it results in a low probability of 8×10^{-6} of the two distributions coming from the same parent population.

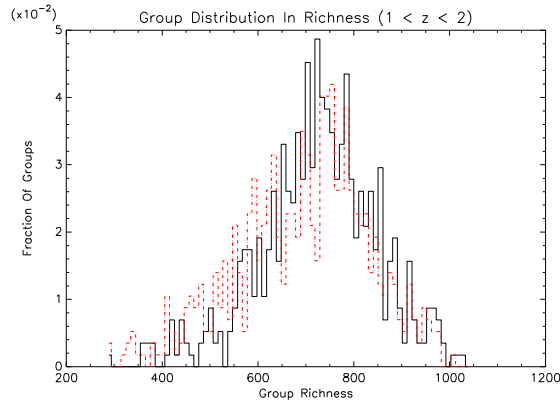
Figure 5.3 and 5.4 show the group richness distributions for the radio-optical sample (solid black line) and for the control sample (red dash-dot line) for the galaxies with the apparent I-band magnitude cut to 26.5 and with the cuts to $\log(\frac{M^*}{M_\odot}) > 10$ and $\log(SSFR) > -11$ (figure 5.3) and to $\log(\frac{M^*}{M_\odot}) > 10$ and $\log(SSFR) < -11$ (figure 5.4), both restricted to $1 \leq z \leq 2$.

The distributions showed in the upper panel of figure 5.3 again lack groups with less than 400 and with more than 1000 elements. The distributions have a peak around 700 elements. A χ^2 test has been performed, resulting in $\chi^2 = 14.67$ and $p = 0.88$, with a number of degrees of freedom of 22. This value is never above the tabulated one, therefore excluding the significance of the differences between the distributions. Nevertheless, a KS test applied to the data results in a probability of 5.7×10^{-5} of the two distributions coming from the same parent population, a very low value. The reduced χ^2 distribution is showed in the lower panel of figure 5.3.

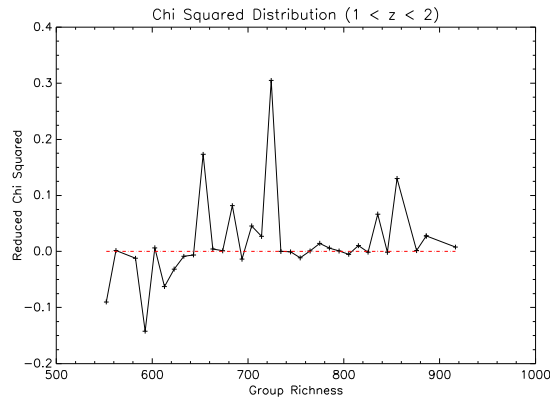
Figure 5.4 shows the group richness distributions (upper panel) and the reduced χ^2 distribution for the complementary sample. Unfortunately the sample suffers from a small statistic, which makes a detailed analysis difficult. The distributions are not significantly different as demonstrated by the χ^2 test performed with results $\chi^2 = 2.52$ and $p = 0.47$, with a number of degrees of freedom of 3, never above the tabulated value for every significance level. A KS test has been applied to the data and results in a probability of 0.51 of the distributions coming from the same parent population.

The restriction to $1 \leq z \leq 2$ has been applied also to the samples with the cuts in stellar mass and specific star formation rate also to the optical sample. Results are showed in figures 5.5 and 5.6 (upper panel: group richness distributions, with the solid black line representing the radio-optical sample and the red dash-dot line representing the control sample, lower panel: reduced χ^2 distribution).

Figure 5.5 refers to the sample with $\log(\frac{M^*}{M_\odot}) > 10$ and $\log(SSFR) > -11$, with, on the optical sample, the same cuts as on the radio-optical one. The distributions show values only between 20 and 120 elements. They are quite different, the χ^2 test applied to them results in $\chi^2 = 39.46$ and $p = 0.04$, with

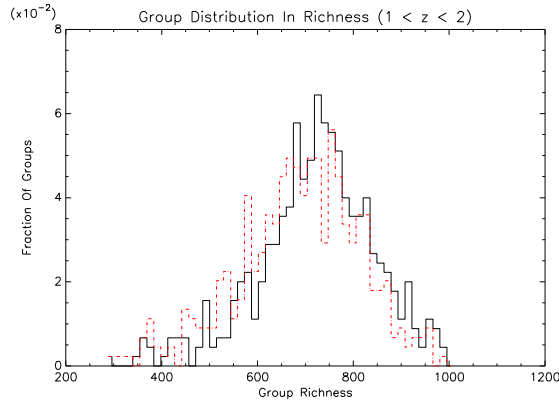


(a) *Group Richness Distribution.* The solid black line refers to the radio-optical sample, while the red dash-dot line to the control sample. The selection to $1 \leq z \leq 2$ has been applied, as well as the cut to apparent I-band magnitude 26.5. The number of galaxies in the sample is of 575.

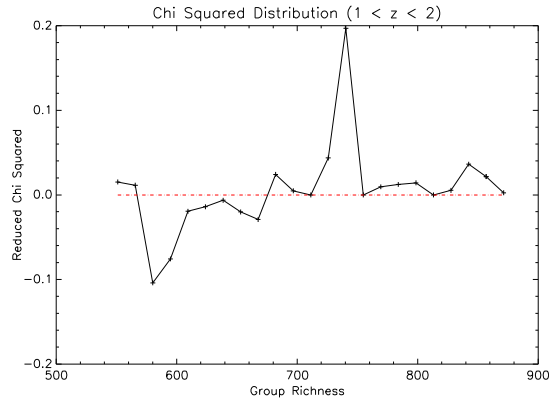


(b) *Reduced χ^2 Distribution.* The χ^2 test has been applied to the distributions above. The results are $\chi^2 = 41.59$ and $p = 0.11$, with a number of degrees of freedom of 32. A KS test has also been applied to the data and it results in a probability of 8×10^{-6} of the two distributions coming from the same parent population.

Figure 5.2: Redshift Dependent Coordinates, $1 \leq z \leq 2$, Apparent I-Band Magnitude Cut.

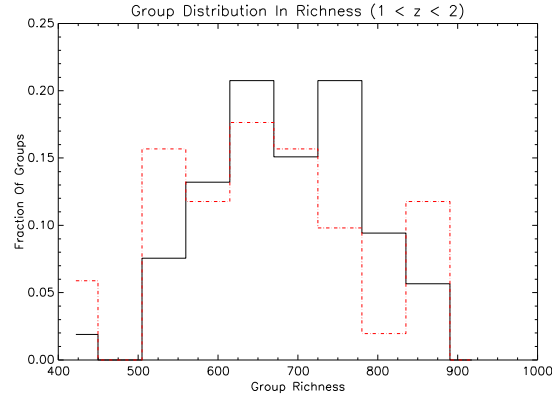


(a) *Group Richness Distribution.* The solid black line refers to the radio-optical sample, while the red dash-dot line to the control sample. The selection to $1 \leq z \leq 2$ has been applied, as well as the cut to apparent I-band magnitude 26.5 and the cuts to $\log(\frac{M^*}{M_\odot}) > 10$ and $\log(SSFR) > -11$. The number of galaxies in the sample is 450.

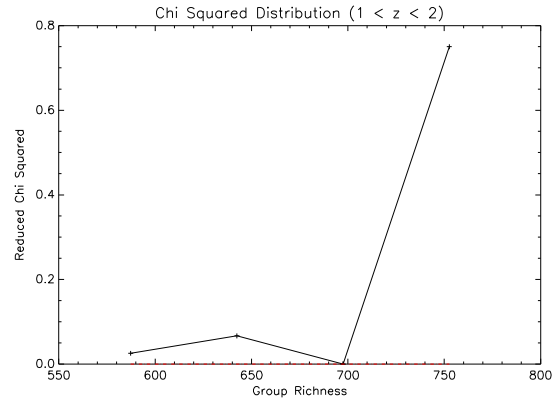


(b) *Reduced χ^2 Distribution.* The χ^2 test has been applied to the distributions above. The results are $\chi^2 = 14.67$ and $p = 0.88$, with a number of degrees of freedom of 22. A KS test applied to the data results in a probability of 5.7×10^{-5} of the two distributions coming from the same parent population.

Figure 5.3: Redshift Dependent Coordinates, $1 \leq z \leq 2$, Apparent I-Band Magnitude Cut, Stellar Mass And Specific Star Formation Cuts.

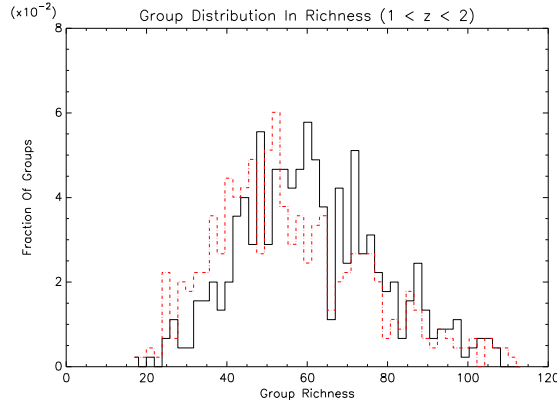


(a) *Group Richness Distribution.* The solid black line refers to the radio-optical sample, while the red dash-dot line to the control sample. The selection to $1 \leq z \leq 2$ has been applied, as well as the cut to apparent I-band magnitude 26.5 and the cuts to $\log(\frac{M^*}{M_\odot}) > 10$ and $\log(SSFR) < -11$. The number of galaxies in the sample is of 53.

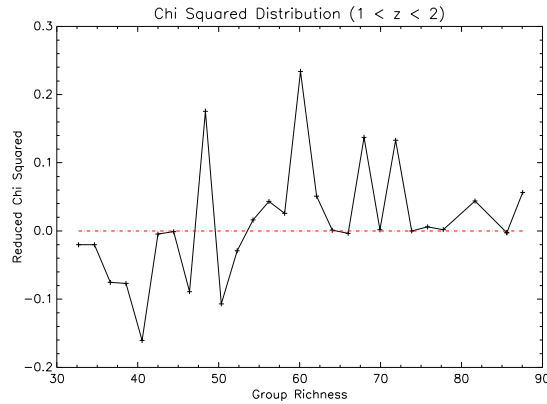


(b) *Reduced χ^2 Distribution.* The χ^2 test has been applied to the distributions above. The results are $\chi^2 = 2.52$ and $p = 0.47$, with a number of degrees of freedom of 3. A KS test has been applied to the data and results in a probability of 0.51 of the distributions coming from the same parent population.

Figure 5.4: Redshift Dependent Coordinates, $1 \leq z \leq 2$, Apparent I-Band Magnitude Cut, Stellar Mass And Specific Star Formation Cuts.



(a) *Group Richness Distribution.* The solid black line refers to the radio-optical sample, while the red dash-dot line to the control sample. The selection to $1 \leq z \leq 2$ has been applied, as well as the cut to apparent I-band magnitude 26.5 and the cuts to $\log(\frac{M^*}{M_\odot}) > 10$ and $\log(SSFR) > -11$, applied also to the optical sample.



(b) *Reduced χ^2 Distribution.* The χ^2 test has been applied to the distributions above. The results are $\chi^2 = 39.46$ and $p = 0.04$, with a number of degrees of freedom of 26. The KS test has been applied to the data and results in a probability of 4×10^{-7} of the two distributions coming from the same parent population.

Figure 5.5: Redshift Dependent Coordinates, $1 \leq z \leq 2$, Apparent I-Band Magnitude Cut, Stellar Mass And Specific Star Formation Cuts Applied Also To The Optical Sample.

a number of degrees of freedom of 26, a value above the tabulated one for a significance level down to 0.05. The KS test has been applied to the data and results in a probability of 4×10^{-7} of the two distributions coming from the same parent population.

The complementary sample is shown in figure 5.6.

Again the low number of counts makes a detailed analysis of the sample quite difficult. The distributions do not appear significantly different. The results of the χ^2 test are $\chi^2 = 3.00$ and $p = 0.39$, with a number of degrees of freedom of 3, a value never above the tabulated one for every significance level. The KS test has been applied to the data and results in a probability of 0.144 of the two distributions coming from the same parent population.

Results are summarized in table 5.1.

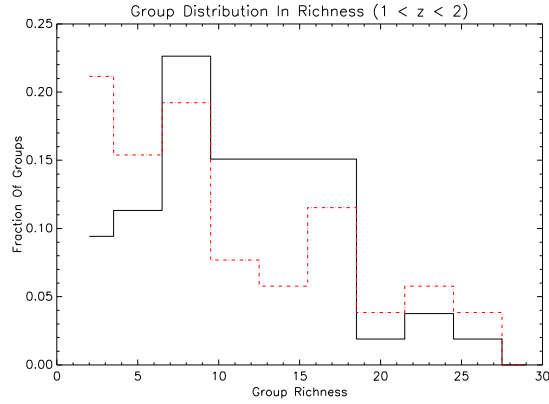
Type Of Sample	N_{RO}	N_C	p_{KS}
Total Sample	626	626	0.0013
$magI < 26.5$	575	575	8×10^{-6}
$\log(\frac{M^*}{M_\odot}) > 10$ And $\log(SSFR) < -11$	53	53	0.51
$\log(\frac{M^*}{M_\odot}) > 10$ And $\log(SSFR) > -11$	450	450	5.7×10^{-5}
$\log(\frac{M^*}{M_\odot}) > 10$ And $\log(SSFR) < -11$, Also To Optical Sample	53	53	0.144
$\log(\frac{M^*}{M_\odot}) > 10$ And $\log(SSFR) > -11$, Also To Optical Sample	450	450	4.0×10^{-7}

Table 5.1: The Study Of The Environment, Redshift Dependent Radius, Restriction To Redshift $1 \leq z \leq 2$.

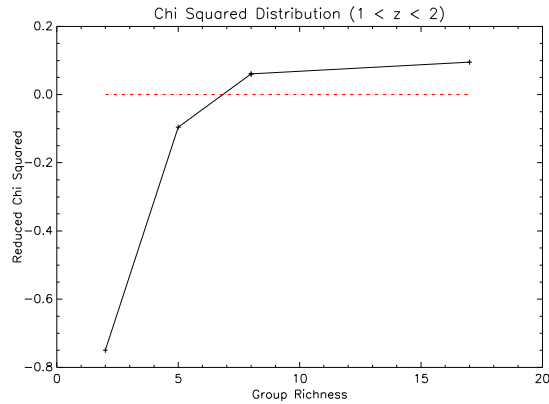
5.2 The Absolute Radio Luminosity Cut

A cut in absolute radio luminosity has been introduced in the data, creating two samples, based on the distinction on the radio power of the galaxies of the radio-optical sample.

According to the current theory of active galactic nuclei, two modes of accretion seem to be possible for a black hole at the center of a galaxy. As exposed for example in Hardcastle et al. (2007) and references therein, both hot and cold gas are a possible fuel for the accretion disk of an active galactic nucleus. While cold gas has a more violent way of accretion and a more powerful energy output, hot gas accretion results in a radiatively inefficient accretion flow. Therefore, hot gas accretion delivers a less energetic output to the surrounding medium. The difference in the two sources of gas for the accretion results in a few separations between the AGNs properties. First of all the power output will be different: in case of cold gas accretion the energy output will be greater than in the case of hot gas accretion. This translates in a different class of objects. In fact, recent studies show that low power and high power radio sources (namely Fanaroff-Riley class I and class II objects, Fanaroff & Riley (1974)) are actually AGNs accreting different kinds of gas, namely hot for low power radio sources and cold for high power radio sources. Moreover, it is expected that these kinds of objects inhabit different kinds of environments. In particular, low power FR I sources are expected to be found mostly in places rich in hot gas, like the hot, X-Ray emitting haloes of galaxy clusters. Otherwise, high power FR II objects



(a) *Group Richness Distribution.* The solid black line refers to the radio-optical sample, while the red dash-dot line to the control sample. The selection to $1 \leq z \leq 2$ has been applied, as well as the cut to apparent I-band magnitude 26.5 and the cuts to $\log(\frac{M^*}{M_\odot}) > 10$ and $\log(SSFR) < -11$, applied also to the optical sample.



(b) *Reduced χ^2 Distribution.* The χ^2 test has been applied to the distributions above. The results are $\chi^2 = 3.00$ and $p = 0.39$, with a number of degrees of freedom of 3. The KS test has been applied to the data and results in a probability of 0.144 of the two distributions coming from the same parent population.

Figure 5.6: Redshift Dependent Coordinates, $1 \leq z \leq 2$, Apparent I-Band Magnitude Cut, Stellar Mass And Specific Star Formation Cuts Applied Also To The Optical Sample.

should be found preferentially in environments with large amounts of cold gas, like in systems which have recently undergone a wet merger.

From these assumptions it is expected to find differences in the environment around high power radio galaxies and around low power ones. Therefore a cut on the radio-optical sample has been performed, in order to check the presence of an effect of such kind in the data.

The environment has been studied around two different samples. In particular the radio-optical sample has been divided into a low power sample, with $24 \leq \log(\frac{L_{1.4GHz}}{W/Hz}) \leq 24.5$ and a high power one with $\log(\frac{L_{1.4GHz}}{W/Hz}) > 24.5$. In addition, the usual cut in apparent I-band magnitude to 26.5 and the restriction to redshift $1 \leq z \leq 2$ have been applied. The number of galaxies in each sample are 419 and 298, respectively for the low and high power samples. The distinction between the two samples has been set to $\log(\frac{L_{1.4GHz}}{W/Hz}) = 24.5$ since it is this value that it is assumed to divide radiogalaxies into class I and class II objects (see Fanaroff & Riley (1974)).

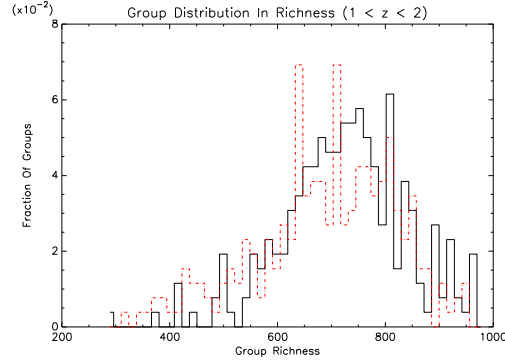
The first panel in figure 5.7 shows the group richness distributions for the samples with the cuts to $24 \leq \log(\frac{L_{1.4GHz}}{W/Hz}) \leq 24.5$, $1 \leq z \leq 2$ and to apparent I-band magnitude lower than 26.5. The solid black line refers to the radio-optical sample, while the dot-dashed red line refers to the control sample. The two distributions are similar, with a wide peak for groups with a number of elements between 650 and 850. In the second panel of the same figure, the reduced χ^2 distribution is showed. The results of the χ^2 test performed on the distributions of the panel above are $\chi^2 = 13.62$ and $p = 0.75$, the χ^2 value is always below the tabulated values for every significativity level and for a number of degrees of freedom of 18. A deep valley and a straight peak can be recognized respectively at 640 and 700 values. A KS test has been performed too, yielding a probability of 0.86 of the distributions coming from the same parent population.

The same analysis has been performed also on the high power samples, namely the one with the cuts to $\log(\frac{L_{1.4GHz}}{W/Hz}) > 24.5$, $1 \leq z \leq 2$, and to apparent I-band magnitude lower than 26.5. The results are showed in figure 5.8.

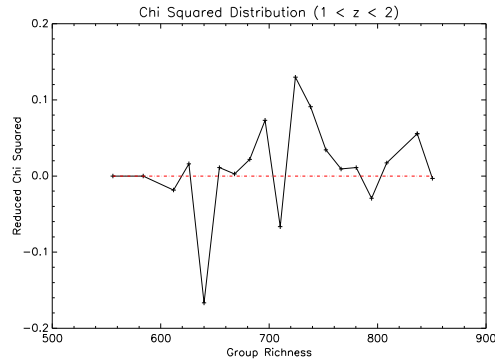
The first panel of figure 5.8 shows the group richness distributions for the radio-optical sample (solid black line) and for the control sample (red dash-dotted line). The two distributions are quite similar and this similarity is confirmed by the results of the reduced χ^2 test performed on the distributions. The test results in $\chi^2 = 2.1$ and $p = 0.91$, a value always below the tabulated values for every significativity level for a number of degrees of freedom of 6. A KS test results in $p = 0.88$ of the two distributions coming from the same parent population. Nevertheless, a comparison between these values and the ones in the previous case shows that the differences between the distributions in the low power samples are more significant than those in the high power case. Therefore, it can be concluded that low power radiogalaxies tend to be found more often in clusters, compared to high power radiogalaxies. This adds an observational evidence to the thesis exposed in Hopkins et al. (2008b) and in Croton et al. (2006), which would see low power AGNs, accreting hot gas from the X-Ray emitting halo of galaxy groups as a more probable quenching mechanism in high mass systems.

Further cuts have been implemented on the samples, namely those in specific star formation rate and stellar mass as explained in chapter 4, section 4.3.2.

First panel of figure 5.9 shows the group richness distributions for the radio-

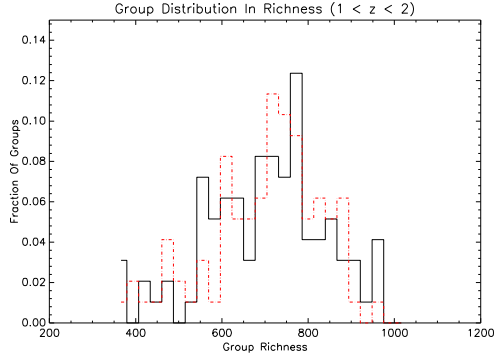


(a) *Group Richness Distribution.* The black solid line refers to the radio-optical sample, while the red dash-dot line to the control sample. The total number of galaxies in the sample is of 419.

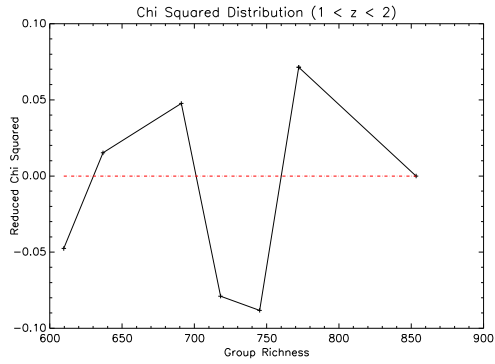


(b) χ^2 *Distribution.* The χ^2 test has been applied to the two distributions above. The test results in $\chi^2 = 13.62$ and $p = 0.75$, with a number of degrees of freedom of 18. A KS test results in $p = 0.86$ of the two distributions coming from the same parent population.

Figure 5.7: Environment Of Low Power Radio Sources. The cut to $24 \leq \log(\frac{L_{1.4GHz}}{W/Hz}) \leq 24.5$ has been applied, together with the restriction to $1 \leq z \leq 2$ and the apparent I-band magnitude cut to 26.5.

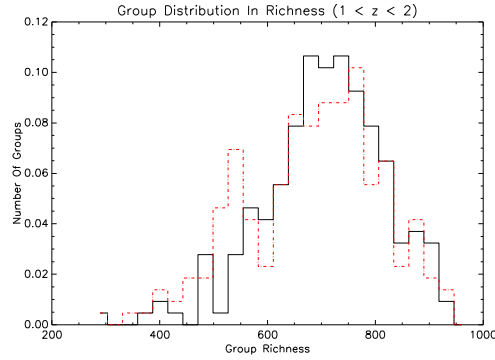


(a) *Group Richness Distribution.* The black solid line refers to the radio-optical sample, while the red dash-dot line to the control sample. The total number of galaxies in the sample is of 298.

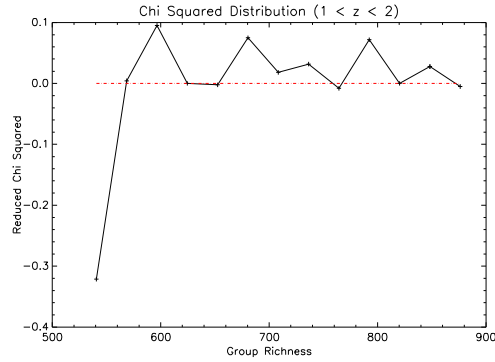


(b) χ^2 *Distribution.* The χ^2 test has been applied to the two distributions above. The test results in $\chi^2 = 2.1$ and $p = 0.91$, with a number of degrees of freedom of 6. A KS test results in $p = 0.88$ of the two distributions coming from the same parent population.

Figure 5.8: Environment Of High Power Radio Sources. The cut to $\log(\frac{L_{1.4GHz}}{W/Hz}) > 24.5$ has been applied, together with the restriction to $1 \leq z \leq 2$ and the apparent I-band magnitude cut to 26.5.



(a) *Group Richness Distribution.* The black solid line refers to the radio-optical sample, while the red dash-dot line to the control sample. The total number of galaxies in the sample is of 318.



(b) χ^2 *Distribution.* The χ^2 test has been applied to the two distributions above. The test results in $\chi^2 = 7.93$ and $p = 0.79$, with a number of degrees of freedom of 12. A KS test results in $p = 0.048$ of the two distributions coming from the same parent population.

Figure 5.9: Environment Of Low Power Radio Sources. The cut to $24 \leq \log(\frac{L_{1.4GHz}}{W/Hz}) \leq 24.5$ has been applied, together with the restriction to $1 \leq z \leq 2$, the apparent I-band magnitude cut to 26.5 and the cuts to $\log(\frac{M^*}{M_\odot}) > 10$ and $\log(SSFR) > -11$.

optical sample (solid black line) and for the control sample (red dot-dashed line) with the cuts to $24 \leq \log(\frac{L_{1.4GHz}}{W/Hz}) \leq 24.5$, $1 \leq z \leq 2$, apparent I-band magnitude lower than 26.5 and the cuts to $\log(\frac{M^*}{M_\odot}) > 10$ and $\log(SSFR) > -11$. The two distributions are almost similar, with a peak around groups with a number of elements of 700 units. A χ^2 test has been performed on them and results in $\chi^2 = 7.93$ and $p = 0.79$, a value always below the tabulated values for every significance level, for a number of degrees of freedom of 12. A Kolmogorov-Smirnoff test results in $p = 0.048$ of the two distributions coming from the same parent population. The reduced χ^2 distribution is showed in the second panel of the same figure. The distribution is quite regular, with no significant features.

The same analysis has been performed on the high power sample with the same cuts as the low power one. The results are shown in figure 5.10.

The first panel shows the group richness distributions for the radio-optical sample (solid black line) and the control sample (red dot-dash line). Although similar in shape, the two distributions are shifted from each other, with the groups around the galaxies from the control sample being less numerous. A reduced χ^2 test has been performed on the distributions and results in $\chi^2 = 1.10$ and $p = 0.58$, a value always below the tabulated values for every significance level, for a number of degrees of freedom of 2. A KS test results in $p = 0.21$ of the two distributions coming from the same parent population. The second panel shows the reduced χ^2 distribution, although the statistics is quite low. Again, as in the previous case, it can be seen that the low power sample have a higher significance in the difference between the radio-optical and control sample. Therefore the results are stronger for the groups around the low power radiogalaxies.

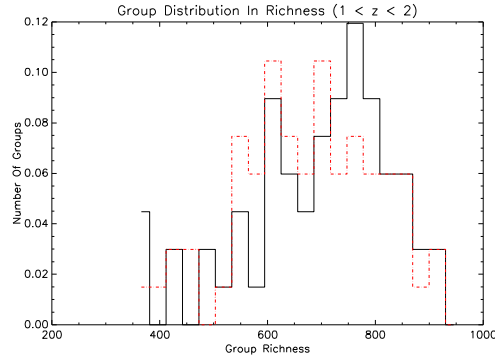
The first panel of figure 5.11 shows the group richness distributions for the radio-optical sample (solid black line) and for the control sample (red dot-dashed line) for the low power sample, with the cuts to $24 \leq \log(\frac{L_{1.4GHz}}{W/Hz}) \leq 24.5$, $1 \leq z \leq 2$, apparent I-band magnitude lower than 26.5 and the cuts to $\log(\frac{M^*}{M_\odot}) > 10$ and $\log(SSFR) < -11$, therefore complementary to the case analyzed above.

The statistic is again really low, but a χ^2 test performed on the distributions results in $\chi^2 = 0.33$ and $p = 0.56$, a value always below the tabulated ones for every significance level and for only one degree of freedom. A KS test results in $p = 0.08$ of the two distributions coming from the same parent population. The reduced χ^2 distribution is showed in the second panel of the same figure.

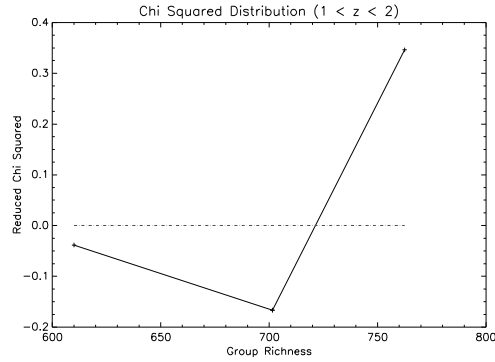
Figure 5.12 shows the same results for the high power sample, with the cuts to $\log(\frac{L_{1.4GHz}}{W/Hz}) > 24.5$, $1 \leq z \leq 2$, apparent I-band magnitude lower than 26.5 and the cuts to $\log(\frac{M^*}{M_\odot}) > 10$ and $\log(SSFR) < -11$.

Although the statistic is very low, the first panel of figure 5.12 shows the group richness distributions for the radio-optical sample (solid black line) and for the control sample (red dot-dashed line). A χ^2 test has been performed on the data, with the results $\chi^2 = 0.09$ and $p = 0.76$, a value always below the tabulated ones for every significance level for only one degree of freedom. A KS test results in $p = 0.74$ of the two distributions coming from the same parent population. The reduced χ^2 distribution is showed in the second panel of the same figure.

Results are summarized in table 5.2.

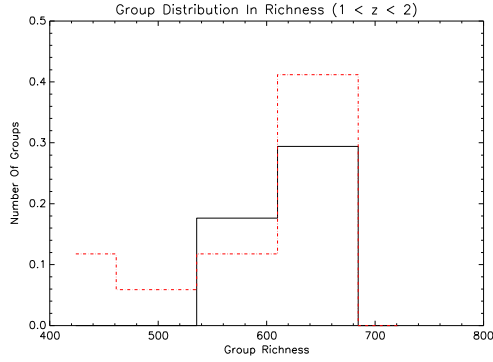


(a) *Group Richness Distribution.* The black solid line refers to the radio-optical sample, while the red dash-dot line to the control sample. The total number of galaxies in the sample is of 218.

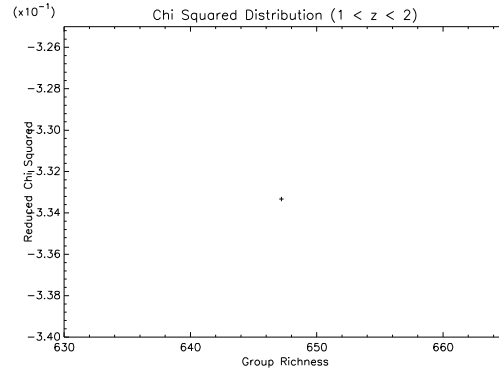


(b) χ^2 *Distribution.* The χ^2 test has been applied to the two distributions above. The test results in $\chi^2 = 1.10$ and $p = 0.58$, with a number of degrees of freedom of 2. A KS test results in $p = 0.21$ of the two distributions coming from the same parent population.

Figure 5.10: Environment Of High Power Radio Sources. The cut to $\log(\frac{L_{1.4GHz}}{W/Hz}) > 24.5$ has been applied, together with the restriction to $1 \leq z \leq 2$, the apparent I-band magnitude cut to 26.5 and the cuts to $\log(\frac{M^*}{M_\odot}) > 10$ and $\log(SSFR) > -11$.

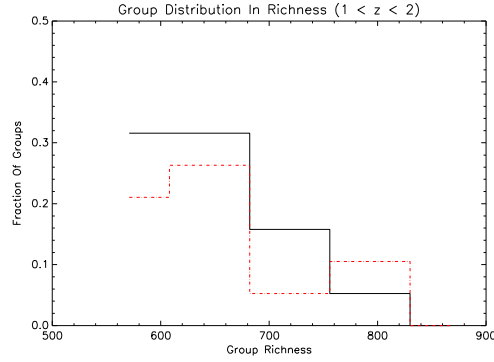


(a) *Group Richness Distribution.* The black solid line refers to the radio-optical sample, while the red dash-dot line to the control sample. The total number of galaxies in the sample is of 63.

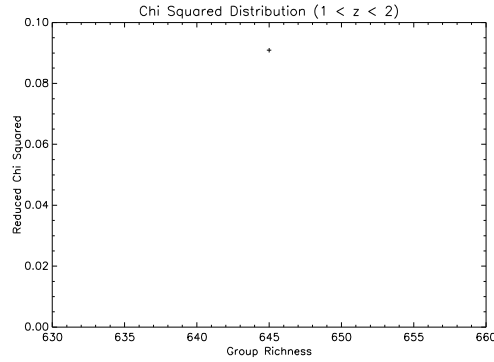


(b) χ^2 *Distribution.* The χ^2 test has been applied to the two distributions above. The test results in $\chi^2 = 0.33$ and $p = 0.56$, with only one degree of freedom. A KS test results in $p = 0.08$ of the two distributions coming from the same parent population.

Figure 5.11: Environment Of Low Power Radio Sources. The cut to $24 \leq \log(\frac{L_{1.4GHz}}{W/Hz}) \leq 24.5$ has been applied, together with the restriction to $1 \leq z \leq 2$, the apparent I-band magnitude cut to 26.5 and the cuts to $\log(\frac{M^*}{M_\odot}) > 10$ and $\log(SSFR) < -11$.



(a) *Group Richness Distribution.* The black solid line refers to the radio-optical sample, while the red dash-dot line to the control sample. The total number of galaxies in the sample is of 45.



(b) χ^2 *Distribution.* The χ^2 test has been applied to the two distributions above. The test results in $\chi^2 = 0.09$ and $p = 0.76$, with only one degree of freedom. A KS test results in $p = 0.74$ of the two distributions coming from the same parent population.

Figure 5.12: Environment Of High Power Radio Sources. The cut to $\log(\frac{L_{1.4GHz}}{W/Hz}) > 24.5$ has been applied, together with the restriction to $1 \leq z \leq 2$, the apparent I-band magnitude cut to 26.5 and the cuts to $\log(\frac{M^*}{M_\odot}) > 10$ and $\log(SSFR) < -11$.

Type Of Sample	N_{RO}	N_C	p_{KS}
$magI < 26.5$, Low Power	419	419	0.86
$magI < 26.5$, High Power	298	298	0.88
$\log(\frac{M^*}{M_\odot}) > 10$ And $\log(SSFR) < -11$, Low Power	63	63	0.08
$\log(\frac{M^*}{M_\odot}) > 10$ And $\log(SSFR) < -11$, High Power	45	45	0.74
$\log(\frac{M^*}{M_\odot}) > 10$ And $\log(SSFR) > -11$, Low Power	318	318	0.048
$\log(\frac{M^*}{M_\odot}) > 10$ And $\log(SSFR) > -11$, High Power	218	218	0.21

Table 5.2: The Study Of The Environment, Absolute Radio Luminosity Selection, $1 \leq z \leq 2$.

5.3 Conclusions

In this chapter a restriction to the redshift interval $1 \leq z \leq 2$ has been applied to the data and the study of the environment has been performed as before. This has been done in order to better compare the results with other works done on the argument and to check the consistency of the galaxy formation paradigm. Results are summarized in table 5.1.

A further distinction in the absolute luminosity at 1.4 GHz has been operated on the samples. The aim is to separate the radio-optical sample into Fanaroff-Riley class I and class II objects, namely low radio power and high radio power sources. The determination of differences in the environment around the two kinds of radiogalaxies can help solve the dichotomy between the formation mechanisms of low power radio galaxies (composed of a black hole with a radiatively inefficient accretion flow of hot gas) and the high power ones (with a highly emitting accretion disk composed of cold gas). It is found that the low power radio sources, tend to stay in more significant overdensities compared to the high power ones. This is in agreement with the current picture of galaxy formation and evolution. A summary is given in table 5.2.

Chapter 6

Conclusions

THIS work of thesis has consisted in the study of the environment, on the scale typical of galaxy clusters, around the galaxies of a sample extracted from the VLA-COSMOS survey. Around every galaxy from the radio-optical sample, it has been searched in a sphere of radius 1 Mpc for possible companions, therefore mapping the presence of protogroups in the area covered by the COSMOS survey. In order to check the consistency of the results, a control sample with the same properties of the radio-optical sample has been created. This has been accomplished by extracting randomly from the optical sample a number of galaxies with the same properties as the radio-optical one. The two samples have been compared, in order to assess the properties of the environment around radiogalaxies.

This chapter is structured as it follows: in section 6.1 the main results of the study of the environment are presented, in section 6.2 the restriction to $1 \leq z \leq 2$ is discussed. In section 6.3 the analysis based on the distinction between high power and low power radio sources is exposed, while in section 6.4 a comparison with previous works on the same topic is performed. A summary is given in section 6.5.

6.1 The Properties Of The Environment Around Radiogalaxies

The properties of the environment around radiogalaxies have been studied in different ways and for different subsamples, in order to check for different trends and properties of various kinds of radio and optical galaxies.

6.1.1 Fixed Distance

A first assumption, in order to simplify the calculations, it is to ignore the dependence from redshift of the angular distance corresponding to a physical distance of 1 Mpc. Therefore, this angular distance is considered to be, in first approximation, that corresponding to 1 Mpc at a redshift $z = 1.5$. The group richness distributions have been derived both for the total sample and for a

cut to apparent I-band magnitude lower than 26.5, in order to account for the completeness limit. Both the distributions (according to the χ^2 test and the Kolmogorov-Smirnoff test performed, see figures 4.1 and 4.2) are significantly different from the control sample. The second panels of figures 4.1 and 4.2 show clearly that this difference in the environment gets explicit in the sense that groups around radiogalaxies tend to be more rich than those around normal galaxies. The distributions of the radio-optical sample in both cases (solid black lines in the first panels of figures 4.1 and 4.2) are systematically shifted to the right of the plot, towards higher values of richness. This effect can be seen also in the second panels of both figures, since the reduced χ^2 distribution is below zero in the first part of the plot and above zero in the second. Therefore, groups around radiogalaxies (both in the total sample and in the one cut to apparent I-band magnitude 26.5) are systematically more rich than those around normal galaxies. This effect is significant, as it holds even increasing to 100 the number of random extractions of the control sample, as depicted by figures 4.13 and 4.14. These two figures both show that the distributions of value of reduced χ^2 is above the tabulated one in the majority of extractions, therefore making the results significative.

Subsequently a cut in stellar mass and specific star formation rate has been applied. This cut has been realized in order to distinguish the radiogalaxies based on their evolutionary status and activity. In fact, from the theory of galaxy formation and evolution, it is known that most galaxies have undergone a phase of intense star formation in the past, and that this phase is associated to (and then quenched by) AGN activity. In chapter 3, section 3.3.3, the characteristics of stellar mass and specific star formation rate of the samples have been discussed and analyzed, with respect to redshift. It is then operated a cut on the radio-optical sample in stellar mass and star formation, in order to define two subsamples corresponding to different degrees of activity and starburst. Only galaxies with $\log(\frac{M^*}{M_\odot}) > 10$ has been considered. This allows to concentrate both on galaxies which are still forming stars, and on the part of the sample which has already reached a high mass and has quenched the star formation. Then, a separation in specific star formation rate is placed to $\log(SSFR) = -11$. This way, galaxies that are more actively star forming are divided from those that are only passively evolving. This distinction allows also to isolate those radio sources for which the radio emission originates purely from AGN activity. In fact, selecting radio sources which present a low degree of star formation allows to eliminate from the sample those sources for which the radio emission is due both from AGN and from starburst activity. The group richness distributions for both samples are showed in figures 4.3 and 4.4 and, although they seem different and seem to show the same effect depicted for the total and the apparent I-band magnitude cut sample in the paragraphs above, no solid results can be stated, since these differences are found to be not significant, as showed by figures 4.15 and 4.16. Nevertheless, although the reduced χ^2 test seems to exclude the significativity of the results, the Kolmogorov-Smirnoff test gives another perspective on the properties of the groups around radiogalaxies. In fact, the probability of the group richness distributions for the radio-optical sample and for the control sample of being drawn from the same parent population is two orders of magnitude lower in the $\log(SSFR) < -11$ case (4.4×10^{-8}) than in the $\log(SSFR) > -11$ (6.6×10^{-6}). Therefore, low starforming, passively

evolving galaxies whose radio emission is dominated by AGN phenomena tend to be at the center of richer groups than galaxies that are still forming stars.

The exact same cut has been operated on the optical sample. The galaxies of this sample are the ones which are searched around the radiogalaxies, therefore they are the population of the groups found around the radiogalaxies. The aim of this operation is to check whether groups are composed preferentially of galaxies with the same properties. In fact, it is possible that star forming optical galaxies tend to group preferentially around radiogalaxies with the same degree of star formation and activity. On the contrary passively evolving galaxies could tend to group around radiogalaxies which have already quenched star formation. This effect could be explained, for example, if it were assumed that quenching of star formation happens in all the group members at the same time due to some large scale environmental effect. Results are showed in figures 4.5 and 4.6. Both the distributions corresponding to the radio-optical sample (solid black lines in the first panel of both figures) are different from the corresponding control samples. This difference is significative as demonstrated also by the comparison with the 100 random extractions (see figures 4.18 and 4.17 for the reduced χ^2 value distributions). The distributions are different, as again groups are more rich around radiogalaxies than around normal ones. This excess of clustering is found in the same measure around galaxies of every level of star formation.

6.1.2 Redshift Dependence

The method for the research of protogroups has been refined, by introducing the dependence of the research from redshift, integrating the equations of cosmology. This introduces a greater accuracy in the determination of the groups richness, taking into account the redshift distribution of the samples, discussed in chapter 3, section 3.2.3. The analysis performed is the same as before, all the cuts have been maintained.

The first two cases analyzed, namely the general case and the sample with the cut to apparent I-band magnitude lower than 26.5, are described in figures 4.7 and 4.8. Both the distributions corresponding to the radio-optical sample (solid black lines) are significantly different from the ones corresponding to the control sample (red dot-dash lines). This difference is convalidated by the check of the significativity with the set of 100 extractions (see figures 4.19 and 4.20). The distributions reproduce the effect described above, *i.e.* of the distributions corresponding to the radio-optical sample being shifted towards higher richnesses. Therefore, the introduction of a higher accuracy confirms the general trend: groups around radiogalaxies are more numerous than those around normal galaxies.

The distinction based on the level of star formation activity has been introduced, in order to check for the effect as said before. Again the samples have first been cut to $\log(\frac{M^*}{M_\odot}) > 10$, then they have been divided on the base of their star formation, the division being at $\log(SSFR) = -11$. Results are shown in figures 4.9 and 4.10. The distributions seem to have the same effect depicted before, with the group richness distributions of the galaxies from the radio-optical sample being shifted towards the right of the plot, to higher richnesses. Unfortunately these results cannot be considered significant, according to the χ^2 test applied to the data, as showed by figures 4.21 and 4.22, which refer to the set of 100 random extractions. Nevertheless, the Kolmogorov-Smirnoff test

applied to the data gives a probability of the two distributions (radio-optical sample and control sample) coming from the same parent population different by three orders of magnitude between the $\log(SSFR) < -11$ case (1.56×10^{-8}), and the $\log(SSFR) > -11$ case (1.5×10^{-11}), in contrast to what found in the less accurate, fixed distance case. Therefore higher star forming galaxies tend to be at the center of richer groups.

The same situation is found also for the distributions showed in figures 4.12 and 4.11. These plots depict the situation that has already been investigated in the case of fixed distance, *i.e.* if galaxies with defined stellar mass and star formation properties tend to group around radiogalaxies with the same characteristics. To do this, the stellar mass selection and the specific star formation rate distinction already operated on the radio-optical sample have been applied also to the optical sample. The distributions again appear shifted to the right of the plot, with the solid black lines (corresponding to the radio-optical sample) covering a range of higher richnesses. Although again results cannot be considered significative according to the χ^2 test applied to the data (see figures 4.23 and 4.24), the Kolmogorov-Smirnoff test performed results in a probability of the two distributions (radio-optical sample and control sample) coming from the same parent population twelve orders of magnitude lower in the case with $\log(SSFR) < -11$ (9.19×10^{-19}) than in the case with $\log(SSFR) > -11$ (1.0×10^{-7}). Therefore groups around radiogalaxies that present a lower degree of star formation activity, which are formed by normal galaxies with the same level of low star formation as the central radiogalaxy tend to be more numerous than groups around galaxies extracted randomly.

6.2 The Restriction To $1 \leq z \leq 2$

A restriction of the data to a limited redshift interval has been made. In particular, only radiogalaxies with $1 \leq z \leq 2$ have been selected and the group richness distributions have been derived for the selection. The same cuts as before have been applied.

This restriction has been made because several works have been done on the search for protoclusters around radiogalaxies in this same redshift interval, with various methods used to identify the protocluster members. A review of the results made in the last few decades may be found in section 7 of Miley & De Breuck (2008).

Another, more physical, reason for the restriction to the redshift range $z \in [1; 2]$ is the fact that the maximum of the cosmic star formation history of the Universe is reached in that redshift interval. In fact, Soifer et al. (2008) has calculated the star formation history of the entire Universe, using IR luminosity of galaxies. This so-called Cosmic Star Formation History (CSFH, see figure 1.4) is found to increase dramatically between $0 \leq z \leq 1$ and to maintain a stable high value in the interval $1 \leq z \leq 2$. After $z = 2$, data become more uncertain but a decrease in CSFH seems inevitable. Therefore, the bulk of the star formation history of the Universe is realized in the interval $z \in [1; 2]$. If it is assumed, as in this work, that star formation is intrinsically related to AGN activity and radio emission, then the study of the environment of radiogalaxies in this redshift selection could give more insights and better understanding of the problem of galaxy formation and evolution.

Results are showed in figures 5.1 and following. The group richness distributions show the general trend described in the previous sections, with the group richness distributions for the radio-optical sample (solid black line) shifted towards higher group richnesses than the control sample (red dot-dashed line). Although the statistic is worse than the previous cases, due to the lower number of counts than in the previous samples, this is more evident in figure 5.5, which refers to the sample with $\log(\frac{M^*}{M_\odot}) > 10$ and $\log(SSFR) > -11$, with the same cuts applied also to the optical sample. This case is the only one for which the χ^2 test results in a significative difference between the two distributions. Nevertheless the probabilities given by the Kolmogorov-Smirnoff test applied to all the distributions are always quite low, meaning that it is unlikely that the group richness distributions for the radio-optical sample and for the control sample come from the same parent population. Moreover these probability seem always to indicate a higher level of clustering for the samples with $\log(SSFR) > -11$ compared to the complementary ones. In fact they have lower values, implying a higher difference between the distributions. A summary of the results may be found in table 5.1.

6.3 The Distinction Between Low Power And High Power Radio Sources

Another investigation which is important to make, in order to better situate the results into the current picture of galaxy formation and evolution, is the distinction of the radio-optical sample into the various classes of AGN types, namely a division based on absolute luminosity at 1.4 GHz, of the radio-optical sample into Fanaroff-Riley Class I and Class II objects (Fanaroff & Riley, 1974). This has been achieved with a cut in total radio luminosity at $\log(\frac{L_{1.4GHz}}{W/Hz}) = 24.5$. Therefore two subsamples have been created, one with $\log(\frac{L_{1.4GHz}}{W/Hz}) > 24.5$ and one with $24 \leq \log(\frac{L_{1.4GHz}}{W/Hz}) \leq 24.5$. A restriction in redshift has also been applied, selecting only sources with $1 \leq z \leq 2$.

Figures 5.7 and following show the group richness distributions for the radio-optical sample with the following cuts: the apparent I-band magnitude cut at 26.5, the $\log(\frac{M^*}{M_\odot}) > 10$ cut and the $\log(SSFR) = -11$ distinction. The group richness distributions for the corresponding control samples are also shown. Every subsample is then further restricted to $1 \leq z \leq 2$ and divided into high power radio sources ($\log(\frac{L_{1.4GHz}}{W/Hz}) > 24.5$) and low power radio sources ($24 \leq \log(\frac{L_{1.4GHz}}{W/Hz}) \leq 24.5$). Although the statistic is quite reduced, the distributions of the radio-optical sample appear to differ from those of the control sample. This difference is remarked by the Kolmogorov-Smirnoff test, which has been applied to the data, and whose values are resumed in table 5.2. The general trend is that the probability of the two distributions (radio-optical and control sample) of coming from the same parent population is always lower in the low power case than in the high power one. This is important since it adds observational evidence to the assumption that low power radio sources are more easily found in richer groups and more massive environments. This is due to the fact that richer clusters have too high velocity dispersions at their centers to successfully trigger wet merger events, therefore hot gas accretion is required to power AGNs. Hot

gas accretion is responsible for radiatively inefficient accretion flows, therefore resulting quasars will be low power sources. Finding low power radiogalaxies in more dense environments observationally empowers this fact.

6.4 Comparison With Previous Works

The search for clusters of galaxies is a quest which has fascinated astronomers ever since the first hypotheses on the formation and evolution of structures. Being the greatest structures in the Universe, formed by gas, galaxies and dark matter, galaxy clusters are the places where modern galaxies are found and are thought to have lived from their first formation. The formation and evolution of galaxies is thought to be entangled with that of the environment they live in. Including this in a much wider picture, in which also the AGN phenomena play a role (see chapter 1), gives rise to the idea that high redshift protoclusters should be found more frequently around radiogalaxies, or that clusters of galaxies found around radiogalaxies ought to be more rich than those around normal, non-radio emitting ones. This should be particularly true when looking for clusters of galaxies at high redshift, when the Universe was younger and the structures were just starting to form.

A lot of work has been done on this topic in the past few decades. Various methods have been developed, in order to search for overdensities or protoclusters of galaxies at high redshift. In general it can be stated the presence of a good agreement between the various results. The present work of thesis is also in good agreement with what found so far.

In particular the COSMOS survey, from which the data sample for this work has been extracted (see chapter 2) has been widely used to search the environment of radiogalaxies for clusters and groups, both for the deep redshifts reached (photometric and spectroscopic, as in the zCOSMOS survey), the large wavelength coverage (which spans from X-Rays to radio) and for the large number of galaxies, which allow for large statistic.

As an example, a good agreement is found between this work and the one by Chiaberge et al. (2010). They studied the environment around five radiogalaxies in the COSMOS field and found clusters around three of them. In particular the three candidate clusters were all found around Fanaroff-Riley class I objects in the redshift range $1 \leq z \leq 2$. A comparison between these radiogalaxies and a sample of more powerful Fanaroff-Riley class II objects and field samples showed that it is more likely to find clusters around low power FR I. This is in perfect agreement with the results of this thesis, exposed in section 6.3. This is nevertheless in opposition to what found by Wylezalek et al. (2013). Using infrared data, the group looked for overdensities around known radio sources in the redshift range $1.2 < z < 3.2$. The results did not show any difference between low power and high power radio sources. Still, the work generally confirmed the results of this thesis, since the groups found around radiogalaxies were found to be always significantly richer than those around their control samples. This same results are found also by Bardelli et al. (2010) and Diener et al. (2013), which found clusters and overdensities around radiogalaxies in the zCOSMOS spectroscopic redshift survey. In particular Bardelli et al. (2010) found that the more clustered radiogalaxies are those with a lower specific star formation rate ($\log(SSFR) < -11$; a $\log(\frac{M^*}{M_\odot}) > 10.7$ cut has also been applied

to the data). This is in agreement with what found for the case showed in figure 4.3, for this work for similar cuts in stellar mass and specific star formation rate. An analogous result of the one found by Diener et al. (2013) is found by Durret et al. (2011), which created a sample of clusters around radiogalaxies, using data from the Canada-France-Hawaii Telescope Legacy Survey (CFHTLS).

A lot of work has been done also using an estimate of the environment based on the search for Lyman α and H α emitters around radio emitting galaxies, whose redshift have been determined in a secure way, as with spectroscopic surveys. This is achieved, for example, by Venemans et al. (2007) and by Kodama et al. (2007). Both of these works find clusters and overdensities of galaxies around radio sources, showing good agreement with previous results and this work. A review of the results found with this method can be found in section 7 of Miley & De Breuck (2008).

On the contrary, Silverman et al. (2009) found opposite results. Analyzing a sample of galaxies from the zCOSMOS survey, the group found that AGNs reside in environments with all kind of densities, from field to clusters. This was understood by looking at the fraction of galaxies hosting an Active Galactic Nucleus in the various kind of environments, which were found to be comaprable. Although this result seems to be negating what found in this work, it is to be kept in mind that in the present work of thesis it has been assumed that the only galaxies with radio emission are those at the center of the cluster, while other cluster members are thought to be normal optical galaxies. Therefore, while no assumptions on the AGN fractions in the VLA-COSMOS selected clusters can be made on the basis of the results of this work, it would be intersting to derive the fractions of active galactic nuclei in the cluster members, in order to better compare with the work of Silverman et al. (2009)

6.5 Summary

This work of thesis has used data from the COSMOS survey and its part at radio wavelengths (VLA-COSMOS) in order to asses the environment around radio sources. The environment has been determined by counting all galaxies on a scale of 1 Mpc around every radio source. Results may be synthesized in the following key-points:

1. The environment around radiogalaxies is significantly more rich than the one around normal ones.
2. The results hold independently from redshift, stellar mass and specific star formation rate selections in galaxies where the radio emission comes from AGN activity.
3. The distinction in richness of the environment around radiogalaxies as compared to the environment around normal ones is more significant for low power FR I radiogalaxies than for high power FR II objects.

Although the results reached from this work are promising, more work on the topic is ausplicable. For example, the study of the environment could be performed also on X-Ray selected sources. The creation of a complete catalogue of clusters in the COSMOS field, with radio, optical and X-Ray data could provide color-magnitude diagrams, mass and luminosity functions to be compared

with theoretical and semi-analytical models of galaxy formation, as well as a more complete determination of the properties of the environment around active galactic nuclei. It is hoped that these results help to better understand the processes which lie at the base of the formation and the evolution of structures in the Universe.

Appendix A

χ^2 Distribution Table

A table of the χ^2 distribution for up to 100 degrees of freedom (columns) and for significance levels down to 0.005 (rows) is given.

df	0.995	0.99	0.975	0.95	0.90	0.10	0.05	0.025	0.01	0.005
1	---	---	0.001	0.004	0.016	2.706	3.841	5.024	6.635	7.879
2	0.010	0.020	0.051	0.103	0.211	4.605	5.991	7.378	9.210	10.597
3	0.072	0.115	0.216	0.352	0.584	6.251	7.815	9.348	11.345	12.838
4	0.207	0.297	0.484	0.711	1.064	7.779	9.488	11.143	13.277	14.860
5	0.412	0.554	0.831	1.145	1.610	9.236	11.070	12.833	15.086	16.750
6	0.676	0.872	1.237	1.635	2.204	10.645	12.592	14.449	16.812	18.548
7	0.989	1.239	1.690	2.167	2.833	12.017	14.067	16.013	18.475	20.278
8	1.344	1.646	2.180	2.733	3.490	13.362	15.507	17.535	20.090	21.955
9	1.735	2.088	2.700	3.325	4.168	14.684	16.919	19.023	21.666	23.589
10	2.156	2.558	3.247	3.940	4.865	15.987	18.307	20.483	23.209	25.188
11	2.603	3.053	3.816	4.575	5.578	17.275	19.675	21.920	24.725	26.757
12	3.074	3.571	4.404	5.226	6.304	18.549	21.026	23.337	26.217	28.300
13	3.565	4.107	5.009	5.892	7.042	19.812	22.362	24.736	27.688	29.819
14	4.075	4.660	5.629	6.571	7.790	21.064	23.685	26.119	29.141	31.319
15	4.601	5.229	6.262	7.261	8.547	22.307	24.996	27.488	30.578	32.801
16	5.142	5.812	6.908	7.962	9.312	23.542	26.296	28.845	32.000	34.267
17	5.697	6.408	7.564	8.672	10.085	24.769	27.587	30.191	33.409	35.718
18	6.265	7.015	8.231	9.390	10.865	25.989	28.869	31.526	34.805	37.156
19	6.844	7.633	8.907	10.117	11.651	27.204	30.144	32.852	36.191	38.582
20	7.434	8.260	9.591	10.851	12.443	28.412	31.410	34.170	37.566	39.997
21	8.034	8.897	10.283	11.591	13.240	29.615	32.671	35.479	38.932	41.401
22	8.643	9.542	10.982	12.338	14.041	30.813	33.924	36.781	40.289	42.796
23	9.260	10.196	11.689	13.091	14.848	32.007	35.172	38.076	41.638	44.181
24	9.886	10.856	12.401	13.848	15.659	33.196	36.415	39.364	42.980	45.559
25	10.520	11.524	13.120	14.611	16.473	34.382	37.652	40.646	44.314	46.928
26	11.160	12.198	13.844	15.379	17.292	35.563	38.885	41.923	45.642	48.290
27	11.808	12.879	14.573	16.151	18.114	36.741	40.113	43.195	46.963	49.645
28	12.461	13.565	15.308	16.928	18.939	37.916	41.337	44.461	48.278	50.993
29	13.121	14.256	16.047	17.708	19.768	39.087	42.557	45.722	49.588	52.336
30	13.787	14.953	16.791	18.493	20.599	40.256	43.773	46.979	50.892	53.672
40	20.707	22.164	24.433	26.509	29.051	51.805	55.758	59.342	63.691	66.766
50	27.991	29.707	32.357	34.764	37.689	63.167	67.505	71.420	76.154	79.490
60	35.534	37.485	40.482	43.188	46.459	74.397	79.082	83.298	88.379	91.952
70	43.275	45.442	48.758	51.739	55.329	85.527	90.531	95.023	100.425	104.215
80	51.172	53.540	57.153	60.391	64.278	96.578	101.879	106.629	112.329	116.321
90	59.196	61.754	65.647	69.126	73.291	107.565	113.145	118.136	124.116	128.299
100	67.328	70.065	74.222	77.929	82.358	118.498	124.342	129.561	135.807	140.169

Bibliography

- Bardelli, S., et al. 2010, *A&A*, 511, A1, A1
- Bertoldi, F., et al. 2007, *ApJS*, 172, 132, 132
- Bondi, M., et al. 2008, *ApJ*, 681, 1129, 1129
- Bruzual, G., & Charlot, S. 2003, *MNRAS*, 344, 1000, 1000
- Burns, J. O., Gregory, S. A., & Holman, G. D. 1981, *ApJ*, 250, 450, 450
- Capak, P., et al. 2007, *ApJS*, 172, 99, 99
- Chiaberge, M., et al. 2010, *ApJL*, 710, L107, L107
- Ciliegi, P., et al. 2003, *A&A*, 398, 901, 901
- . 2005, *A&A*, 441, 879, 879
- Coles, P., & Lucchin, F. 2002, *Cosmology - The Origin And Evolution Of Cosmic Structures*
- Croton, D. J., et al. 2006, *MNRAS*, 365, 11, 11
- Dahlen, T., et al. 2005, *ApJ*, 631, 126, 126
- Diener, C., et al. 2013, *ApJ*, 765, 109, 109
- Durret, F., et al. 2011, *A&A*, 535, A65, A65
- Elvis, M., et al. 2009, *ApJS*, 184, 158, 158
- Fanaroff, B. L., & Riley, J. M. 1974, *MNRAS*, 167, 31P, 31P
- Ferrarese, L., & Merritt, D. 2000, *ApJL*, 539, L9, L9
- Gebhardt, K., et al. 2000, *ApJL*, 539, L13, L13
- Hardcastle, M. J., et al. 2007, *MNRAS*, 376, 1849, 1849
- Hasinger, G., et al. 2007, *ApJS*, 172, 29, 29
- Hickox, R. C., et al. 2009, *ApJ*, 696, 891, 891

- Hopkins, P. F., et al. 2008a, *ApJS*, 175, 356, 356
- . 2008b, *ApJS*, 175, 390, 390
- Ilbert, O., et al. 2006, *A&A*, 457, 841, 841
- . 2009, *ApJ*, 690, 1236, 1236
- . 2010, *ApJ*, 709, 644, 644
- Kodama, T., et al. 2007, in *Astronomical Society Of The Pacific Conference Series*, Vol. 379, *Cosmic Frontiers*, ed. N. Metcalfe & T. Shanks, 202
- Kormendy, J. 1982, in *Saas-Fee Advanced Course 12: Morphology And Dynamics Of Galaxies*, ed. L. Martinet & M. Mayor, 113–288
- Kormendy, J., & Richstone, D. 1995, *ARA&A*, 33, 581, 581
- Krolik, J. H. 1999, *Active Galactic Nuclei*
- Lilly, S. J., et al. 2007, *ApJS*, 172, 70, 70
- Longair, M. S. 2008, *Galaxy Formation*, Second Edition
- Magorrian, J., et al. 1998, *AJ*, 115, 2285, 2285
- Miley, G., & De Breuck, C. 2008, *A&APR*, 15, 67, 67
- Mobasher, B., et al. 2007, *ApJS*, 172, 117, 117
- Peterson, B. M. 1997, *An Introduction To Active Galactic Nuclei*
- Polletta, M., et al. 2007, *ApJ*, 663, 81, 81
- Press, W. H., Teukolsky, S. A., Vetterling, W. T., & Flannery, B. P. 2007, *Numerical Recipes - The Art Of Scientific Computing*, Third Edition
- Sanders, D. B., et al. 2007, *ApJS*, 172, 86, 86
- Schinnerer, E., et al. 2004, *AJ*, 128, 1974, 1974
- . 2007, *ApJS*, 172, 46, 46
- . 2010, *ApJS*, 188, 384, 384
- Scoville, N., et al. 2007a, *ApJS*, 172, 38, 38
- . 2007b, *ApJS*, 172, 1, 1
- Silverman, J. D., et al. 2009, *ApJ*, 695, 171, 171
- Soifer, B. T., et al. 2008, *ARA&A*, 46, 201, 201
- Spergel, D. N., et al. 2003, *ApJS*, 148, 175, 175
- Springel, V., et al. 2005, *Nature*, 435, 629, 629
- Sutherland, W., & Saunders, W. 1992, *MNRAS*, 259, 413, 413
- Tabor, G., & Binney, J. 1993, *MNRAS*, 263, 323, 323

Taniguchi, Y., et al. 2007, *ApJS*, 172, 9, 9

Urry, C. M., & Padovani, P. 1995, *PASP*, 107, 803, 803

Venemans, B. P., et al. 2007, *A&A*, 461, 823, 823

White, S. D. M., & Rees, M. J. 1978, *MNRAS*, 183, 341, 341

Wright, E. L. 2006, *PASP*, 118, 1711, 1711

Wylezalek, D., et al. 2013, *ApJ*, 769, 79, 79

Zamojski, M. A., et al. 2007, *ApJS*, 172, 468, 468

List of Figures

1.1	The galaxy formation mechanism which operates on small cluster scales. (Figure from Hopkins et al. (2008a)).	2
1.2	A schematic representation of the evolution of the primordial fluctuations. The evolution for three species is represented: a cold dark matter component (δ_X), a baryonic component (δ_m) and a radiation component (δ_r). Figure taken from Coles & Lucchin (2002)	3
1.3	The galaxy formation mechanism, differentiated by host dark matter halo mass. Figure from Hickox et al. (2009).	6
1.4	The Cosmic Star Formation History. On the vertical axis is the Infrared Luminosity Density is plotted, used as a proxy for star formation. (Figure From Soifer et al. (2008)).	8
1.5	Galaxy luminosity functions, in the K and b_J bands. The solid line represents the model with AGN feedback, the dashed line represents the model without AGN feedback. The agreement with the data is much better for the AGN feedback case. Data points are taken from the literature. (Figure from Croton et al. (2006)).	9
2.1	Comparison between spectroscopic and photometric redshift, zCOSMOS-Bright. This figure is taken from Ilbert et al. (2009).	18
2.2	Left Panel: Comparison between spectroscopic and photometric redshift, zCOSMOS-Faint. Right Panel: Comparison between spectroscopic and photometric redshift, MIPS-Spectro-z. This figure is taken from Ilbert et al. (2009).	19
2.3	Radio Source Counts (From Bondi et al. (2008)). The various symbols refer to various radio surveys as explained in the image (see also the image caption in the reference).	20
2.4	Area Coverage. The red dots refer to the optical sample, the blue dots refer to the radio sample.	22
3.1	Total Radio Flux Distributions. The red line shows the distribution for the radio sample. The blue line shows the distribution for the radio-optical sample. The plot is normalized to 1.	28

3.2	Apparent I-band Magnitude Distributions. The red line shows the distribution for the optical sample. The blue line shows the distribution for the radio-optical sample. The plot is normalized to unity.	29
3.3	Redshift Distributions. The red line shows the distribution for the optical sample. The blue line shows the distribution for the radio-optical sample. A cut has been made, selecting only those galaxies with apparent I-band magnitude lower than 26.5. The plot is normalized to 1.	30
3.4	Distribution on the plane of the sky of galaxies composing the peak at $z = 2$. The black stars represent the total optical sample, while the yellow triangles represent the galaxies from the radio-optical sample with redshift between 1.75 and 2.25.	31
3.5	Absolute I-band Magnitude Vs. Redshift. The black stars represent the whole optical sample, the purple triangles represent the radio-optical sample. The cut to apparent I-band magnitude lower than 26.5 has been applied.	32
3.6	The correlation between radio luminosity at 1.4 GHz and redshift. The red dots represent the radio sample.	33
3.7	Specific Star Formation Rate Vs. Stellar Mass. The black stars represent the whole optical sample, the red triangles represent the radio-optical sample.	34
3.8	Specific Star Formation Rate Vs. Stellar Mass. The plot is derived for the optical sample in three redshift bins, as described in text. The black stars identify Bin 1, the red crosses Bin 2, the blue triangles Bin 3. The redshift bins are defined in the following way: Bin 1 refers to $z = 0 \div 1$, Bin 2 to $z = 1 \div 2$ and Bin 3 to $z = 2 \div 3$	35
3.9	Specific Star Formation Rate Vs. Stellar Mass. The plot is derived for the radio-optical sample in three redshift bins, as described in text. The black stars identify Bin 1, the red crosses Bin 2, the blue triangles Bin 3. The redshift bins are defined in the following way: Bin 1 refers to $z = 0 \div 1$, Bin 2 to $z = 1 \div 2$ and Bin 3 to $z = 2 \div 3$	36
3.10	Evolution Of Galaxies In The $SSFR-M^*$ Plot. The solid black line represents the optical sample, while the red dash-dot one represents the radio-optical sample.	37
4.1	Fixed Coordinates	42
4.2	Fixed Coordinates, I-Band Apparent Magnitude Cut	45
4.3	Fixed Coordinates, I-Band Apparent Magnitude Cut, Stellar Mass And SSFR Cut	47
4.4	Fixed Coordinates, I-Band Apparent Magnitude Cut, Stellar Mass And SSFR Cut	49
4.5	Fixed Coordinates, I-Band Apparent Magnitude Cut, Stellar Mass And SSFR Cut, Applied Also To The Optical Sample.	51
4.6	Fixed Coordinates, I-Band Apparent Magnitude Cut, Stellar Mass And SSFR Cut, Applied Also To The Optical Sample.	52
4.7	Redshift Dependent Coordinates	55
4.8	Redshift Dependent Coordinates, Apparent Magnitude Cut.	56

4.9	Redshift Dependent Coordinates, Apparent Magnitude Cut, SSFR And Stellar Mass Cut	58
4.10	Redshift Dependent Coordinates, Apparent Magnitude Cut, SSFR And Stellar Mass Cut	59
4.11	Redshift Dependent Coordinates, Apparent Magnitude Cut, SSFR And Stellar Mass Cut Applied Also To The Optical Sample . . .	61
4.12	Redshift Dependent Coordinates, Apparent Magnitude Cut, SSFR And Stellar Mass Cut Applied Also To The Optical Sample . . .	62
4.13	Reduced χ^2 Value Distribution. The black line represents the distribution of the 100 reduced χ^2 values obtained by comparing the radio-optical sample to the 100 control samples extracted as described in text. The red line represents the tabulated value for a significativity level of 0.005.	64
4.14	Reduced χ^2 Value Distribution. The black line represents the distribution of the 100 reduced χ^2 values obtained by comparing the radio-optical sample to the 100 control samples extracted as described in text. The red line represents the tabulated value for a significativity level of 0.005. The magnitude cut to 26.5 has been applied to the data.	65
4.15	Reduced χ^2 Value Distribution. The black line represents the distribution of the 100 reduced χ^2 values obtained by comparing the radio-optical sample to the 100 control samples extracted as described in text. The red line represents the tabulated value for a significativity level of 0.005. The magnitude cut to 26.5 and the cuts to $\log(\frac{M^*}{M_\odot}) > 10$ and to $\log(SSFR) < -11$ have been applied to the data.	66
4.16	Reduced χ^2 Value Distribution. The black line represents the distribution of the 100 reduced χ^2 values obtained by comparing the radio-optical sample to the 100 control samples extracted as described in text. The red line represents the tabulated value for a significativity level of 0.005. The magnitude cut to 26.5 and the cuts to $\log(\frac{M^*}{M_\odot}) > 10$ and to $\log(SSFR) > -11$ have been applied to the data.	67
4.17	Reduced χ^2 Value Distribution. The black line represents the distribution of the 100 reduced χ^2 values obtained by comparing the radio-optical sample to the 100 control samples extracted as described in text. The red line represents the tabulated value for a significativity level of 0.005. The magnitude cut to 26.5 and the cuts to $\log(\frac{M^*}{M_\odot}) > 10$ and to $\log(SSFR) > -11$ have been applied to the data, including the optical sample.	68
4.18	Reduced χ^2 Value Distribution. The black line represents the distribution of the 100 reduced χ^2 values obtained by comparing the radio-optical sample to the 100 control samples extracted as described in text. The red line represents the tabulated value for a significativity level of 0.005. The magnitude cut to 26.5 and the cuts to $\log(\frac{M^*}{M_\odot}) > 10$ and to $\log(SSFR) < -11$ have been applied to the data, including the optical sample.	69

4.19	Reduced χ^2 Value Distribution. The black line represents the distribution of the 100 reduced χ^2 values obtained by comparing the radio-optical sample to the 100 control samples extracted as described in text. The red line represents the tabulated value for a significativity level of 0.005. The redshift dependence has been implemented.	70
4.20	Reduced χ^2 Value Distribution. The black line represents the distribution of the 100 reduced χ^2 values obtained by comparing the radio-optical sample to the 100 control samples extracted as described in text. The red line represents the tabulated value for a significativity level of 0.005. The redshift dependence has been implemented. The apparent I-band magnitude cut to 26.5 has been applied to the data.	71
4.21	Reduced χ^2 Value Distribution. The black line represents the distribution of the 100 reduced χ^2 values obtained by comparing the radio-optical sample to the 100 control samples extracted as described in text. The red line represents the tabulated value for a significativity level of 0.005. The redshift dependence has been implemented. The apparent I-band magnitude cut to 26.5 has been applied to the data, as well as the cuts to $\log(\frac{M^*}{M_\odot}) > 10$ and $\log(SSFR) > -11$	72
4.22	Reduced χ^2 Value Distribution. The black line represents the distribution of the 100 reduced χ^2 values obtained by comparing the radio-optical sample to the 100 control samples extracted as described in text. The red line represents the tabulated value for a significativity level of 0.005. The redshift dependence has been implemented. The apparent I-band magnitude cut to 26.5 has been applied to the data, as well as the cuts to $\log(\frac{M^*}{M_\odot}) > 10$ and $\log(SSFR) < -11$	73
4.23	Reduced χ^2 Value Distribution. The black line represents the distribution of the 100 reduced χ^2 values obtained by comparing the radio-optical sample to the 100 control samples extracted as described in text. The red line represents the tabulated value for a significativity level of 0.005. The redshift dependence has been implemented. The apparent I-band magnitude cut to 26.5 has been applied to the data, as well as the cuts to $\log(\frac{M^*}{M_\odot}) > 10$ and $\log(SSFR) > -11$, also to the optical sample.	74
4.24	Reduced χ^2 Value Distribution. The black line represents the distribution of the 100 reduced χ^2 values obtained by comparing the radio-optical sample to the 100 control samples extracted as described in text. The red line represents the tabulated value for a significativity level of 0.005. The redshift dependence has been implemented. The apparent I-band magnitude cut to 26.5 has been applied to the data, as well as the cuts to $\log(\frac{M^*}{M_\odot}) > 10$ and $\log(SSFR) > -11$, also to the optical sample.	75
5.1	Redshift Dependent Coordinates, $1 \leq z \leq 2$	78
5.2	Redshift Dependent Coordinates, $1 \leq z \leq 2$, Apparent I-Band Magnitude Cut.	80

5.3	Redshift Dependent Coordinates, $1 \leq z \leq 2$, Apparent I-Band Magnitude Cut, Stellar Mass And Specific Star Formation Cuts.	81
5.4	Redshift Dependent Coordinates, $1 \leq z \leq 2$, Apparent I-Band Magnitude Cut, Stellar Mass And Specific Star Formation Cuts.	82
5.5	Redshift Dependent Coordinates, $1 \leq z \leq 2$, Apparent I-Band Magnitude Cut, Stellar Mass And Specific Star Formation Cuts Applied Also To The Optical Sample.	83
5.6	Redshift Dependent Coordinates, $1 \leq z \leq 2$, Apparent I-Band Magnitude Cut, Stellar Mass And Specific Star Formation Cuts Applied Also To The Optical Sample.	85
5.7	Environment Of Low Power Radio Sources. The cut to $24 \leq \log(\frac{L_{1.4GHz}}{W/Hz}) \leq 24.5$ has been applied, together with the restriction to $1 \leq z \leq 2$ and the apparent I-band magnitude cut to 26.5.	87
5.8	Environment Of High Power Radio Sources. The cut to $\log(\frac{L_{1.4GHz}}{W/Hz}) > 24.5$ has been applied, together with the restriction to $1 \leq z \leq 2$ and the apparent I-band magnitude cut to 26.5.	88
5.9	Environment Of Low Power Radio Sources. The cut to $24 \leq \log(\frac{L_{1.4GHz}}{W/Hz}) \leq 24.5$ has been applied, together with the restriction to $1 \leq z \leq 2$, the apparent I-band magnitude cut to 26.5 and the cuts to $\log(\frac{M^*}{M_\odot}) > 10$ and $\log(SSFR) > -11$	89
5.10	Environment Of High Power Radio Sources. The cut to $\log(\frac{L_{1.4GHz}}{W/Hz}) > 24.5$ has been applied, together with the restriction to $1 \leq z \leq 2$, the apparent I-band magnitude cut to 26.5 and the cuts to $\log(\frac{M^*}{M_\odot}) > 10$ and $\log(SSFR) > -11$	91
5.11	Environment Of Low Power Radio Sources. The cut to $24 \leq \log(\frac{L_{1.4GHz}}{W/Hz}) \leq 24.5$ has been applied, together with the restriction to $1 \leq z \leq 2$, the apparent I-band magnitude cut to 26.5 and the cuts to $\log(\frac{M^*}{M_\odot}) > 10$ and $\log(SSFR) < -11$	92
5.12	Environment Of High Power Radio Sources. The cut to $\log(\frac{L_{1.4GHz}}{W/Hz}) > 24.5$ has been applied, together with the restriction to $1 \leq z \leq 2$, the apparent I-band magnitude cut to 26.5 and the cuts to $\log(\frac{M^*}{M_\odot}) > 10$ and $\log(SSFR) < -11$	93

List of Tables

2.1	Bands Of Observations	14
2.2	Additional Bands	15
2.3	The Sample	23
3.1	Mean Total Radio Flux, I-Band Apparent Magnitude And Redshift.	31
3.2	Fractions Of Galaxies With $\log(\frac{M^*}{M_\odot}) \geq 10$ And $\log(SSFR) \leq -10$	37
4.1	Cosmological Set Up	40
4.2	The Study Of The Environment, Fixed Distance	50
4.3	The Study Of The Environment, Redshift Dependent Radius . .	63
5.1	The Study Of The Environment, Redshift Dependent Radius, Restriction To Redshift $1 \leq z \leq 2$	84
5.2	The Study Of The Environment, Absolute Radio Luminosity Se- lection, $1 \leq z \leq 2$	94